DISSERTATION

PRECISION MEASUREMENTS ON A SINGLE TRAPPED BERYLLIUM ION

Submitted by

David M. Fairbank

Department of Physics

In partial fulfillment of the requirements

For the Degree of Doctor of Philosophy

Colorado State University

Fort Collins, Colorado

Spring 2024

Doctoral Committee:

Advisor: Samuel M. Brewer

Dylan Yost
Christian Sanner
Alan Van Orden

ABSTRACT

PRECISION MEASUREMENTS ON A SINGLE TRAPPED BERYLLIUM ION

Precision laser spectroscopy of transitions in simple atoms can be used as a stringent test of many-body quantum electrodynamics (QED) calculations, or to extract subtle information about internal nuclear structure. $^{9}Be^{+}$ is a three electron ion which has been the focus of study in ion trap and high energy beam experiments dating back several decades. We present the first measurements of the D-lines in $^{9}Be^{+}$ using a single trapped ion, which reduced the experimental uncertainty of both the D_1 and D_2 transitions by an order of magnitude. A framework for characterization of systematic shifts due to effects like photon recoil and quantum interference in ion trap-based measurements of strong transitions is presented. From the D_2 lineshape data, a ^{2}P excited state lifetime was extracted with reduced uncertainty and better agreement with theory, compared to previous work. The first experimental measurement of the unresolved $^{2}P_{3/2}$ hyperfine splittings is reported, which helped to uncover a sign error in the theoretical prediction of the $^{2}P_{3/2}$ electric quadrupole hyperfine constant. This measurement required development of techniques to selectively isolate and measure the unresolved components, utilizing the exceptional state preparation and control available for trapped ions. The 1.25 GHz $^{2}S_{1/2}$ ground state hyperfine splitting was measured with a relative uncertainty of 1.6×10^{-11} using microwave Ramsey spectroscopy and is in good agreement with previous measurements made in Penning traps at NIST. The technique can be extended to the rare isotope $^{7}Be^{+}$, for which the current hyperfine constant uncertainty is four orders of magnitude larger. This planned measurement could enable extraction of an improved value of the ^{7}Be nuclear Zemach radius. D-line measurements on the rare isotopes $^{7,10}Be^{+}$ are also planned using the techniques developed for $^{9}Be^{+}$. A comparison of the fine structure splitting across the isotope chain can be used to extract the

relative nuclear charge radii or test the many-body QED contributions to theory in Li-like ions. A new ion trap was built and direct ablation loading of the ion trap from small $^{9}BeCl_2$ salt deposits was demonstrated in preparation for loading the rare isotopes from evaporated aqueous solution.

ACKNOWLEDGEMENTS

I wish to extend sincere gratitude to professors Sam Brewer and Dylan Yost for their support and encouragement prior to and throughout graduate school. I also want to recognize the significant contributions which were made by other students in the lab in building the infrastructure, taking data, troubleshooting issues and sharing individual expertise. In particular, Robert Gunkelman, Alessando Banducci and Jacob VanArsdale all made extensive contributions to the work. I want to thank Ryan Bullis and Will Tavis for maintaining and providing light from the optical frequency comb, the staff at WWV for their help with the stabilized fiber link, and Krzysztof Pachucki, Mariusz Puchalski and Vladimir Yerokhin for help and discussions regarding the theoretical 2p $^2P_{3/2}$ electric quadrupole hyperfine coefficient. A thank you to John Bollinger, Dylan Yost and Christian Sanner for proofreading and helpful discussions of the publications. I would like to acknowledge the NIST precision measurement grant program which supported this project. Additional funding support for the lab was received from Colorado State University, the Office of Naval Research and the National Science Foundation.

I wish to acknowledge the support from my wife Michelle and our three sons, two of which were born during this time period. Pursuing a degree at a later stage in life was a blessing but also a challenge. To Michelle, we have made it through many hardships together and I appreciate your patience and endurance through all of it.

DEDICATION

For my wife Michelle and our three sons, Lucas, Adrian and Clifton.

TABLE OF CONTENTS

LIST OF TABLES

LIST OF FIGURES

Chapter 1

Introduction

1.1 Motivation

Few-electron atoms are ideal systems for tests of many-body quantum electrodynamics (QED) and searches for physics beyond the standard model of particle physics [1]. The relatively simple atomic structure enables *ab initio* calculations of transition frequencies and fine structure splittings with an accuracy comparable to what can be achieved in high-precision laser spectroscopy experiments, including systems such as lithium and Li-like ions [2–4]. In addition, precision laser spectroscopy on transitions in simple atoms can be used to extract information about nuclear structure. A well-known example is the "proton radius puzzle," in which a discrepancy exists in the extracted proton radius between precise measurements of regular atomic hydrogen and muonic hydrogen [5]. More generally for alkali-like systems, measurement of the ground-state hyperfine splitting can be used to extract the nuclear magnetic dipole moment, charge radius or Zemach radius of the nucleus [4]. Measurement of the ^2P fine structure splitting across an isotope chain can yield the relative nuclear charge radii between isotopes [6, 7]. Excited state hyperfine structure measurements can be used to extract higher order nuclear electromagnetic moments, such as the electric quadrupole or magnetic octupole moments [8–11].

$^9\mathrm{Be}^+$ is a Li-like three-electron system with laser-accessible D-line transitions around 313 nm ($2s\ ^2S_{1/2} \longleftrightarrow 2p\ ^2P_{1/2,3/2}$) for Doppler cooling and detection, and a long-lived ground state hyperfine qubit ($I_{nuc} = 3/2$). These features have made it widely used in precision laser spectroscopy experiments [12–15], quantum information processing [16, 17] and as a sympathetic cooling partner in quantum-logic clocks [18, 19]. Although $^9\mathrm{Be}^+$ had been utilized for such purposes for several decades, the fundamental limitations of ion trap-based precision measurements of the strong transitions and hyperfine structure had not been fully explored.

In this work, we characterized the leading systematic effects due to photon recoil and quantum interference, and were able to improve upon the existing experimental values for all of the ground and first excited state structure. The framework developed in measurements of $^{9}Be^{+}$ will enable the extension of this work to the study of rare isotopes $^{7,10}Be^{+}$ in the future. Comparison of absolute frequency measurements of the D-lines between isotopes 7, 9 and 10 will yield an improved characterization of the splitting isotope shift and the relative nuclear charge radii. The planned work will also enable a high accuracy test of many-body QED in a 3 electron system.

An additional use for single $^{9}Be^{+}$ is as a sympathetic cooling partner and logic ion in highly charged ion (HCI)-based quantum-logic clocks aimed at searching for time-variation of the fine structure constant, α. By comparing two HCI clocks with different α-sensitivity factors it will be possible to investigate possible new physics such as the nature of ultra-light scalar dark matter [1]. The trap characterization and experimental developments necessary for the strong transition measurements in this work are also prerequisite for the future work building quantum-logic clocks.

1.2 Energy Level Structure

Be^{+} has three electrons, with ground state configuration $1s^2 2s$. The lowest energy excited state is $1s^2 2p$, which is split into two fine structure levels, $^{2}P_{1/2}$ and $^{2}P_{3/2}$. The fine-structure splitting, $\Delta\nu_{fs}$, is approximately 197 GHz. The dipole allowed transitions to these two excited states in alkali-like systems are referred to as the D_1 and D_2 transitions, and in $^{9}Be^{+}$ have a natural linewidth of about 18 MHz [20,21]. A Grotrian diagram of the relevant energy level structure for $^{9}Be^{+}$ is shown in Figure 1.1.

A convenient feature is the σ^{-} (or σ^{+}) D_2 closed cycling transition which is used for Doppler cooling, state preparation and detection. From there, resolved hyperfine transitions within the $^{2}S_{1/2}$ ground state can be driven coherently with a controlled microwave field to manipulate atomic state populations.

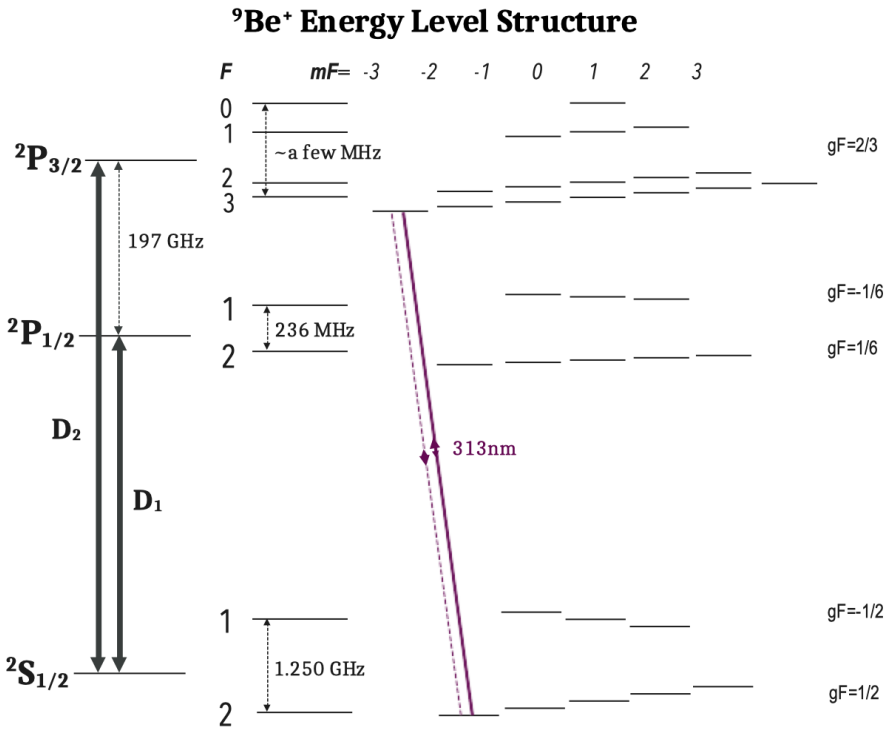

Figure 1.1: Energy level structure of ^{9}Be$^+$. The D_2 σ^- cycling transition used for Doppler cooling and state detection is shown in purple. The structure of ^{7}Be$^+$ is similar, with nuclear spin 3/2 and ground state hyperfine splitting of 1.49 GHz instead.

1.3 State of Prior Measurements

Prior to the work done here, several measurements of the D-line transition frequencies were made on ^{9}Be$^+$. A summary of the results is shown in Figure 1.2. The first measurement was done using clouds of laser-cooled ions stored in a Penning trap at NIST [13]. Further measurements were performed with bunches of buffer gas-cooled and laser-cooled ions stored in an rf quadrupole trap at RIKEN [14], then later with beams of ions using collinear laser spectroscopy at the ISOLDE facility at CERN [15]. A 7σ (combined) discrepancy existed in the absolute frequency determination of the D_2 line between the laser-cooled ion trap measurement at RIKEN and the collinear laser spectroscopy result obtained at ISOLDE [14, 15]. A comparison of the ISOLDE measurements of the ^2P fine structure splitting, $\Delta\nu_{fs}$, and the $^2P_{1/2}$ hyperfine constant, $A_{P_{1/2}}$, with *ab initio* theory calculations revealed mild discrepancies of 1.8σ (combined) and 1.6σ (combined), respectively [3, 15, 22].

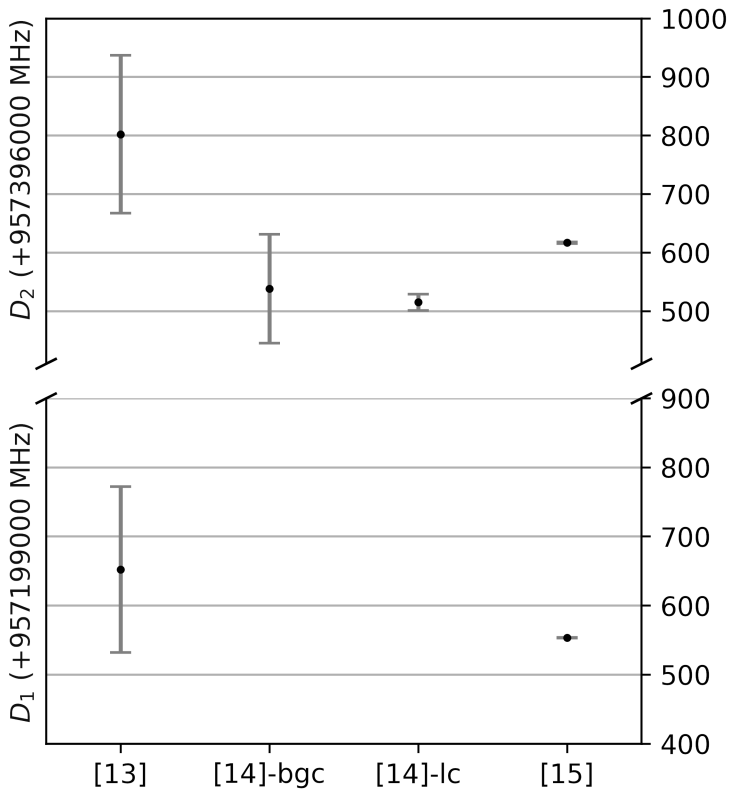

Figure 1.2: A summary of the prior D-line measurements is shown. The first was a measurement in 1985 by John Bollinger, using double resonance spectroscopy of ions in a Penning trap at NIST [13]. The second and third are buffer-gas-cooled (bgc) and laser-cooled (lc) results, respectively, measured on clouds of ions in an rf quadrupole trap at RIKEN [14]. The final result is from collinear laser spectroscopy at the ISOLDE facility at CERN [15].

The D-lines in isotopes 7, 9, 10, 11, and 12 were measured at the ISOLDE facility at CERN using collinear laser spectroscopy, with uncertainty on the order of 1 MHz [15]. The dominant uncertainty in those measurements is related to cancellation of the first order Doppler shifts between the spectroscopy lasers. The spectral lines in the experiment were also somewhat broadened from the 18 MHz natural linewidth [21] to about 40 MHz, from residual Doppler broadening. In comparison, ion trap based measurements of single, cooled ions of isotopes 7, 9 and 10 should have significantly reduced total systematic uncertainty. Such measurements require no first order Doppler shift cancellation, and the ions are sufficiently cold to have sub-natural-linewidth Doppler broadening. Residual broadening effects are

instead quantized at the secular and micromotion frequencies and can be characterized using motional sideband spectroscopy techniques.

The $^2P_{1/2}$ hyperfine splitting of approximately 236 MHz is resolved and had been measured most recently in the collinear laser spectroscopy measurement of the D lines [15], and earlier by Bollinger *et al.* at NIST [13]. The $^2P_{3/2}$ hyperfine structure is unresolved and had never been directly measured, with only rough limits having been determined using zero field quantum beat spectroscopy [23].

The 1.25 GHz ground state hyperfine splitting in $^9Be^+$ was measured to the exceptionally low uncertainty of 24 mHz under high magnetic fields (0.68 to 4.46 T), using clouds of laser-cooled ions stored in a Penning trap at NIST [12, 24, 25]. There had not been, however, a similar uncertainty measurement at low magnetic field. In a radiofrequency (rf) Paul trap, with a bias field of only about 1 Gauss, high magnetic field corrections like the diamagnetic shift are negligible. The 1.49 GHz ground state hyperfine splitting of the radioactive isotope $^7Be^+$ was previously measured to an uncertainty of 860 Hz using buffer gas cooled ions stored in a radiofrequency-quadrupole (RFQ) trap at RIKEN in 2008 [26]. This result could possibly be improved upon in our system by about 4 orders of magnitude. ^{10}Be is an even-even isotope with nuclear spin zero resulting in no additional hyperfine structure.

Chapter 2

Apparatus

2.1 Experiment Design and Ion Trap

2.1.1 System Overview

The main experimental apparatus consists of a linear radiofrequency (rf) Paul trap, mounted inside an ultrahigh vacuum (UHV) chamber, and UV lasers for cooling and spectroscopy. A schematic of the full apparatus, including the relative orientation of the ion trap and spectroscopy lasers, is shown in Figure 2.1. The octagonal spectroscopy chamber is oriented to allow laser access from six ports, which permits σ and π laser polarizations and all necessary k-vector orientations for resolved Raman sideband cooling and spectroscopy. Laser ablation can also be achieved on axis through the center of the trap. For $^9Be^+$, a single ion is loaded via laser ablation of a small length of beryllium wire [27]. The rf trap drive frequency of $\Omega_{rf}/2\pi = 78.93$ MHz is applied to opposing pairs of trap electrodes, to generate a differential drive amplitude of approximately $\pm$ 168 V. A DC bias voltage is added to each of the rf trap electrodes to provide both axial DC confinement and to break the radial mode degeracy in the trap. Additional compensation electrodes on the trap wafer allow for fine tuning of the ion position within the trap to minimize excess micromotion (EMM).

At the beginning of a typical experiment, regardless of which specific transition is being measured, the ion is cooled using 1 ms of far-detuned ($\Delta/2\pi = -415$ MHz) laser cooling and 500 μs of near-detuned Doppler cooling ($\Delta/2\pi = -10$ MHz) on the $|^2S_{1/2}, F = 2, m_F - 2\rangle \rightarrow |^2P_{3/2}, F = 3, m_F = -3\rangle$ cycling transition ($\Gamma/2\pi \approx 18$ MHz [21]). The final ion temperature after cooling was measured using stimulated Raman spectroscopy [28]. The temperature was consistent with the Doppler cooling limit of $T_D \approx 0.5$ mK [29]. The ion can be cooled further to the motional ground state using resolved Raman sideband transitions. While ground state cooling is necessary for quantum-logic spectroscopy, it is not required for measurements

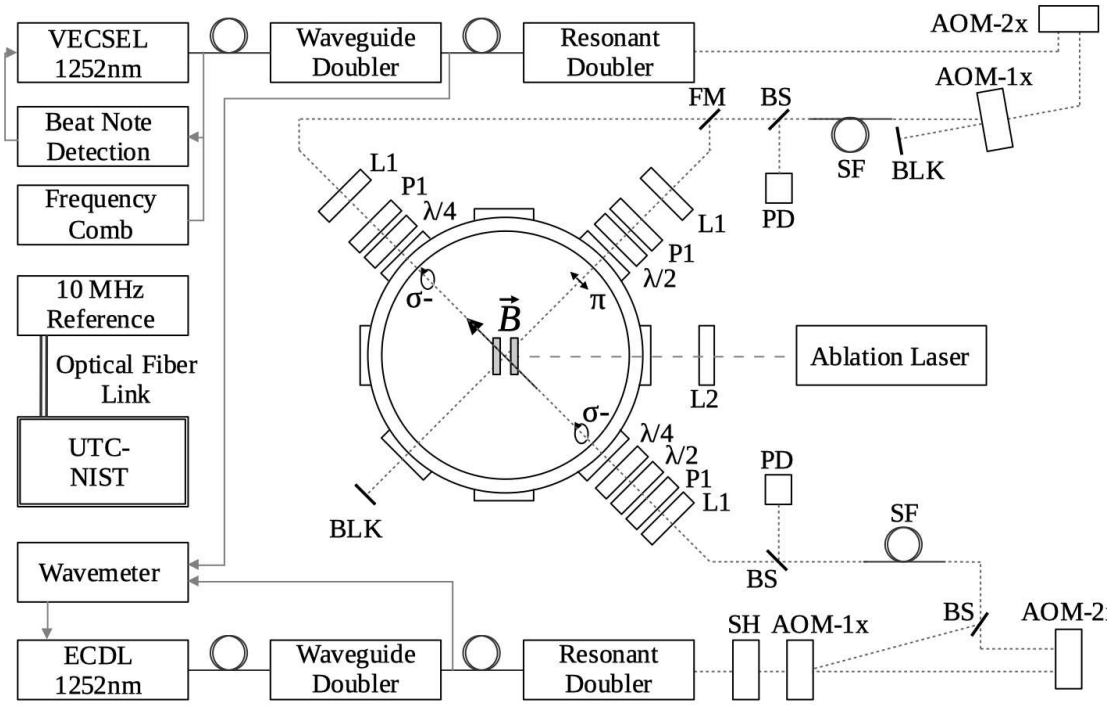

Figure 2.1: Schematic of the experimental setup for D_1 measurements. The D_1 spectroscopy laser (VECSEL) is frequency stabilized to the OFC. For D_2 measurements, the ECDL is locked to the optical frequency comb (OFC) and the VECSEL is not used. D_2 Doppler cooling and detection beams enter the chamber counter-propagating to the D_1 spectroscopy laser. Acousto-optic modulators in single (AOM-1x) and double-pass (AOM-2x) configurations generate the required laser frequencies. The laser polarization is set using a Glan-Laser polarizer (P1) plus half ($\lambda/2$) and quarter waveplates ($\lambda/4$). A flip mirror (FM) is used to switch between $\sigma-$ and π beams for D_1 measurements. An rf loop antenna for driving microwave transitions is located outside the vacuum chamber. The remaining components are single mode fiber spatial filter (SF), photodiode detector (PD), focusing lens (L1), high-speed shutter (SH), beamsplitter (BS), beam block (BLK).

of strong transitions. Furthermore, it can complicate the ion temperature and photon recoil characterization due to the possibility of non-thermal motional state distributions after GSC [30].

During the cooling sequence, optical pumping takes place which is used to prepare the ion in the $|^2S_{1/2}, F = 2, m_F - 2\rangle$ state. For most experimental configurations, a constant magnetic field of 0.0895(1) mT is applied along the quantization axis. The quantization field can be extracted with high precision by measuring the $|^2S_{1/2}, 2, -2\rangle \rightarrow |^2S_{1/2}, 1, -1\rangle$ microwave transition frequency, $\nu_{-2,-1} \approx 1251.9$ MHz.

2.1.2 Vacuum Chamber

A schematic of the vacuum chamber assembly used to house the ion trap is shown in Figure 2.2. The chamber is constructed using titanium to achieve the lowest possible hydrogen outgassing rate and final vacuum pressure at room temperature. A single Agilent Vacion Plus 55 ion pump, in conjunction with two SAES Capacitorr Z100 titanium non-evaporable getter (NEG) pumps maintain the vacuum pressure after the initial pump down and bake using a turbo-molecular pump. The final measured pressure as estimated by the ion pump current is about 10^{-11} Torr, or below. Lifetimes for a single trapped ion were on the order of about six or more hours before either being lost or converted to beryllium hydride. There was at least one case of the ion remaining in the trap overnight without any laser cooling. After the measurements of $^{9}Be^{+}$ were completed, the chamber was repurposed for trapping $^{40}Ca^{+}$. A second, nearly identical stainless steel chamber has been constructed using otherwise the same design, for experiments with the rare isotopes $^{7,10}Be^{+}$. The stainless steel chamber was tested first without the getter pumps and achieved a pressure around 8×10^{-10} Torr, which is low enough for the initial tests of loading from beryllium chloride salts. At this pressure the observed ion lifetime in the trap was reduced, typically on the order of about 1-2 hours. A single SAES Capacitorr Z100 NEG pump was purchased to add prior to installation of the rare isotopes for improved reduction of the residual hydrogen pressure.

A side view showing the vacuum chamber and ion trap from the entrance window of the σ^{-} Doppler cooling and spectroscopy beams is shown in Figure 2.3. A cutaway view of the mounted post assembly is shown in Figure 2.4.

2.1.3 Ion Trap Design

The linear Paul trap used in this work follows the design used in the Aluminum ion clock [27], adjusted for slight improvements to the electrode symmetry. The radial confinement is provided by gold coated electrodes on a diamond wafer. The characteristic radial ion-to-

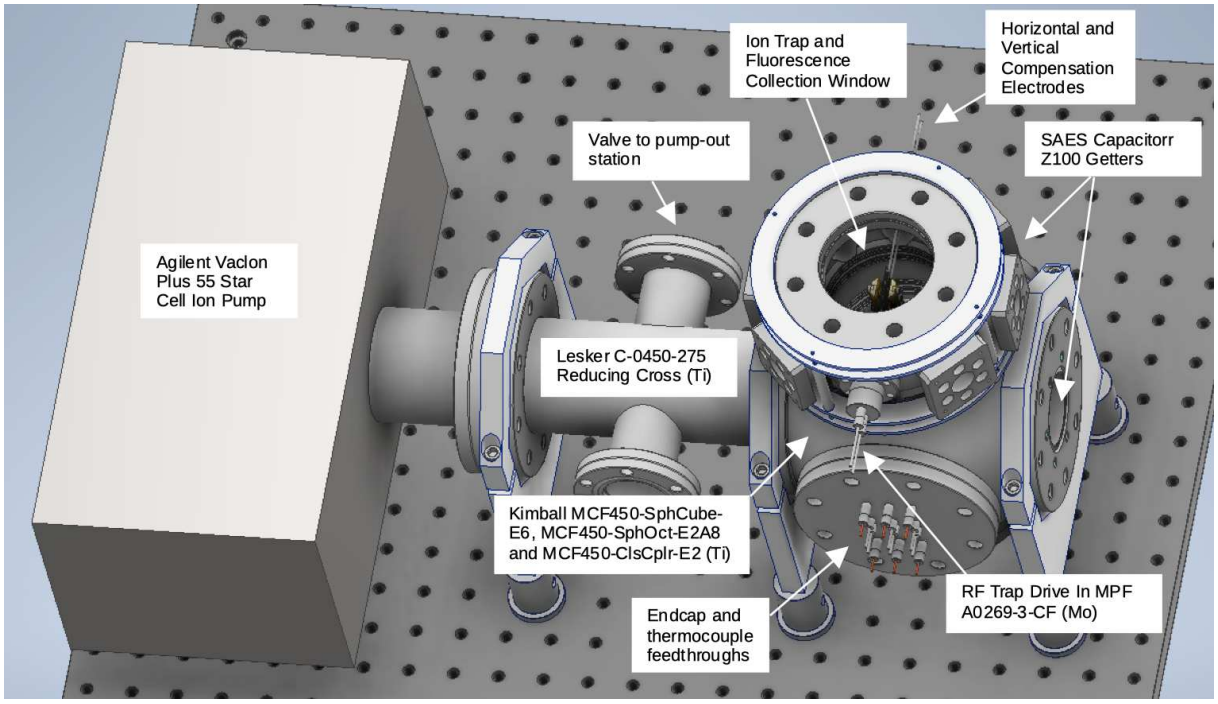

Figure 2.2: A CAD model of the vacuum chamber used for the experiments on $^{9}Be^{+}$ is shown in the figure. Major components are labeled. The first chamber was constructed out of titanium to reduce the hydrogen outgassing rate compared to stainless steel. The ion trap sits at the center of the top octagonal spectroscopy chamber, which allows laser access from six sides. Fluorescence from the ion is collected by the imaging system out from the top viewing window. A breadboard with holes on a 1" grid is shown for scale.

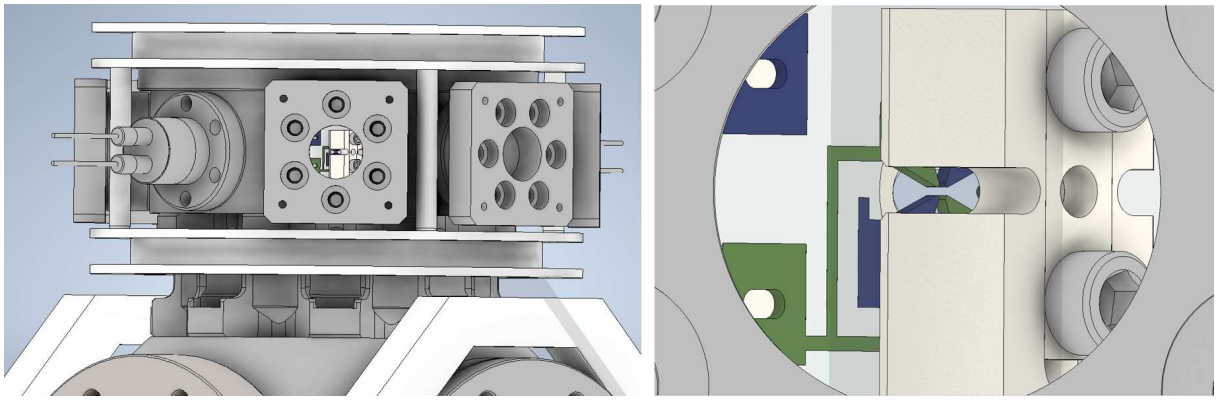

Figure 2.3: A side view of the vacuum chamber from the perspective of the incoming σ^{-} Doppler cooling and spectroscopy beams is shown on the left, with a zoomed in view of the center of the ion trap from the same perspective on the right. The rings above and below the optical axis were used for winding the vertical axis magnetic field compensation coils. Two other sets field coils were mounted on the 30mm cage system rods extending from the spectroscopy chamber for the other axes, but are not shown.

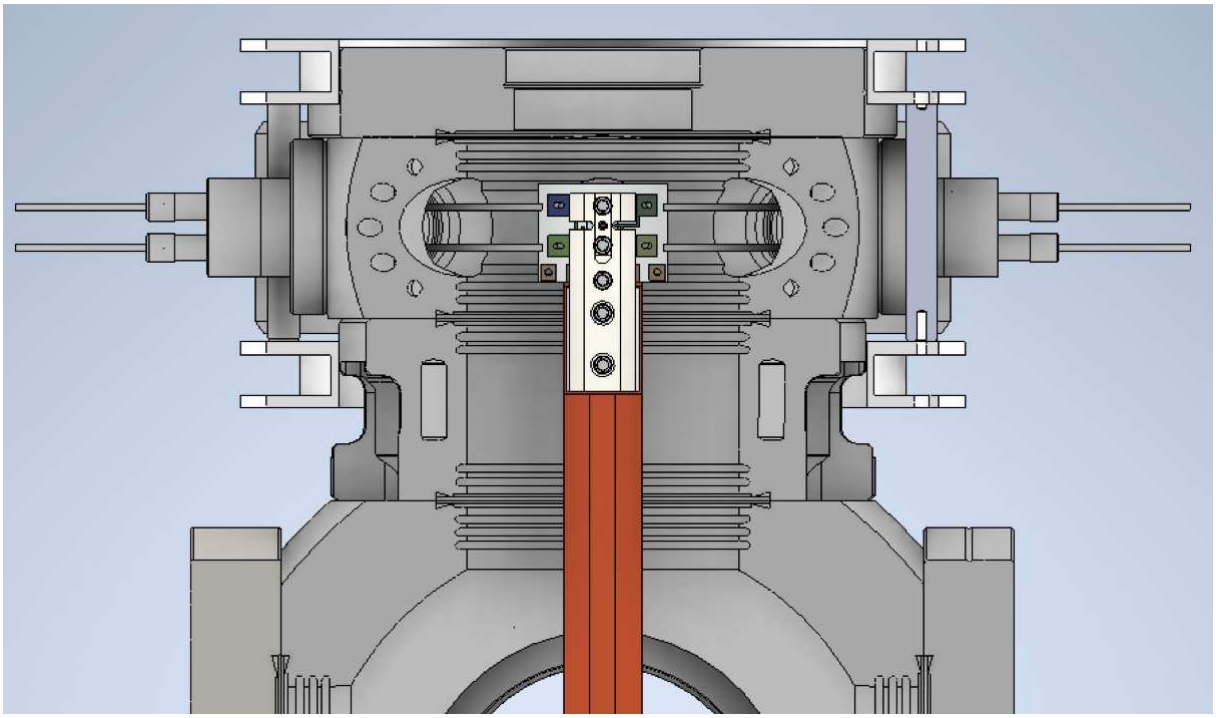

Figure 2.4: A cutaway view of the trap post assembly mounted within the vacuum chamber is shown. The diamond trap wafer and titanium endcaps sit mounted on a OFHC copper post with the optical axis aligned with the center of the octagonal spectroscopy chamber. The electrical connections for the trap electrodes enter from the left, with the horizontal and vertical compensation electrode connections on the right. The trap post is secured to the bottom of the spherical cube via a customized solid OFHC copper gasket.

electrode distance is 0.25 mm and the thickness of the wafer is 0.5 mm. Axial confinement is provided by a relative DC potential applied between the endcaps and the rf trap electrodes. The endcaps are symmetric and are each spaced 4 mm from the trap center. An image of the assembled trap wafer and encaps in the vacuum chamber is shown in Figure 2.5.

Typical secular mode frequencies of a single $^9Be^+$ ion are $\omega_z/2\pi \approx 3.65$ MHz for the axial mode, and $\omega_x/2\pi \approx 9.8$ MHz and $\omega_y/2\pi \approx 10.6$ MHz for the radial modes (in the plane of the trap wafer). The angles between the laser propagation direction and trap axes are $\theta_z = 45°$ (axial), $\theta_{x,y} = 60°$ (radial). The photon recoil frequencies for each axis are $\omega_{rec}/2\pi = 226$ kHz $\times \cos^2 \theta_{x,y,z}$. The Lamb-Dicke parameters are then defined as $\eta = (\omega_{rec}/\omega_{x,y,z})^{1/2}$, for each axis [31].

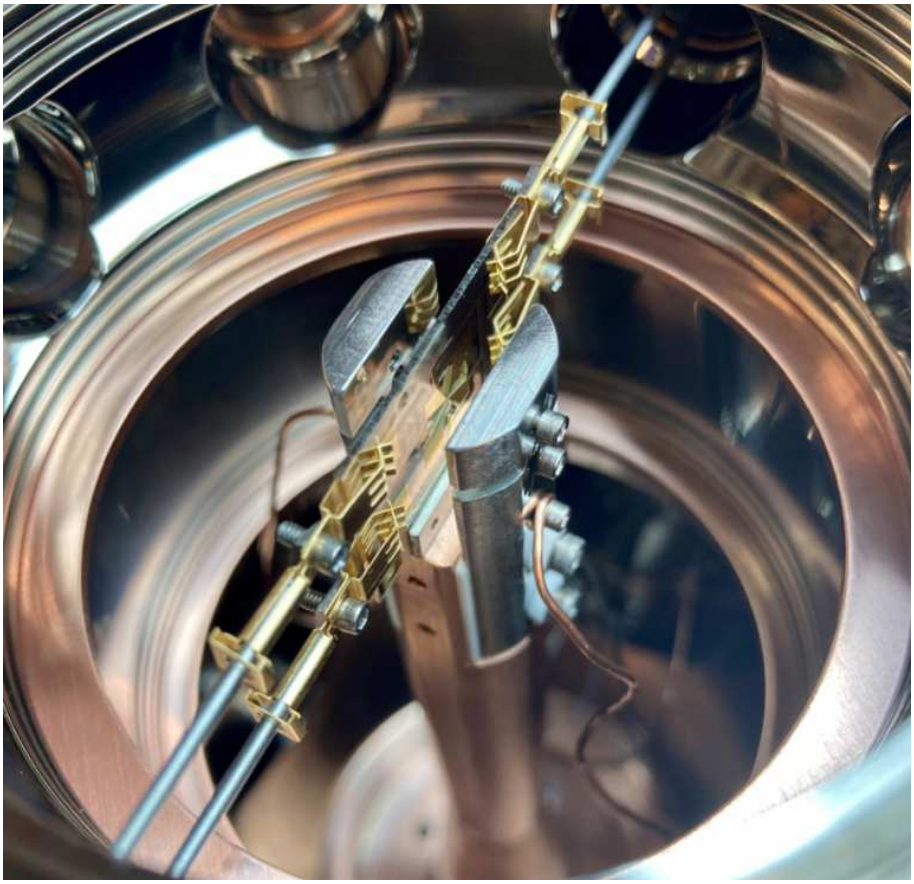

Figure 2.5: An image of the assembled trap is shown within the vacuum chamber. The diamond wafer with gold coated electrodes is secured to a copper post for heat dissipation, with titanium endcaps mounted on either side.

The equations of motion and stability conditions for various types of ion traps are described in the literature dating back several decades. The specifics for a linear rf Paul trap can be found in [32]. In our case we use a dual-ended drive supplied by a meander line waveguide resonator, such that the two sets of opposing pairs of electrodes have similar applied voltage but with opposite phase. The dual-ended drive has the effect of doubling V_0 compared to the single-ended drive case. The wheel trap geometry using a thin wafer and widely spaced endcaps is quite different than the original four-rod linear trap designs. The geometric scaling factor, κ, thus needs to be manually adjusted for the model results to match experiment. A plot of the calculated stability and classical trajectories under typical operating conditions are shown in Figure 2.6.

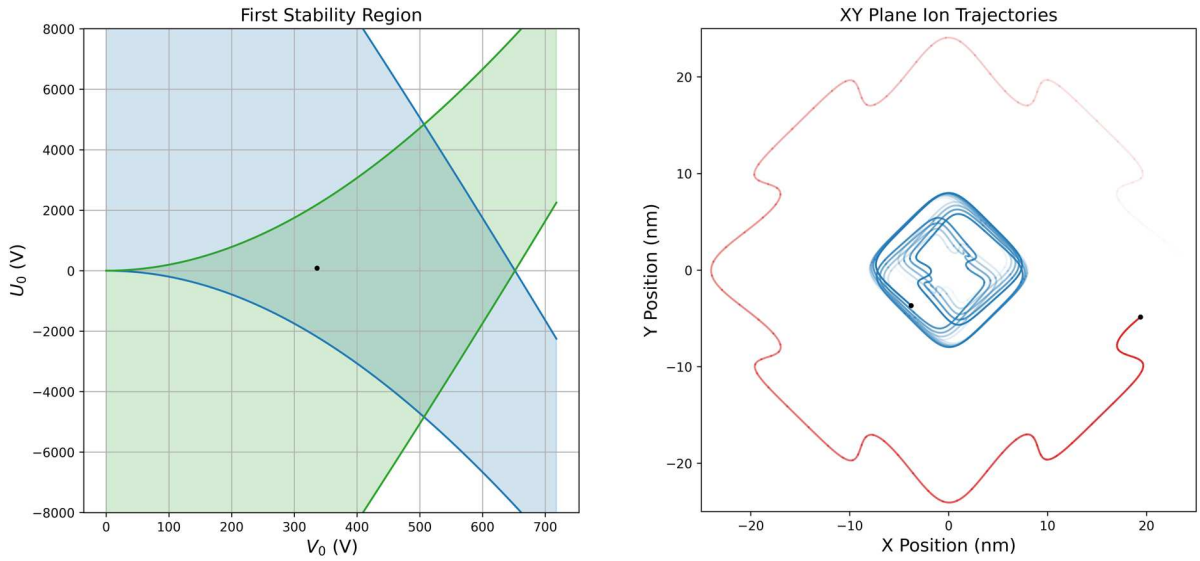

Figure 2.6: A stability diagram for the radial dimensions is shown as a function of the RF and DC voltages, V_0 and U_0, respectively (left). Note that V_0 is 2 times the single ended voltage since our trap uses dual-ended drive. The combined voltages must be within the central region for the ion trajectories to be stable. Note that while the radial stability is symmetric for positive and negative U_0 axial potential, positive ions are only stable in the axial dimension for positive values of U_0. The black dot on the left indicates the typical operating point. A plot of two example trajectories is shown (right), generated using an explicit Runge-Kutta numerical integration. The ion starts displaced in X with velocity component in Y equal to the mean velocity for the Doppler cooling limit temperature of about 0.5 mK. The blue plot shows a classical trajectory under the typical intermediate-strength radial confinement, $\omega_{x,y}$ ≈10 MHz. If the radial confinement is weakened(red), the secular mode frequencies decrease and it is easier to distinguish the secular motion(circular path) from the 80 MHz micromotion(small wiggles). The calculated paths are faded in to roughly show the time dependence over about 0.5 μs using a purely classical model.

2.1.4 ARTIQ Control System

The control system used in these experiments is based on a field programmable gate array (FPGA) architecture (ARTIQ) originally designed for applications in ion trap-based quantum computing. The control system consists of an FPGA and a bank of twelve Analog Devices AD9910 and four AD9912 direct digital synthesis (DDS) channels, plus various TTL and low-voltage analog inputs and outputs that are used to control the experiment. The AD9912 channels have a frequency resolution of 4 μHz, but lack the convenient amplitude control of the AD9910. In this work the resolution of the AD9912 was only required for the

Ramsey spectroscopy measurement of the ground state hyperfine splitting. Otherwise, the AD9910 channels were sufficient.

2.1.5 Trap Drive Antenna and Waveguide

To generate the 180° out of phase harmonic trap drive components and to act as a narrow RF bandpass filter, an RF meander line waveguide resonator is used to drive the trap [33]. This is coupled to using a loop antenna of approximately 25mm diameter, positioned on an XYZ stage for fine adjustment of the coupling. A directional coupler prior to the antenna allows monitoring of the reflected signal, which is minimized to ensure critical coupling of the antenna to the resonator. An rf drive power of approximately 0.35 W. A diagram of the coupling geometry is shown in Figure 2.7.

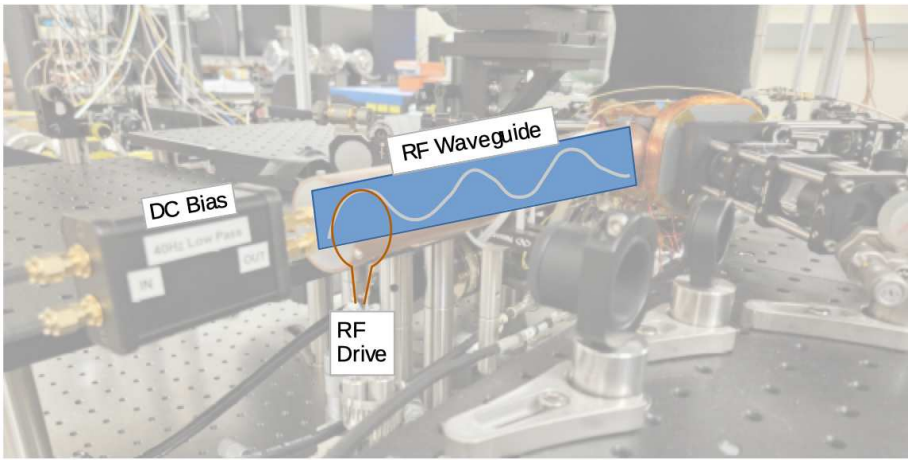

Figure 2.7: A diagram of the waveguide and loop antenna used to provide the RF trap drive components for radial confinement. The opposite side of the waveguide produces the second component with opposite phase.

2.1.6 Microwave Transition RF Loop Antenna

A 50 mm diameter rf loop antenna is positioned about 1 mm above the fluorescence collection window, outside the vacuum chamber above the trap. This is used to drive all

microwave transitions between the $|F, m_F\rangle$ states in the ground $^2S_{1/2}$ manifold. The frequencies and pulses are generated by an externally referenced ARTIQ control system on an AD9912 DDS channel, with a resolution of 4 μHz. The base rf frequencies are quadrupled to reach the required range of $\nu \approx 1.25$ GHz. This is then amplified and filtered for suppression of harmonic components. The π-times for ground state transitions with the available RF power are approximately 100-400 μs.

2.1.7 Magnetic Field Stabilization

A laser diode current controller (Thorlabs LDC500) is used to set the quantization axis magnetic field using a set of magnetic field coils located just outside the vacuum chamber. A convenient feature of the LDC500 is the analog input that can be used to feedback onto the output, using control signal from the ARTIQ control system. This was used in the Ramsey spectroscopy measurement of the $^2S_{1/2}$ ground state hyperfine splitting to correct for small ($\approx$ mG level) ambient magnetic field drifts. Current to the two other sets of coils is used to null the off axis fields, and is applied with a low noise current and voltage controller.

2.2 UV Laser Systems

Several specific frequencies near 313 nm need to be generated for far-detuned and near-detuned Doppler cooling and resonant state detection. The basic scheme relies on frequency quadrupling lasers operating at $\lambda = 1252$ nm. This allows the laser to be locked to an optical frequency comb (OFC) in the IR while being a reliable method to generate the required 313 nm laser light.

For this work, we used two 1252 nm lasers. One is a Toptica external cavity diode laser (ECDL) with a tapered amplifier (TA) output coupled to single mode fiber. The other laser is a Vexlum vertical external cavity surface emitting laser (VECSEL). The ECDL is used for Doppler cooling and D_2 state detection and spectroscopy. The VECSEL is used for

D_1 spectroscopy and (separately) for driving far detuned Raman sideband transitions. The further details are provided in the following subsections.

2.2.1 VECSEL vs ECDL

The Toptica ECDL is an established commercial system, and the performance parameters were fairly well understood. The system requires minimal adjustments of the fiber coupling and fine tuning of the grating angle and piezo voltage to achieve the desired output frequency.

Since the VECSEL is a recently developed commercial laser system, we performed additional characterization to verify the stability, linewidth, beam profile and other parameters. It was expected that the combination of the higher optical output power in the IR and the naturally circular Gaussian mode would ultimately lead to significantly improved UV optical power compared to the ECDL with tapered amplifier. A spatial profile of the VECSEL taken early in testing is shown in Figure 2.8. Divergence data taken at two different dates, along with manufacturer estimates are shown in Figure 2.9.

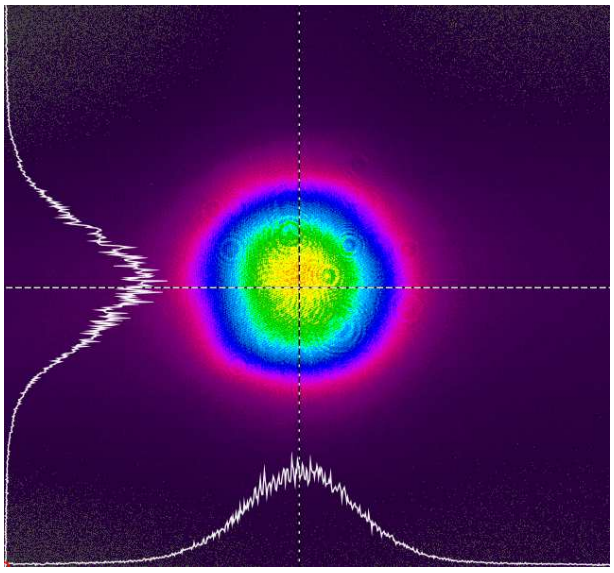

Figure 2.8: Sample beam profile taken with a CCD beam profiler during initial testing of the VECSEL.

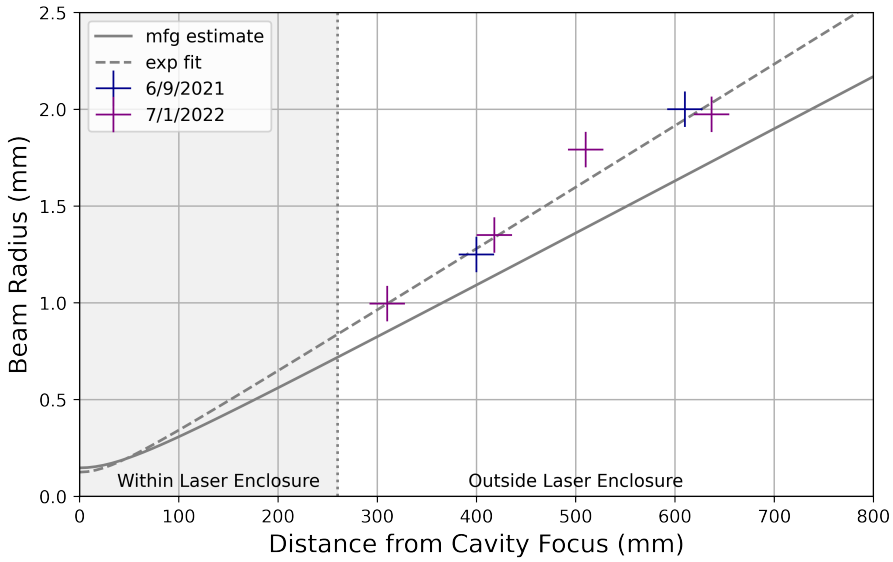

Figure 2.9: Divergence data for the VECSEL compared to manufacturer estimated values.

Fiber coupling of the VECSEL was done with extra care, using Zemax simulations and experimentally testing several separate lenses. In this laser design there is relatively large divergence of the beam from the cavity output aperture. It is large enough that the distance from the output at which the fiber coupling is performed significantly affects the coupling efficiency, in combination with the specific lens chosen. In retrospect, addition of a long focal-length lens (f $\approx$ 300 mm) at the output of the VECSEL would have been helpful to reduce the divergence, at the expense of a few percent extra loss. The final configuration for fiber coupling used a Thorlabs achromatic doublet (AC080-30-C) placed 650mm from the output and achieved about 70% efficiency. Two Thorlabs IO-4-1220-VLP isolators were also added in series prior to fiber coupling, which together reduced the available optical power by about 6%.

2.2.2 1252 nm to 626 nm Waveguide Doublers

The first stage doubling was done in single pass fiber coupled Lithium Niobate ($LiNbO_3$) waveguide doublers (NTT WH-0626-000-A-B-C), which require only the temperature to be adjusted to achieve the phase matching condition, and the correct linear polarization

launched into the PM fiber. Test data for the ECDL is shown in Figure 2.10, with VECSEL data shown in Figure 2.11.

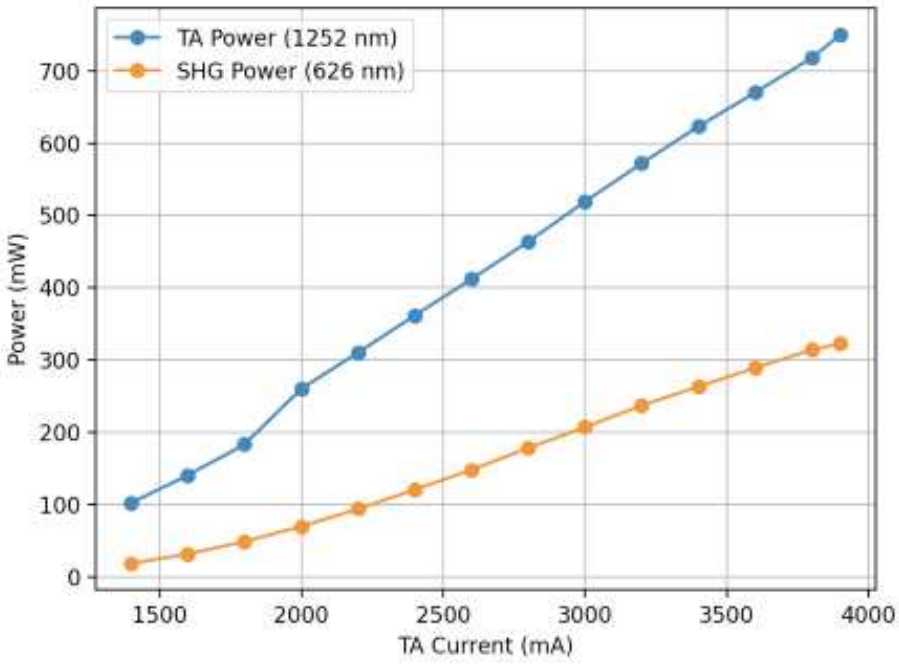

Figure 2.10: Conversion efficiency data for a 1252nm to 626nm single pass Lithium Niobate waveguide doubler, taken using the Toptica ECDL.

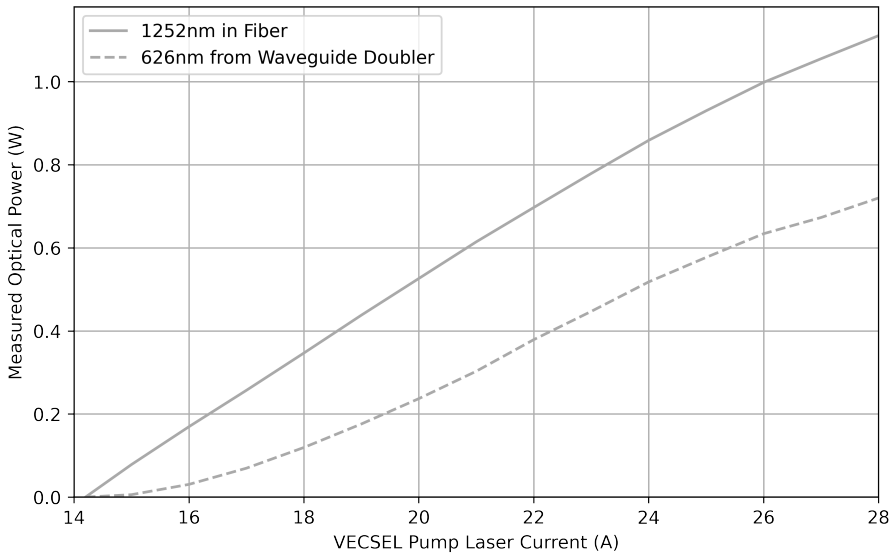

Figure 2.11: Conversion efficiency for the VECSEL, fiber coupled to the second Lithium Niobate waveguide doubler.

The maximum optical power available from the VECSEL in the red at 626 nm after the waveguide doubler (700 mW) was roughly double the maximum when using the Toptica ECDL (320 mW). The fiber coupled VECSEL could reach the maximum rating of the waveguide doublers, which became the limiting factor for that system.

Light at 626 nm from the waveguide doubler is output to free-space. Careful fiber coupling was performed for both lasers, into polarization maintaining single mode fiber (OZ Optics PMJ-3A3A-633-4/125-3-5-1). The beam diameter at the output of the waveguide module indicates a short focal length lens is optimal for mode matching into standard 0.1 numerical aperture fiber. The first configuration tested was a Thorlabs 4 mm focal length achromatic fiberport (PAF2-A4A), which achieved 68.3 % efficiency. This was later replaced with Thorlabs 2 mm focal length aspheric fiberport (PAF2-2A), which achieved a measured fiber coupling and transmission efficiency of 91.7 %. This coupling efficiency is nearly perfect, after accounting for roughly a 3.5 % Fresnel loss at each of the two uncoated fiber facets.

2.2.3 626 nm to 313 nm Resonant Doubler Designs

Since the phase matching and transmission properties of $LiNbO_3$ are not suitable for the second doubling from 626 nm to 313 nm, there are no waveguide doublers available and a resonant cavity with Beta-Barium-Borate: β-BaB_2O_4 (BBO), is the standard choice. The resonant cavity is necessary to amplify the electric field strength, as second harmonic generation (SHG) is a second order effect. The well known paper on SHG by Boyd and Kleinman [34] provides the necessary framework to calculate the optimal beam parameters for maximum single pass conversion efficiency, given fundamental material characteristics such as birefringent walk-off at the phase matching angle. A further generalization to elliptical beams is given in [35]. A cavity that produces the appropriate waist(s) (or focusing parameter(s)) can be designed using Gaussian beam ABCD matrix formalism [36], valid in the paraxial approximation. A schematic diagram and matrices for a bow tie cavity are listed in Figure 2.12. Total conversion efficiency can be calculated by considering the cavity

buildup factor. A detailed discussion of cavity enhanced UV laser light generation can be found in the thesis of Zak Burkley [37]. This ultimately depends on factors like round trip cavity loss, input coupler reflectivity and mode matching of the input beam to the secondary waist.

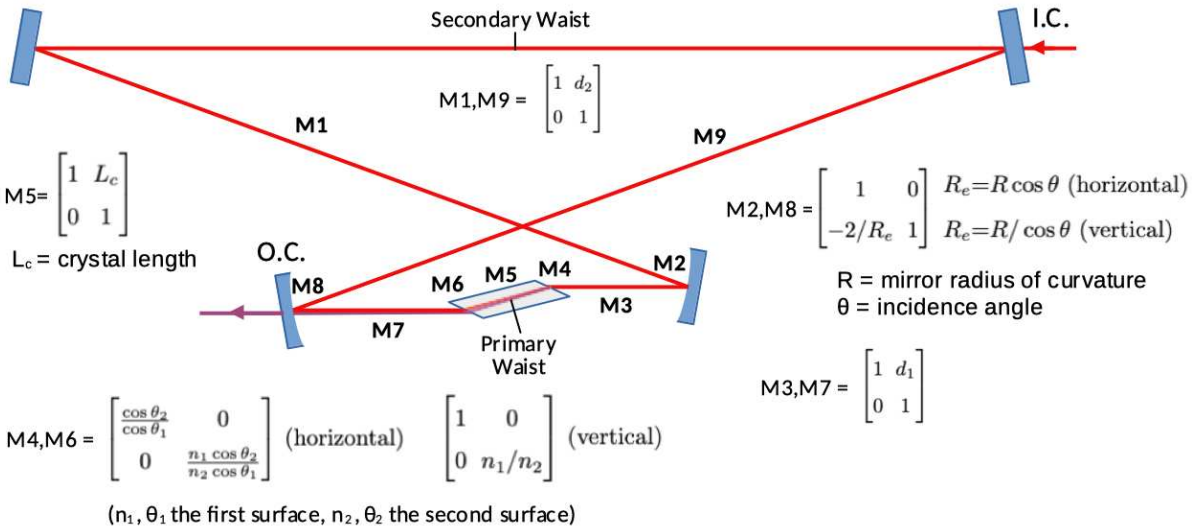

Figure 2.12: Bowtie cavity schematic and ABCD paraxial propagation matrices for calculating the resonant mode. d_1 is the curved mirror to facet distance, while d_2 is the half long arm distance from curved mirror to secondary waist. Input coupler (I.C.) and output coupler (O.C.) Other parameters are labeled in the figure. Horizontal and vertical axes have different matrix components and are calculated independently.

The two UV doubling cavities developed here were based on a well-tested design using a Brewster-cut BBO crystal [38], optimized for high power applications (750 mW at 313 nm) at NIST. In our experiments, we require at most 20-50 mW from each doubler. One doubler was based on the original design with a Brewster-cut BBO crystal, with only minor cavity optimizations. This system was used for the Doppler cooling and detection applications. The second doubler implemented a new cavity design, using a flat facet dual AR-coated BBO crystal. Flat-facet cavity designs had been used previously for systems at other wavelengths, and this choice allowed us to directly compare the two approaches for 313 nm SHG generation in BBO. The most significant advantage of using a flat-facet AR coated crystal is the elimination of the significant UV loss at the output Brewster facet, where the UV polarization is

orthogonal to the fundamental. This loss is about 22% for 626-313 nm SHG in Brewster cut BBO. Cavity alignment and phase matching optimization is also simpler without the large refraction angles, and the hygroscopic BBO facets are moderately protected from long term degradation from ambient humidity.

Both cavities were designed for type II $o + o \rightarrow e$ second harmonic generation (SHG) from 616 nm to 313 nm in BBO. The phase matching angle is 38.4°, with effective refractive index of 1.6676. Brewster's angle is 59.05°. The birefringent walk-off, ρ, is 80 mrad. The relatively large walk-off puts the optimal focusing parameter at the Boyd-Kleinman asymptotic limit of 1.39 assuming a symmetric beam [34]. An elliptical beam can give slightly improved conversion efficiency [35]. For a negative uniaxial crystal, however, the ellipticity originating from the refraction of the fundamental at Brewster's angle is in the incorrect axis, so decreasing this ellipticity source is an advantage.

An image of the two cavities is shown in Figure 2.13 and design parameters are summarized in Table 2.1. The cavities both use a bow-tie configuration. A shallow folding angle is optimal for the flat facet cavity, but it was not reduced below 20° to allow sufficient clearance around the kinematic mirror mounts. This still has plenty of overlap in the stability diagrams for the horizontal and vertical modes, but has the effect of making the second waist slightly elliptical. A plot of the stability diagrams are shown in Figure 2.14. The two BBO crystal types (and also flat facet BiBO crystal to test) were purchased together in one batch from Castech, Fujian China. The mirror sets were produced in one batch with electron beam evaporation using existing coating designs from Laseroptik, GmbH. Both cavities typically receive an O_2 purge while actively running and no N_2 purge.

A plot of the output power generated from each cavity is shown in Figure 2.15. The main performance advantage of the flat facet cavity comes from the lack of the large Fresnel loss at the output facet of the crystal. The crystal waist optimization is also slightly better. The two designs were tested initially with up to 200 mW of input power at 626 nm. The flat facet cavity was additionally tested one year later with up to 350 mW after occasional use.

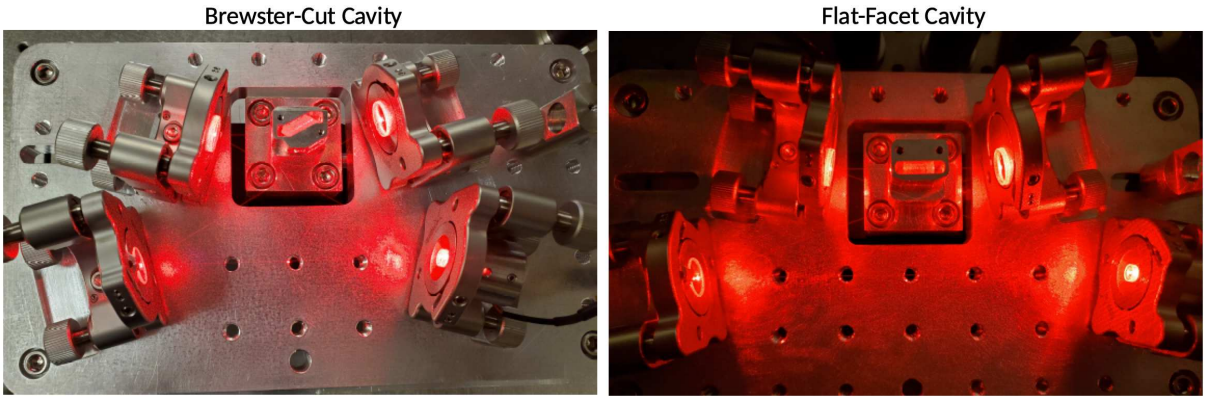

Figure 2.13: Images of the bow-tie and flat facet cavity designs.

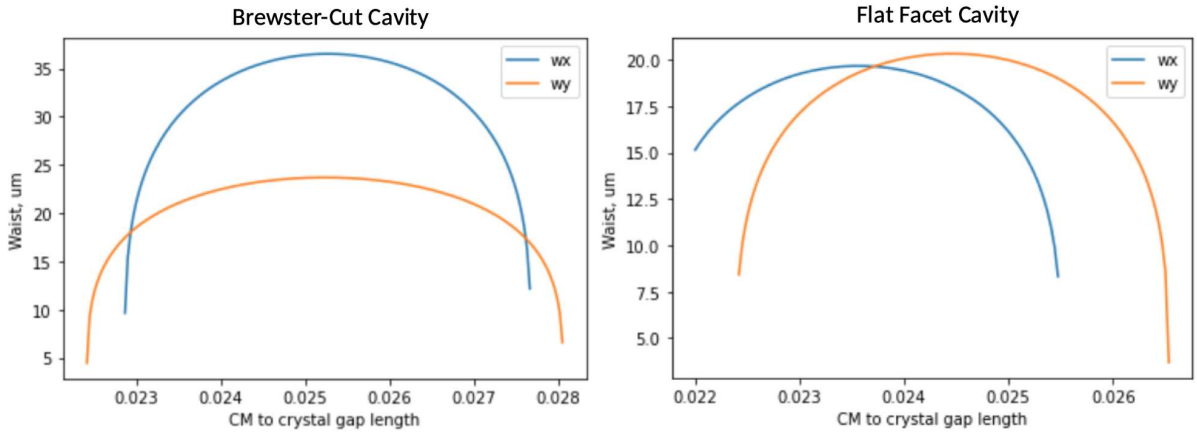

Figure 2.14: Plots of the stability diagrams for Brewster-cut and flat facet cavities, versus distance in meters from curved mirror (CM) to crystal facet. For a stable mode to exist, there must be overlap between the x and y dimensions. The calculated waist dimensions of the intra-cavity mode are shown. In the Brewster cavity, the astigmatism from the Brewster facets is compensated for by astigmatism in the folding angle incidence on the curved mirrors. In the flat facet cavity there is no astigmatism at the crystal facets, so a more shallow folding angle is appropriate. At a folding angle of 20° there is plenty of overlap. The intra-cavity mode is less elliptical in x, which is slightly beneficial for single pass conversion efficiency in a negative uniaxial crystal.

The conversion efficiency of the flat facet cavity was maintained at a similar level despite minimal purging. The Brewster-cut cavity was used and adjusted more frequently over the same time period and as such an exact long term comparison is difficult. The general trend with the Brewster cut cavity was a gradual loss in optical power output of roughly 30% and occasional need to translate the crystal to partially regain performance. It isn't certain whether this is solely related to the hygroscopicity of BBO, or some other effects.

Table 2.1: Design parameters for the Brewster cut and flat facet cavity designs. Note that x and y in the waist dimensions refer to horizontal and vertical planes, respectively. In terms of the crystal axes, x and y are the sagittal and tangential planes.

Design Parameter	Brewster	Flat Facet
Mirror to Facet Distance (mm)	25.3	24.2
Crystal Length (mm)	10	10
Full Long Arm Distance (mm)	290	361
Mirror Radius of Curvature (mm)	50	50
Input Coupler Transmission (%)	1.6	1.6
UV Reflection at Facet (%)	22	$\leq$0.1
Folding Angle (deg)	30.5	20.0
Crystal Waist ($w_x \times w_y$) (μm)	36.5 $\times$ 23.7	19.1 $\times$ 20.3
Second Waist ($w_{x_2} \times w_{y_2}$) (μm)	154 $\times$ 152	149 $\times$ 187
Focusing Parameters (ξ_x , ξ_y)	0.45 , 1.06	1.63 , 1.46

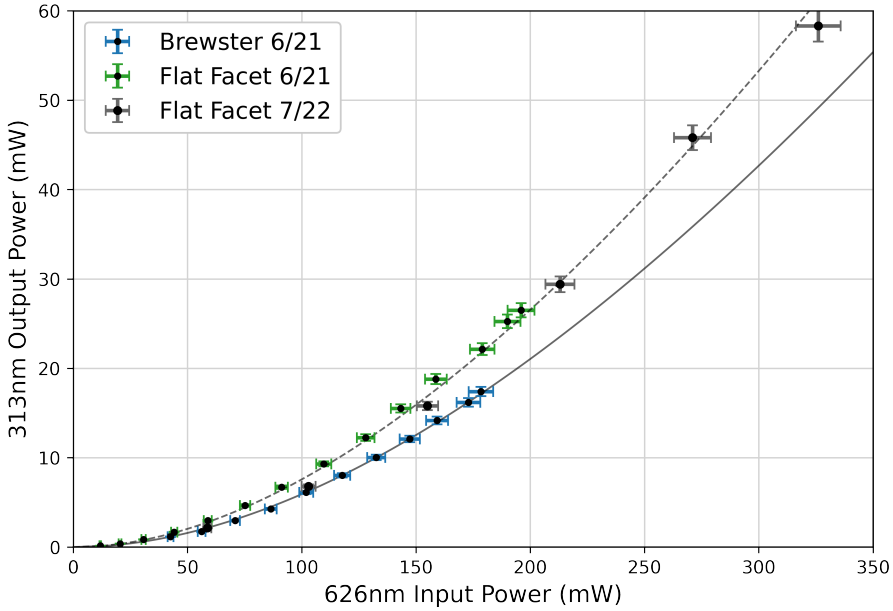

Figure 2.15: The conversion efficiency results are shown for both cavities. Results 1 year later and up to higher input power are included for the flat facet cavity design. The 626nm light is collimated from a polarization maintaining single mode fiber, passed through a polarizing prism and focused to the second waist with a single plano-convex lens of suitable focal length for mode matching in each case. The lens is on an xyz stage for fine tuning after the main cavity alignment. Calculated conversion efficiency is shown for each (Brewster Facet as solid line, Flat Facet as dashed line), using approximate values for the mode matching and intra-cavity build up factors. Note that the mode matching is lower for the flat facet design design due to the slight ellipticity of the second waist, which could be further optimized using two cylindrical lenses instead. The single lens configuration was chosen for simplicity and more direct performance comparison.

2.2.4 Mode Matching and UV Output Collimation

For efficient frequency conversion, the 626 nm input to the resonant cavity needs to be spatially mode matched to the cavity. Typically, this requires matching the input beam's focus through the input coupler to the cavity's larger second waist. The dimensions of the cavity resonant mode are obtained during cavity design, with the waist radii listed in Table 2.1. The input coupling implemented was the same for the two cavities used in this work. The 626 nm light from the first stage doubling is collimated upon exiting the PM fiber patch cable (OZ Optics PMJ-3A3A-633-4/125) using a Thorlabs fiberport (PAF2-A4A), which uses a 4 mm focal length achromatic doublet lens. The beam is passed through a polarizing beamsplitter cube to ensure the correct polarization (horizontal for the BBO cavities, particularly if using Brewster cut facets) then focused to roughly a 150 μm waist with a 300 mm focal length plano-convex singlet lens (Thorlabs LA1484-A). Although the second waist of the flat facet cavity is slightly elliptical, we chose to use a single lens for simplicity. The reduction in overall expected conversion efficiency with the single lens is minor, while the practical implementation is much more straightforward than introducing an additional cylindrical lens.

The relatively large walk-off in BBO results in what is effectively collimation of the generated UV output in the vertical axis. In simulation, the spatial profile in the walk-off axis is more like a Gaussian stretched toward a top-hat profile, but in any case only a single cylindrical lens is necessary to collimate the horizontal non-walk-off axis at the doubler output. For this purpose, an Edmund optics cylindrical singlet with 75 mm focal length was mounted in a customized holder near the output.

2.2.5 Piezo Stack Assembly

The piezo stack used to lock the cavity to resonance is Thorlabs PK4FA2P2 (4x4x9 mm, 750 nF, 0-150 V with 63 nm/V displacement). This is mounted on a tapered copper puck,

back filled with lead to suppress mechanical resonances, following the designs described in [39]. The cavity mirror is attached to the top of the piezo stack using quick-drying epoxy. The mirror substrate dimensions are 6 mm diameter by 2 mm thick. A diagram of the assembly is shown in Figure 2.16. The voltage required to scan over one wavelength with this stack is approximately 10 V. It would be possible to use a shorter stack for higher lock bandwidth, at the expense of higher voltage requirements.

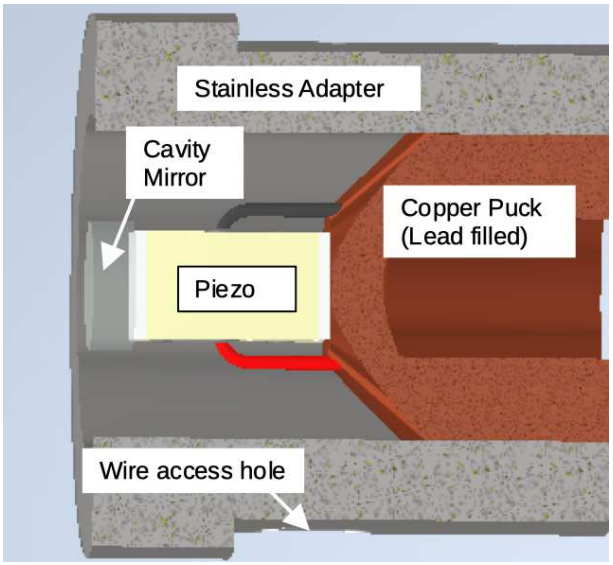

Figure 2.16: The full piezo and mirror assembly used in the UV doublers is shown in the figure. The piezo stack was epoxied to a tapered copper puck back filled with lead to suppress mechanical resonances. The 6mm diameter x 2mm thick cavity mirror was epoxied to the opposite side. This was then housed in a stainless steel tube with 1" outer diameter to mount to the 1" Thorlabs Polaris kinematic mirror mount in the cavity. The design was adjusted from previous versions to put the mirror surface at the pivot point of the Thorlabs kinematic mount, rather than sticking out to eliminate lateral walk when aligning.

2.2.6 UV Doubling Cavity Lock Electronics

Both resonant doublers are locked using the Hansch-Couillaud method of polarization spectroscopy of the cavity reflectance [40]. The original paper on the topic from 1980 describes a confocal cavity with an intra-cavity polarizer, with linear input polarization oriented at 45°. The reflected beam acquires polarization ellipticity from this configuration, which can

be decomposed to generate an error signal using a quarter waveplate, polarizing beamsplitter and a balanced detector. A Brewster cut crystal SHG cavity is similar to this configuration, though with the incoming polarization angle nearly aligned with the Brewster facets which act as a partial polarizer. The BBO crystal introduces a birefringence such that there is an offset in the resonance between the two polarization orientations. A flat-facet cavity has little to no polarization dependent loss of the perpendicular component, though in practice this configuration still produced a suitable error signal for locking. The balanced detector model used in these experiments was Thorlabs PDB210A, using silicon photodiodes each with 5 mm active diameter and up to 1 MHz bandwidth.

Two separate FPGA-based solutions for providing proportional integral derivative (PID) servo control of the cavities were successfully implemented. The first, which was used for all of the data prior to the rare isotope work, was the NIST/Leibrandt digital servo lock box (https://github.com/nist-ionstorage/digital-servo). This provides two analog outputs and two analog inputs, with high voltage support up to the HV supply of 50 V. In practice we required only the lower voltage output (0 to +10 V). The second solution, which we implemented first in late 2023, uses a RedPitya STEMLab 125-14 module that is controlled with the pyRPL library written at TU Darmstadt (https://github.com/TU-Darmstadt-APQ/RedPitaya-Lockbox). We used this first with just a simple 20x piezo amplifier, but later with replica back plane boards following their design. For reference, a compatible set of Python libraries implemented here were Anaconda 2020.02, pyqt 5.12, pyqtgraph 0.12, numpy 1.19, quamash 0.6.1, and RedPitaya firmware 0.98. The laser was locked by simple manual sweep to find the peak, then engaging the PID feedback on the same output channel. A screen capture of the successful lock settings are show in Figure 2.17. Note that there is a multi-stage filtering available on the input. The most successful setting in our case utilized one low frequency filter (20 Hz) and one higher frequency filter (2.5 kHz). This contrasts with the NIST lock box settings which we typically had set at about a 20-30 kHz 3dB roll off.

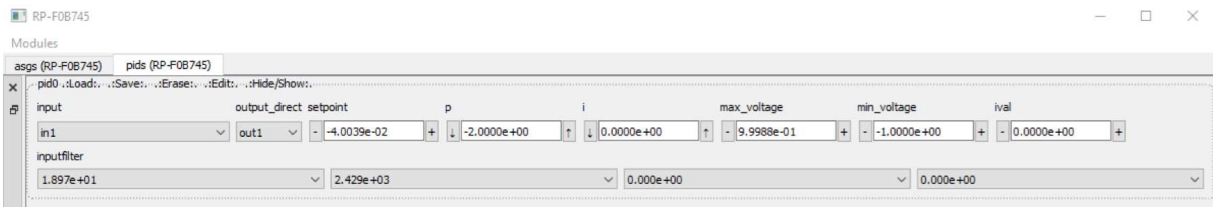

Figure 2.17: The settings which were successful for locking the resonant UV doubler with the STEMLab 125-14 with pyRPL are shown. Note that the software assumes the default -1 to 1 V output range, but after the voltage offset modification described online the corresponds range is actually 0-2 V. The output is also sent through a 20x piezo amplifier for this initial test.

2.2.7 AOM Shifting of UV Frequencies

The ECDL laser frequency is stabilized between the D_2 resonance for the two ground state hyperfine sublevels ($F = 2, 1$), then acousto-optic modulators (AOMs) in single and double-pass configurations are then used to fine tune the laser frequency to generate the specific components needed for cooling, state preparation, and detection. Double pass configurations with cat-eye geometry are used for all spectroscopy beams [33]. This helps to suppress beam pointing variation as a function of the AOM drive frequency. We also use spatial filters and power stabilization feedback to maintain uniform intensity at the location of the ion when performing measurements. A diagram of a double pass cat-eye AOM configuration is shown in Figure 2.18. For simplicity and space considerations, we used a single reflection configuration. Since the UV AOMs used here for 313 nm are highly polarization sensitive, the typical method of separating beams based on polarization was not feasible. While a cylindrical lens might be the most appropriate choice for the cat-eye, for convenience we used a plano-convex singlet with flat side facing the mirror, aligned along the axis of the first-order beam. In addition, spatial filtering and power stabilization of the light delivered to the ion after the frequency shifting in the AOM reduces the requirements on the double-pass performance.

Measured beam profiles approximately one meter from the double pass AOM are shown in Figure 2.19. The cat-eye configuration removes most of the beam pointing frequency dependence. In the test data, the residual beam pointing variation over 140 MHz total

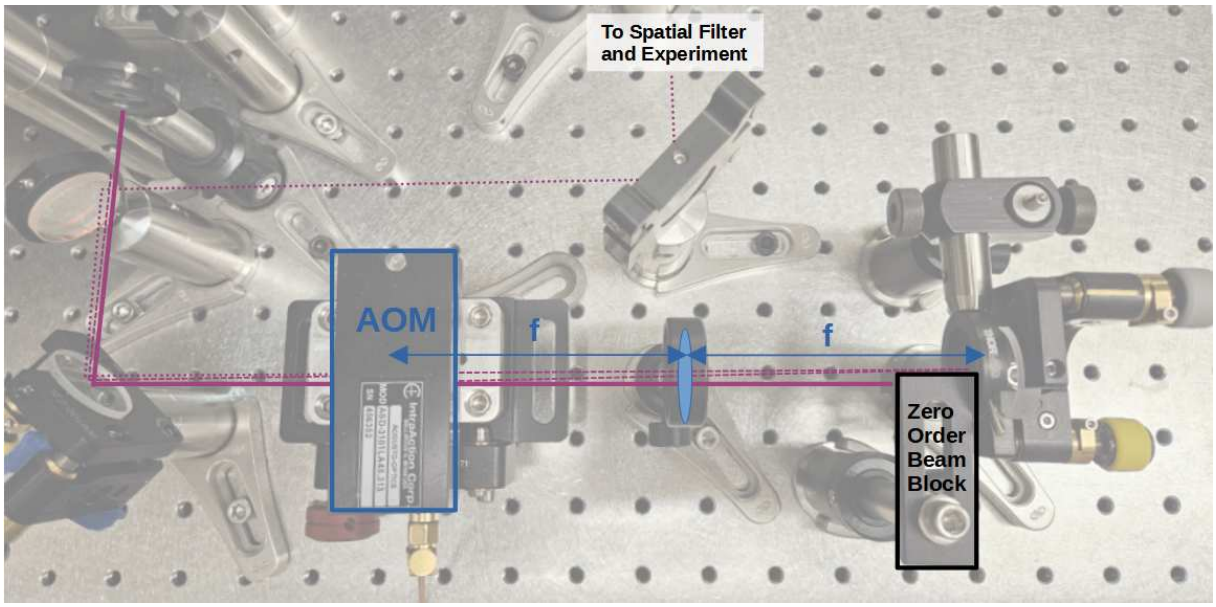

Figure 2.18: Double-pass cat-eye AOM configuration with single reflection. The lens is placed one focal length from the center of the AOM and also from the back mirror. The zero order beam on each pass is removed such that only the component refracted twice is sent to the experiment. Some frequency dependence in the partial clipping of the first order beam on the zero-order beam block can be a hidden variable to look out for in the overall output power frequency dependence.

frequency shift range was approximately 20 μrad. A single pass configuration over the same frequency range would have 7.5 mrad of beam pointing shift. Identical measurements after installing a pinhole spatial filter (discussed in the next section) are also shown.

For D_1 measurements, or for driving Raman sideband transitions, the VECSEL frequency is set either near the D_1 transition frequency or ≈ 50 GHz red-detuned (in the UV) from the D_2 transition. A combination of AOMs was used to span the 1.25 GHz ground state splitting for the Raman transitions. Other elements like spatial filtering and power stabilization were identical to the ECDL setup. The main difference was that in addition to σ^- beams, π polarization beams from either side were required to drive specific transitions and address both axial and radial secular modes.

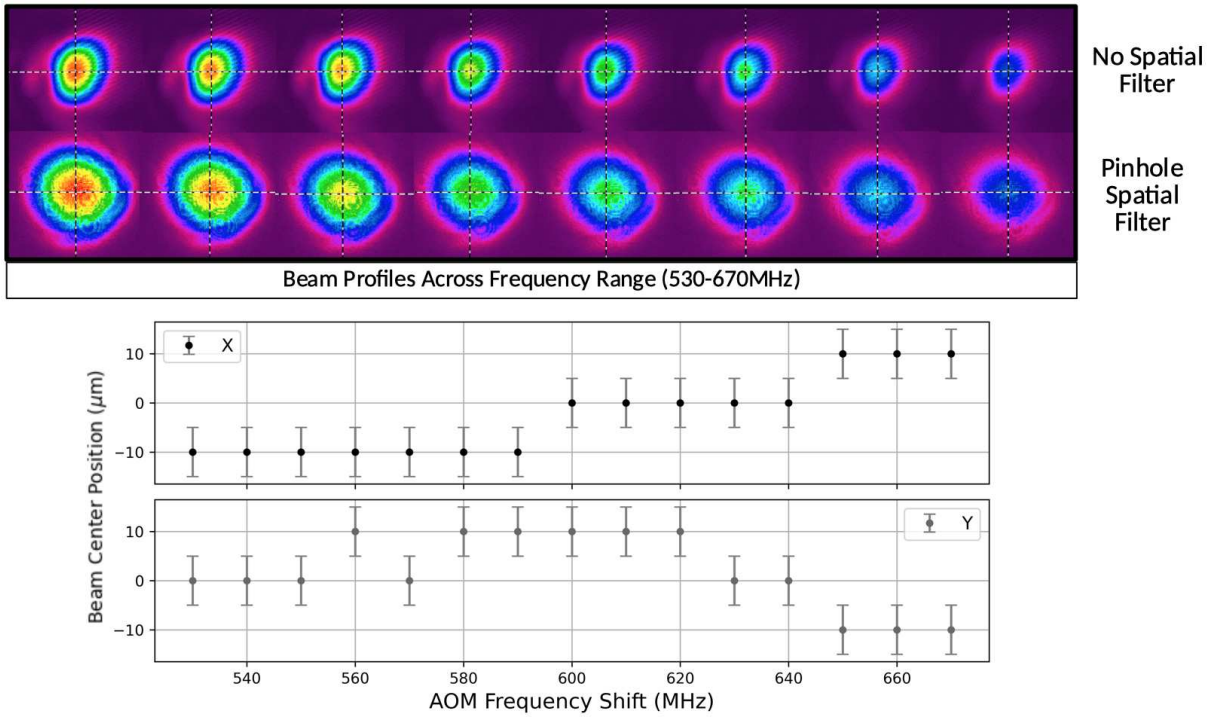

Figure 2.19: Beam pointing stability test data from the D_2 side double-pass cat-eye AOM, at a distance of 1 m. The beam pointing (just from the cat-eye double pass AOM without any spatial filtering) was stable over the 140 MHz frequency range to ≈20 μrad. This is a significant improvement compared to the beam pointing shift in a single pass configuration of approximately 7 mrad over the same frequency range. Profiles taken with a pinhole spatial filter (after the AOM) are also shown to demonstrate the improved spatial uniformity versus frequency.

2.2.8 UV Single Mode Fiber and Pinhole Spatial Filters

Since the spatial mode from the resonant UV doublers is somewhat astigmatic and elliptical, and various effects associated with the AOMs can occur, a spatial filter was used to improve beam uniformity prior to sending light to the ion. Single mode fiber is generally the most reliable option to produce a highly uniform and near-Gaussian profile, but step-index fibers for UV wavelengths are uncommon. We used 6 inch patch cables of Thorlabs SM300 fiber, which has a cutoff wavelength specification of $\leq$310 nm. Input coupling was done with a 6 mm diameter, 10 mm focal length UV-AR-coated plano-convex lens (Edmund Optics 89-415). The achieved coupling efficiency was 33%. We considered this efficiency acceptable given the many imperfect conditions such as beam ellipticity, astigmatism, aberrations, imperfect numerical aperture match, and alignment sensitivity for the fiber mode field diameter

(MFD) of only 2-2.4 μm. An 8 mm focal length aspheric lens (Edmund Optics 87-977) was also tested later, but the efficiency achieved was ultimately worse from the thicker optic and the very short back focal length of 2.5 mm was challenging to work with.

While the beam profile from the fiber was quite good, we observed gradual photo-darkening and the fiber had to be replaced after about two months of occasional low optical power use ($\approx$ 0.1-5 mW). Hydrogen-loading and UV curing the has been shown to reduce photo-darkening in UV photonic crystal fibers [41, 42], though it hasn't been tested in this particular step-index fiber. As an alternative, a pinhole spatial filter was tested for the D_1 and D_2 absolute frequency measurements, with agreement within statistical uncertainty. This configuration was then used for measurements of the unresolved $^2P_{3/2}$ hyperfine splitting.

2.2.9 Optical Power Stabilization Summary

To maintain uniform intensity at the ion as the AOM drive frequency is adjusted, it is necessary to apply feedback to the AOM drive power to maintain a fixed optical power. This was measured by sampling the beam on an amplified photodiode detector. The optical power of the twice-diffracted beam from the cat-eye AOM using a fixed AOM drive voltage is shown in Figure 2.20.

To compensate for the frequency dependent diffraction efficiency, the AOM drive power is adjusted at each frequency point. A sample-and-hold technique is used, where a small fraction of the spectroscopy laser light is sampled prior to each measurement to generate the feedback. This is performed after spatial filtering to simultaneously account for both diffraction efficiency and residual beam pointing frequency dependence. This also automatically compensates for any slow drift in the UV optical power from the resonant doubler. Data showing the final sampled photodiode signal and applied AOM drive power after feedback loops for a D_2 measurement is shown in Figure 2.21. While the uncorrected optical power may decrease by more than 50% over the scan range, with slow feedback this can be reduced to at least better than 3% across the full range and typically less. This general scheme

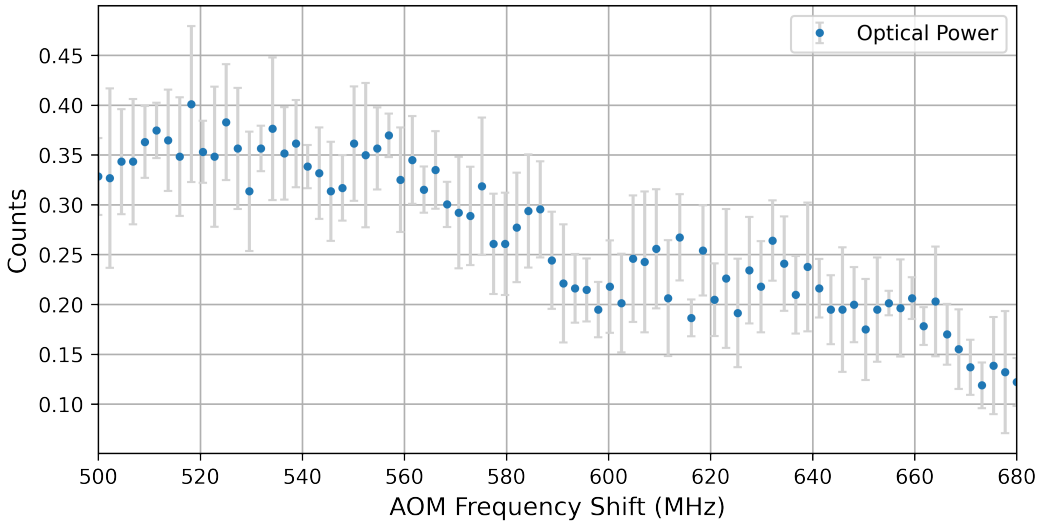

Figure 2.20: A plot of the measured optical power in the refracted beam from a double pass AOM configuration is shown, using a fixed drive voltage from the ARTIQ control box. The result includes the overall frequency dependence in the AOM diffraction efficiency and the RF amplifier, and any clipping of the first order beam on the initial pass zero order beam block.

was applied in all spectral measurements of the strong transitions and further details are provided in the individual sections below.

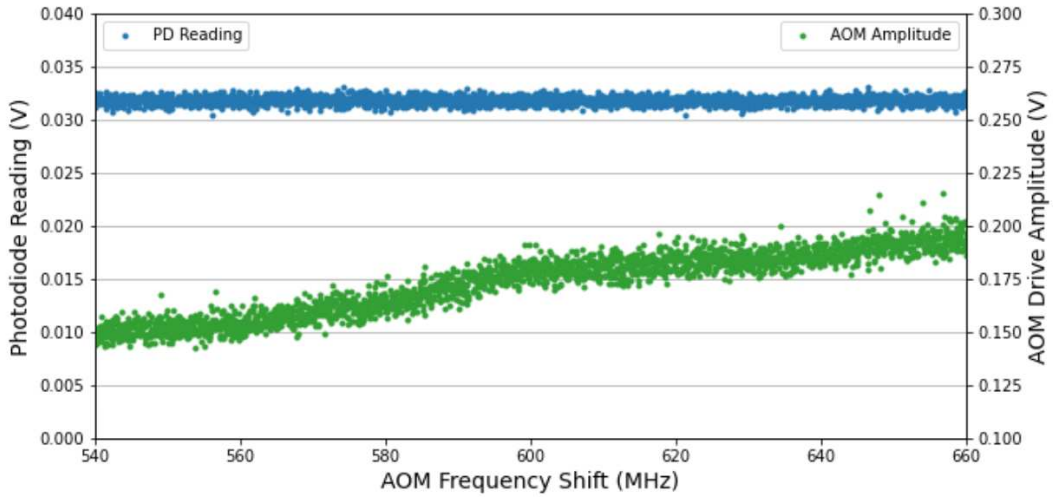

Figure 2.21: Optical power stabilization of the spectroscopy laser. Photodiode signal is shown in blue, with the (un-amplified) AOM drive amplitude in green. The optical power is stabilized to better than 3% across the full scan range.

2.3 Fluorescence Imaging System

A 0.39NA imaging system was used to collect fluorescence to the CCD camera (Photometrics Prime 95B UV) and PMT (Hamamatsu H10682-210). A diagram of the full system is shown in Figure 2.22. A pair of 0.39 NA fused silica aspheres (Asphericon AFL50-60) make a 1 to 1 imaging relay to a 100 um pinhole, which reduces the lateral field of view and allows some confocal-imaging-like suppression of out of focal-plane scatter. A 200 μm pinhole was typically used for initial trapping, due to the larger field of view, and was later replaced with the 100 μm pinhole for the $^9Be^+$ measurements. The pinhole and ion are imaged using a 40x infinity corrected UV objective (Thorlabs LMU-40X-UVB). A 250 mm lens (Thorlabs LA4158-UV) forms the final image, which is filtered just prior to detection with a 313 nm bandpass filer (Edmund Optics 34-977) with transmission $\geq$75%. The PMT quantum efficiency at 313 nm is approximately 0.317 and objective transmission approximately 0.92. Taken together, including integration of a 0.39NA field of view perpendicular to a sigma dipole radiation pattern and all other optical surface losses, the approximate total detection efficiency is 0.265%. Thus, in typical D_2 data where we collect on average around 0.45 PMT counts at the peak, the calibrated total number of scattering events is approximately 160. This detection efficiency is consistent with the saturation parameter measured using the ion.

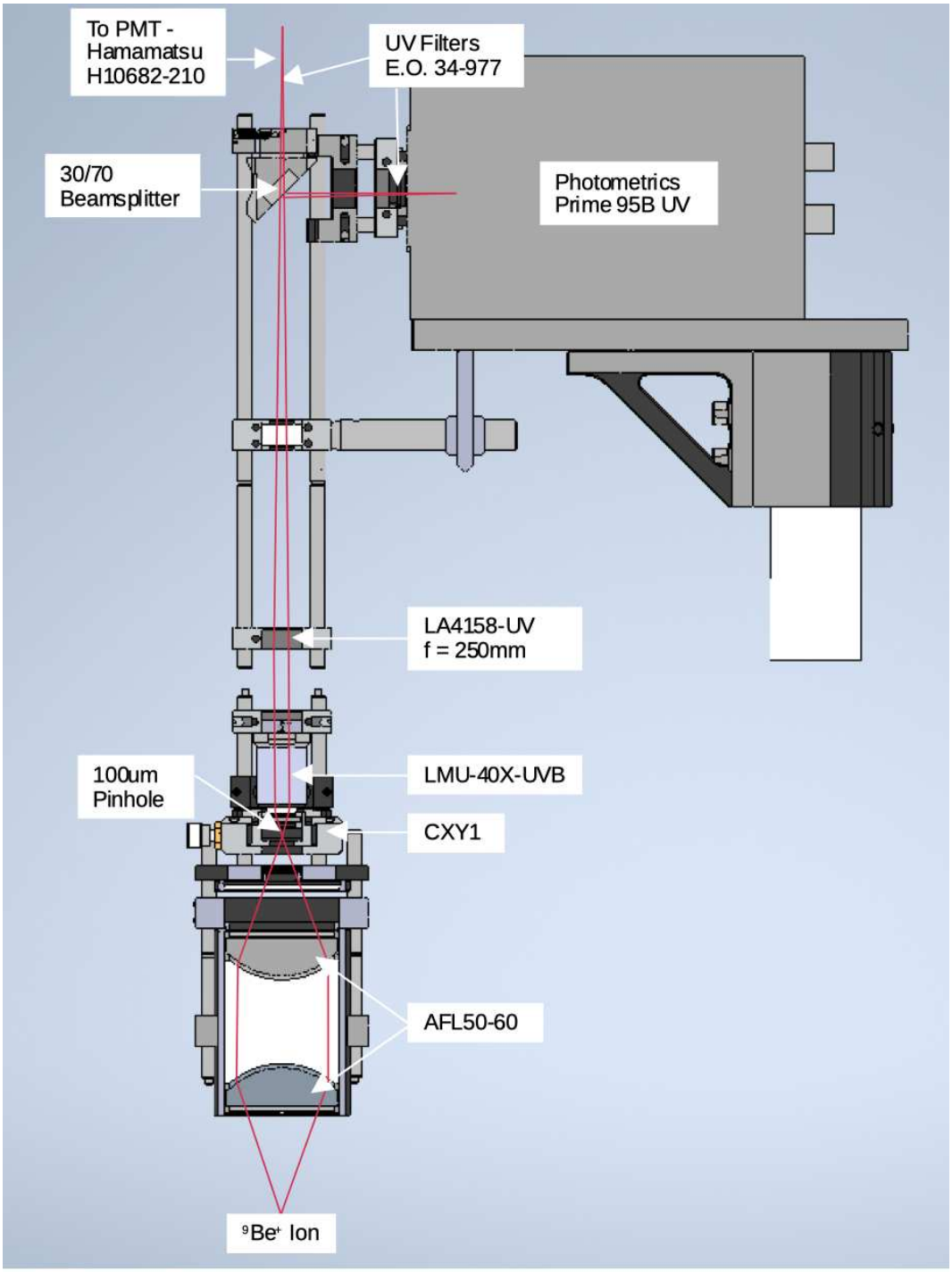

Figure 2.22: A CAD model of the imaging system assembly is shown in the figure. Major components are labeled. Two aspheric lenses create a 1 to 1 imaging relay of the ion fluorescence to a 100 μm pinhole, which is then imaged by a single lens to the both the camera and PMT. UV filters greatly reduce the ambient light background. The assembly is then wrapped loosely in black felt to further attenuate any background scatter. The beamsplitter was mounted in a removable mount to enable some experiments to have all the light going to the PMT.

Chapter 3

D_1 and D_2 Strong Transitions in $^9Be^+$

3.1 Introduction

Improved absolute frequency measurements of the D lines in $^9Be^+$ and extraction of the ^2P fine structure splitting and $^2P_{1/2}$ hyperfine constant were the first precision measurement objectives for the lab. The motivation was to both improve upon the previously achieved experimental values and to characterize the dominant systematic uncertainties in ion-trap-based measurements of strong transitions. Working with a single laser-cooled and trapped ion largely eliminates Doppler shifts which can introduce significant systematic uncertainty. In fact, the uncertainty in the cancellation of a large first order Doppler shift in the previous collinear laser spectroscopy experiments was the dominant source of systematic uncertainty and limited the accuracy of that work to ≈ 1 MHz [7]. The dominant uncertainty in our trap-based experiment was due to lineshape asymmetries caused by a change in the temperature of the ion during measurement (photon recoil heating). By applying short spectroscopy pulses, it was possible to characterize small residual effects on the spectrum. An optical frequency comb (OFC) was used for these absolute frequency measurements and was provided via optical fiber from Dylan Yost's group at CSU [43, 44]. The results described in this chapter were published in September 2023 in Physical Review Letters [45].

3.2 Measurement Configurations

Four separate D-line measurements were performed, including a conventional D_2 measurement of the σ^- closed cycling transition and three D_1 repump measurements. The configurations are shown in Figure 3.1.

At the beginning of each experiment, the ion is cooled using 1 ms of far-detuned ($\Delta/2\pi = -415$ MHz) laser cooling followed by 500 μs of near-detuned Doppler cooling

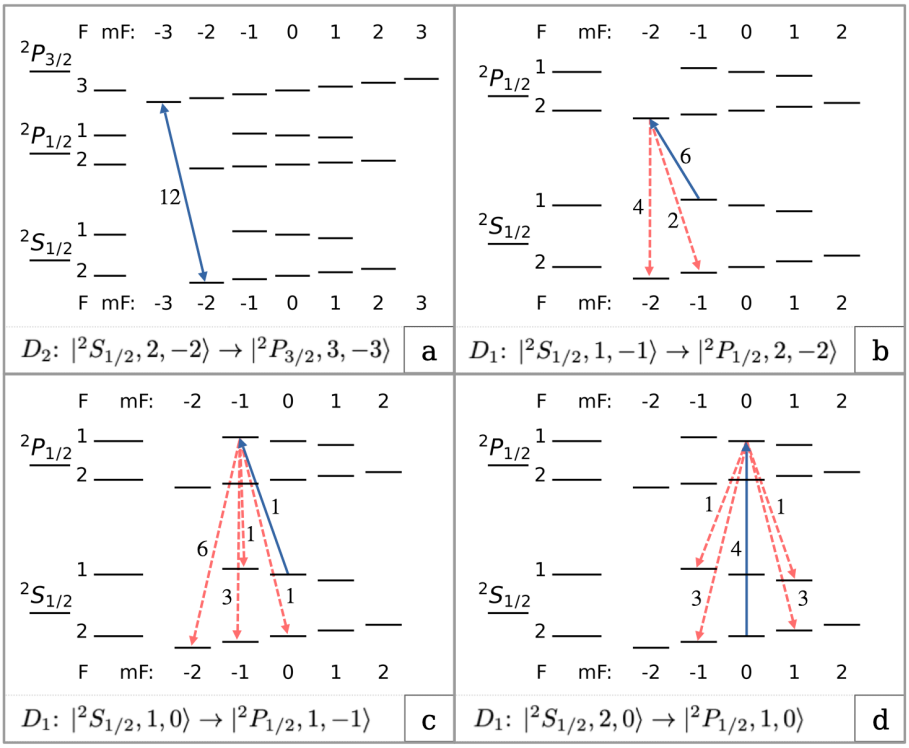

Figure 3.1: Schematics for the D_2 measurement (a) and three D_1 measurements (b,c,d). Transition strengths are listed for the excitation (solid blue) and decay channels (dashed red). Measurement (c) is the only measurement affected by quantum interference. To improve the measurement contrast in sequence (d), any population remaining in the $^2S_{1/2}\,|2,0\rangle$ state is transferred via a microwave pulse to $|1,1\rangle$, and the $|2,-1\rangle$ population is transferred to $|2,-2\rangle$.

($\Delta/2\pi = -10$ MHz) on the $|^2S_{1/2}, F = 2, m_F - 2\rangle \rightarrow |^2P_{3/2}, F = 3, m_F = -3\rangle$ cycling transition ($\Gamma/2\pi = 18$ MHz) [20, 21]. Periodically throughout the measurement campaign, the ion temperature was measured after Doppler cooling, using stimulated Raman spectroscopy [28]. The measured temperature was consistent with the Doppler cooling limit of $T_D \approx 0.5$ mK [29]. During the cooling sequence, the ion is optically pumped into the $|^2S_{1/2}, F = 2, m_F - 2\rangle$ state. A constant magnetic field of 0.0895(1) mT is applied along the quantization axis. The quantization field is determined by measuring the $|^2S_{1/2}, 2, -2\rangle \rightarrow |^2S_{1/2}, 1, -1\rangle$ microwave transition frequency, $\nu_{-2,-1} \approx 1251.9$ MHz, between each D-line measurement.

After Doppler cooling and state preparation, one of the four D_1 or D_2 measurements is performed. D_2 measurements (Figure 3.1, a) are carried out by counting scattered photons

on a photomultiplier tube (PMT) during a 250 μs spectroscopy pulse and a laser intensity corresponding to a saturation parameter of $S_0 = 0.02$. The optical power and exposure duration are chosen to limit lineshape distortion due to photon scattering when the laser detuning is set to the high-frequency ("blue") side of the D-line resonance.

D_1 measurements are performed using one of three measurement configurations shown in Figure 3.1, b-d. Each D_1 measurement begins with a microwave state preparation sequence which coherently transfers the atomic state population from the initial $|^2S_{1/2}, 2, -2\rangle$ state to a desired $|^2S_{1/2}, F, m_F\rangle$ state. A low-intensity ($S_0 \approx 0.02$) D_1 spectroscopy pulse is then applied. State detection is performed using a resonant D_2 laser pulse. This scheme allows for measurements between several initial and final $|F, m_F\rangle$ states and can be performed with negligible ion heating. D_1 optical power is attenuated to below approximately 5 nW and the pulse duration is adjusted between 10-100μs to minimize re-pump saturation broadening. From these three separate configurations we were able to extract the D_1 transition center of gravity, $^2P_{1/2}$ hyperfine constant, $A_{P_{1/2}}$, and characterize the effect of quantum interference in one of the measurements [6].

For both D_1 and D_2 measurements, each point is the average of 100 to 200 individual photon counting experiments. A single lineshape is a collection of 6 repetitions of 400 points across the laser detuning range of about $\pm$ 80 MHz. The order of measurement points is randomized for each set. The final results are then assembled from uncertainty-weighted averages of the individual measurements.

3.3 Measurement Lineshapes

The lifetime of the ^2P excited state in $^9Be^+$ was measured in 1969 by Andersen *et al.* to be $\tau = 8.1$ ns [20], corresponding to a natural linewidth of $\Gamma/2\pi \approx 19.6$ MHz. We later measured this as well, discussed in chapter 5, with a result closer to $\tau = 8.85$ ns or $\Gamma/2\pi \approx 18$ MHz. This result is in better agreement with theory [21]. Power broadening from a laser with saturation intensity of ≈ 0.02 contributes ≈ 200 kHz to the observed linewidth.

The measured ion temperature after Doppler cooling is ≈ 0.5 mK, which corresponds to a classical Doppler width,

$$\sqrt{\frac{8k_BTln(2)}{mc^2}}f_0 \approx 5 \text{ MHz}, \tag{3.1}$$

using values of m(^{9}Be)=1.496×10^{-26} kg, k_B=1.38×10^{-23} J/K, f_0=957×10^6 MHz. Representative experimental D_1 and D_2 data with fits and studentized residuals are shown in Figure 3.2. The photon recoil shift and slight asymmetry from heating were characterized carefully and are discussed in a separate section. D_1 measurements are slightly broadened compared to D_2 measurements from repump saturation broadening, related to the amount of population depletion from the initial state.

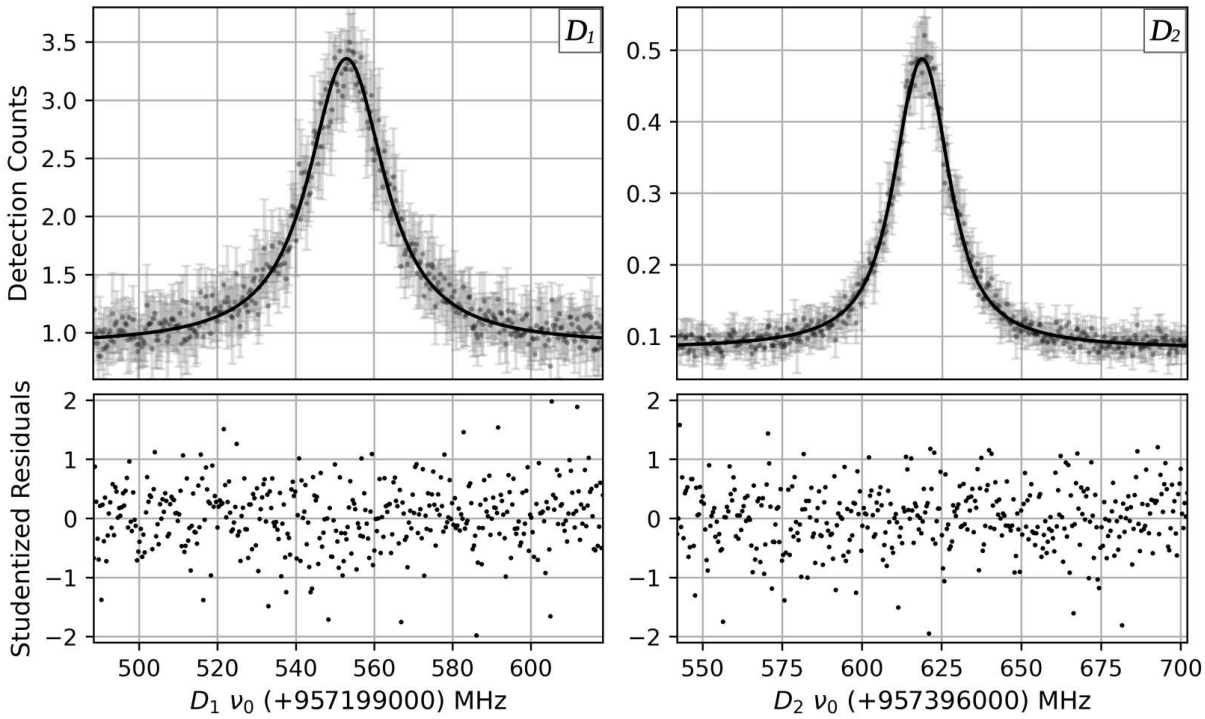

Figure 3.2: Lineshapes from individual D_1 (left) and D_2 (right) measurements are shown with Voigt fits and residuals. The D_1 measurement is from the set of σ^- re-pump measurements from $|^2S_{1/2}, 1, -1\rangle$ to $|^2P_{1/2}, 2, -2\rangle$. The D_2 measurement is on the σ^- closed cycling transition from $|^2S_{1/2}, 2, -2\rangle$ to $|^2P_{3/2}, 3, -3\rangle$.

3.4 Uncertainty Budget Summary

In total, 37 D_2 measurements and 95 D_1 measurements were collected and used in the final analysis. The overall statistical uncertainties for both D-line measurements were evaluated by calculating the weighted standard error of the individual D_1 and D_2 measurements. Several systematic uncertainties have been investigated and those common to both D_1 and D_2 measurements are summarized in Table 3.1 and discussed individually in following sections.

Table 3.1: Statistical and systematic uncertainties for the D_1 and D_2 transitions (kHz). This list excludes the contribution of quantum interference, which is present in one of the D_1 measurement configurations (see text).

Effect	D_1	D_2
Statistical variation	17	16
Spectroscopy laser lock to OFC	28	28
Optical power stabilization	25	25
Blue side heating & asymmetry	25	25
Hyperfine constants	3.8	13.8
Magnetic field drift	< 2	< 2
AC Stark shift (optical)	< 1	< 1
Imperfect laser polarization	< 1	< 0.1
Primary frequency reference	< 0.5	< 0.5
Total	**48**	**50**

3.5 Laser Frequency Stabilization to OFC

During these measurements, the spectroscopy laser was stabilized to an optical frequency comb (OFC). The OFC repetition rate and offset frequency were monitored throughout the measurement duration. The slow drift in the OFC repetition rate from thermal expansion of an ultra-stable cavity is at a negligible level for these measurements. Noise related to stabilization feedback of the laser to the OFC is the main source of broadening and uncertainty related to the beat note detection. To estimate the uncertainty and determine the center frequency, the beat note was observed both on a frequency counter and as a time averaged

spectrum on an externally referenced RF spectrum analyzer. Uncertainty in the center frequency determination in the IR is estimated at ±7 kHz, which corresponds to ±28 kHz in the UV. A sample beat note spectrum is shown for reference in Figure 3.3.

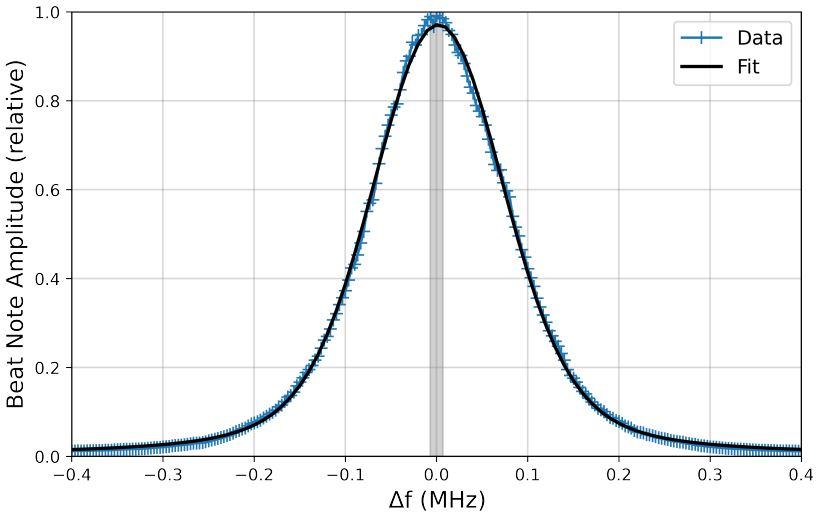

Figure 3.3: A typical time averaged RF spectrum generated from the optical beat note between the optical frequency comb and stabilized laser. Data is shown in blue with a Voigt fit in black. The estimated uncertainty in the center frequency determination is shown as a grey band.

3.6 Optical Power Stabilization for D-line Measurements

Stabilization of the laser power and spatial profile as a function of the AOM drive frequency is critical to achieve an uncertainty lower than a few hundred kHz in the strong transition measurements. The spatial profile was stabilized by spatial filtering in 6 inch length patch cables of UV single mode fiber (Thorlabs SM300). Optical power stabilization was achieved through feedback on the AOM drive amplitude. Two identical spatial filters and optical power feedback sections were implemented, one for the D_2 lasers and one for the D_1 lasers. These were optimized independently.

To apply the feedback, a small portion of the beam ($\approx 20\%$) after the spatial filter was sampled with an amplified photodiode detector (Thorlabs PDA25K2). The detector output

voltage was read in by ARTIQ and used to adjust the drive amplitude on the AD9910 DDS channel driving the AOM. A sample-and-hold routine was applied, with the optical power corrected prior to taking data at each new frequency setpoint. Only proportional gain was implemented in this experiment. The sampling routine would loop a discrete number of times, typically about 15, after which the AOM drive amplitude to apply for the new frequency setpoint was determined. Photodiode readings at the final AOM drive amplitude setpoint were recorded to monitor the effectiveness of the stabilization. A high speed shutter (SRS SR475) was also added to block incident beams on the detector when the stabilization routine was not running.

A plot of the typical achieved optical power stabilization is shown in Figure 2.21. Feedback parameters were optimized to ensure any residual slope to the optical power as a function of frequency was less than 3% across the full scan range. The total residual systematic uncertainty related to optical power stabilization in the D-line center frequency determinations is $\leq$25 kHz.

3.7 Photon Recoil Heating and Motional Sideband Asymmetry

Measurements are performed in an intermediate confinement regime with secular motional frequencies ($\omega_z/2\pi \approx 3.65$ MHz, $\omega_x/2\pi \approx 9.8$ MHz, $\omega_y/2\pi \approx 10.6$ MHz) much greater than the photon recoil frequencies for each axis ($\omega_{rec}/2\pi = 226\ \text{kHz} \times \cos^2\theta_{x,y,z}$), but less than the natural linewidth of the transition ($\Gamma/2\pi = 18$ MHz). The angles between laser propagation direction and trap axes are $\theta_z = 45°$ (axial), $\theta_{x,y} = 60°$ (radial). The Lamb-Dicke parameters are defined as $\eta = (\omega_{rec}/\omega_{x,y,z})^{1/2}$, for each axis [31], $\eta_x, \eta_y, \eta_z \approx 0.076$, 0.073, 0.176.

In the reference frame of the ion, the laser appears phase modulated with sidebands at the secular frequencies [46]. Matrix elements $\langle n'| e^{i\eta(a+a^\dagger)} |n\rangle$ scale the carrier ($\Delta n = 0$) and sideband ($\Delta n = \pm 1$) amplitudes, in place of the classical J_n Bessel functions. Laguerre polynomial based expressions for the matrix elements in the one dimensional case are given

in [31] and a plot of the squared matrix elements is shown on the left side of Figure 3.4. The basis of the heating and spectrum model is to calculate the full phase modulated spectrum of the laser in the reference frame of the ion and apply it to the Lorentzian lineshape of the transition. Since there is projection of each axis onto the laser, each secular mode contributes to the spectrum in this experimental configuration. The phase modulation terms can be applied somewhat independently, so long as the frequencies are non-degenerate. The laser spectrum is the Fourier transform of the carrier (ω_c) with phase modulations at three different frequencies ($\omega_1, \omega_2, \omega_3$),

$$E(t) \propto \cos\left(\omega_c t + a_1 \cos\left(w_1 t\right) + a_2 \cos\left(w_2 t\right) + a_3 \cos\left(w_3 t\right)\right). \tag{3.2}$$

In classical sinusoidal modulation, the spectrum is comprised of terms which are products of Bessel functions scaling the various sideband components,

$$I(\omega) \propto \sum_{n,m,l} J_n^2(a_1) J_m^2(a_2) J_l^2(a_3) \delta(\omega - \omega_c + n\omega_1 + m\omega_2 + l\omega_3) \tag{3.3}$$

where $n, m, l \in [0, \pm 1, \pm 2, \pm 3, ...]$. In the quantized model, the Bessel functions are replaced with the squared matrix elements which correctly represent the sideband asymmetry at low average mode occupation number, $\bar{n}$. An example is shown on the right side of Figure 3.4. Typically only the lowest few orders for each index are necessary to consider, due to the scaling in orders of η^2. The final model included calculations to 6^{th} order in the axial mode and 4^{th} order in the radial mode frequencies.

Since the matrix elements are defined for the integer n (Fock) states, it is necessary to sum over a thermal probability distribution described by $\bar{n}$ for each mode. This value at all points in time and detuning is a necessary input to the model to determine the relative sideband amplitudes. Note that a thermal distribution is not only a reasonable assumption, it was also shown experimentally to be the correct distribution after Doppler cooling of $^9Be^+$ ions in [48]. Generation of non-classical motional states required first ground state

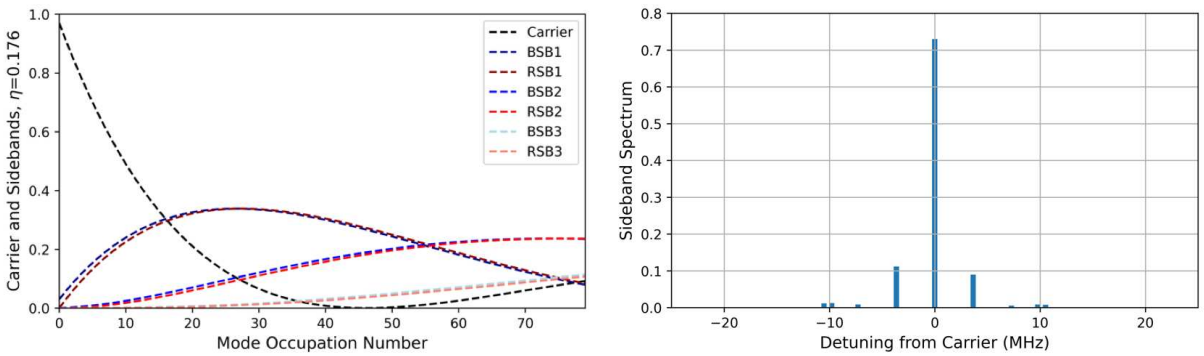

Figure 3.4: A plot of the squared matrix elements for a Lamb-Dicke parameter of $\eta_z = 0.176$ is shown (left). These are analogous to Bessel functions $|J_{\Delta n}(2\eta\sqrt{n})|^2$ which give the sideband amplitudes in classical phase modulation [47], but now with quantization and the appropriate asymmetry in the red and blue components. A sample laser spectrum in the reference frame of the ion is shown (right). The plot is for arbitrarily selected mode occupation numbers 4, 2 and 2 for the axial and two radial modes. Note that the blue sidebands appear on the low frequency side in the ion reference frame such that they generate a peak in the excitation spectrum for a detuning of $\omega_0 + \omega_{bsb}$, consistent with the convention in [46].

cooling then specific adjustment of motional state populations. Heating can be modeled with experimental parameters using the descriptions in [31,46]. We have measured $\bar{n}$ for each mode as a function of both D_2 pulse time and detuning using Raman sideband spectroscopy. The heating results are shown in Figure 3.5, with corresponding modeled spectral components in Figure 3.6. Limiting the number of scattering events to prevent excessive heating during the spectroscopy pulses is important, however, under the experimental conditions in this work, the spectral shifts primarily come from the asymmetry in the red and blue sidebands in both the D_1 and the D_2 measurements. The overall effect is a scaled photon recoil shift, which tends toward the full free-particle photon recoil in the weak confinement limit and zero in the strong confinement limit.

As a further check on the consistency of the model at low $\bar{n}$, the center frequency for the D_2 transition was measured at a variety of total exposure levels and compared with expectations from the model. Average mode occupation number inputs to the model for the various exposure levels were scaled linearly, a reasonable approximation in this regime. The total number of scattering events was calibrated based on the total detection efficiency

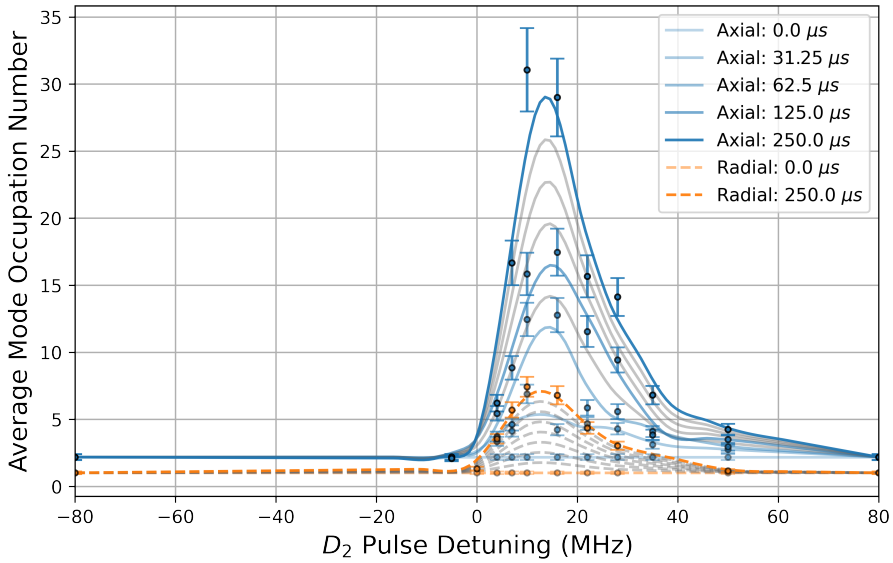

Figure 3.5: Average mode occupation number measurements as a function of both time and D_2 pulse detuning are plotted with approximate error bars for the axial mode (blue solid) and one of the radial modes (orange dashed). The mode occupation is similar for the second radial mode. Lines represent a smooth interpolation over a total of nine discrete time steps.

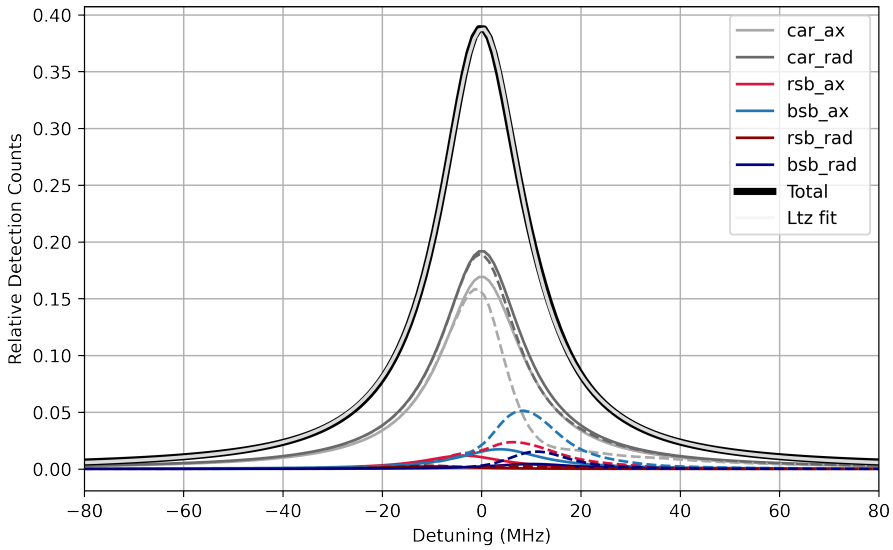

Figure 3.6: Plot of the calculated excitation spectrum during a D_2 spectroscopy pulse, at 0 μs (solid) and 250 μs (dashed). The sideband composition changes some as the ion heats, though the change in the total spectrum is mild for small amounts of heating. The effect presents as a photon recoil shift that is slightly less than the free particle recoil shift, due to the finite confinement. This effective shift goes to zero in the limit of very strong confinement, when the secular motional sidebands are fully resolved from the lineshape [49,50], analogous to the Mössbauer effect in crystals.

(≈ 0.27 %), which includes collection geometry, optical losses, σ dipole radiation pattern and PMT quantum efficiency. The results are shown in Figure 3.7.

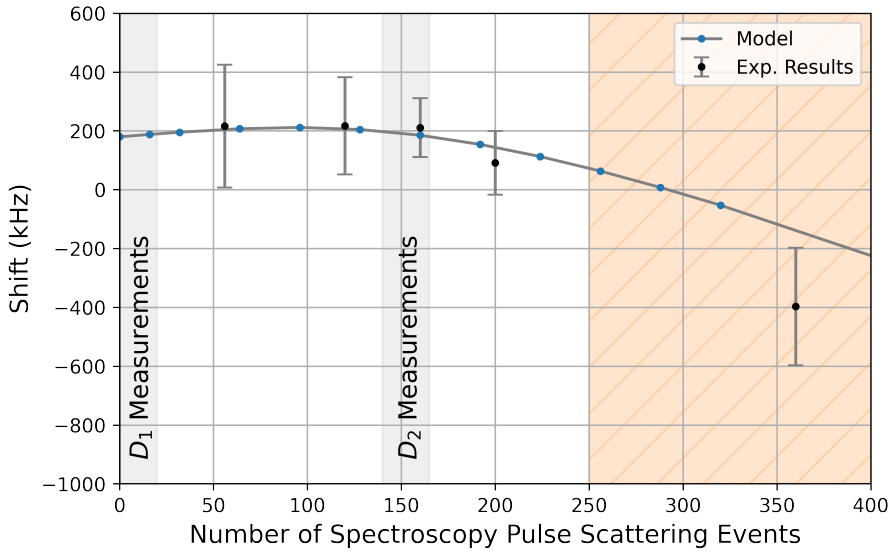

Figure 3.7: Experimental results for several D_2 spectroscopy pulse exposure levels are shown in comparison to predicted shifts based on the model. The absolute offset for the experimental data points is set manually, as only a relative shift can be determined experimentally. Grey bands represent the approximate regions in which D_1 and D_2 measurements take place. In these regions the recoil shift is reasonably flat. The orange hatch represents the region in which the heating starts to become excessive with distortion more visually apparent in the lineshape.

3.8 Quantum Interference

Quantum interference can also play a role in the observed spectral lineshape. Transition rates between specific initial and final ground states are calculated using simplified expressions derived from [6]. An equivalent description is provided in [51]. As a brief summary, the starting point for this calculation is the Kramers-Heisenberg formula, which gives the differential scattering rate into solid angle $d\Omega_s$,

$$\frac{dR_{i\to f}}{d\Omega_s} = \frac{2\pi}{\hbar}|M_{fi}|^2\rho_s, \tag{3.4}$$

where i and f represent the initial and final ground states and ρ_s is the scattered photon state density. M_{fi} are scattering matrix elements which depend on frequency and polarization.

The scattering matrix elements are expanded to a product of dipole matrix elements, then simplified with the Wigner-Eckart theorem to arrive at:

$$\frac{dR_{i\to f}}{d\Omega_s} = \frac{3}{8\pi}\frac{I}{I_0}\left(\frac{\Gamma}{2}\right)^3 \left| \sum_{F'm'} \frac{(\hat{\epsilon}_s \cdot A^{F'm'}_{F_f m_f})(A^{F'm'}_{F_i m_i} \cdot \hat{\epsilon}_L)}{\Delta^{F'}_{F_i} + i\Gamma/2} \right|^2, \tag{3.5}$$

with a defined reference intensity I_0, natural linewidth Γ, applied laser and scattered polarizations $\hat{\epsilon}_L$ and $\hat{\epsilon}_s$, laser detuning $\Delta^{F'}_{F_i}$, and intermediate excited state quantum numbers F' and m'. Full expressions for the $A^{F'm'}_{Fm}$ terms, written in the A_q spherical vector basis are given in the appendix of [6], and a brief description of how these terms arise by reduction of the full dipole matrix elements is given in the next section.

In our D_1 measurements, the laser polarization is set to be either σ^-, σ^+ or π, which simplifies the dot product involving $\hat{\epsilon}_L$. Another simplification is the population has been coherently transferred to a single initial ground state sublevel, rather than a statistical distribution of sublevels [6]. Under these two conditions, the sum over m' is trivial since there can be only one intermediate m' value. Expressions for the scattering direction $\hat{k}_s$, and two orthogonal polarizations $\hat{\epsilon}_{s_1}$ and $\hat{\epsilon}_{s_2}$ can be written as $\hat{\epsilon}_r$, $\hat{\epsilon}_\theta$ and $\hat{\epsilon}_\phi$, respectively,

$$\hat{k}_s = \sin\theta\cos\phi\hat{x} + \sin\theta\sin\phi\hat{y} + \cos\theta\hat{z}, \tag{3.6}$$

$$\hat{\epsilon}_{s_1} = \cos\theta\cos\phi\hat{x} + \cos\theta\sin\phi\hat{y} - \sin\theta\hat{z}, \tag{3.7}$$

$$\hat{\epsilon}_{s_2} = -\sin\phi\hat{x} + \cos\phi\hat{y}. \tag{3.8}$$

Transformation into the $[\sigma^+, \pi, \sigma^-]$ basis, using standard definitions such as Eq. 4.110 in [52] yields:

$$\hat{k}_s = \begin{bmatrix} \frac{-\sin\theta}{\sqrt{2}}(\cos\phi - i\sin\phi) \\ \cos\theta \\ \frac{\sin\theta}{\sqrt{2}}(\cos\phi + i\sin\phi) \end{bmatrix} \tag{3.9}$$

$$\hat{\epsilon}_{s_1} = \begin{bmatrix} \frac{-\cos\theta}{\sqrt{2}}(\cos\phi - i\sin\phi) \\ -\sin\theta \\ \frac{\cos\theta}{\sqrt{2}}(\cos\phi + i\sin\phi) \end{bmatrix} \tag{3.10}$$

$$\hat{\epsilon}_{s_2} = \begin{bmatrix} \frac{i}{\sqrt{2}}(\cos\phi - i\sin\phi) \\ 0 \\ \frac{i}{\sqrt{2}}(\cos\phi + i\sin\phi) \end{bmatrix}. \tag{3.11}$$

In our case, we do not collect photons during the D_1 spectroscopy pulse. Therefore, the total scattering rate, regardless of emission direction or polarization, is the relevant quantity. A sum of the two independent scattered polarizations and integration over full solid angle gives $\frac{8\pi}{3}$ for each spherical vector component. A simplified expression results in the total rate for each set of initial and final states

$$R_{i\to f} = \frac{I}{I_0}\left(\frac{\Gamma}{2}\right)^3 \left| \sum_{F'} \frac{(A^{F'm'}_{F_f m_f})_{q_s}(A^{F'm'}_{F_i m_i})_{q_L}}{\Delta^{F'}_{F_i} + i\Gamma/2} \right|^2. \tag{3.12}$$

Sums over q_s and m' have been suppressed due to control of the laser polarization and preparation of a single initial state. An expression similar to Eq. 4 in [6] can be defined for the numerator,

$$C^{F'}_{i\to f}(q_s, q_L) = (A^{F'm'}_{F_f m_f})_{q_s}(A^{F'm'}_{F_i m_i})_{q_L}. \tag{3.13}$$

If desired, the complex square magnitude can be evaluated to give an expression that contains the sum of individual Lorentzian contributions and interference cross terms. Note that all $C^{F'}_{i\to f}(q_s, q_L)$ terms are real so there is no need to carry complex conjugate notation. This

expression is given as

$$R_{i\to f} = \frac{I}{I_0}\left(\frac{\Gamma}{2}\right)^3 \left[\sum_{F'} \frac{\left(C^{F'}_{i\to f}(q_s,q_L)\right)^2}{(\Delta^{F'}_{F_i})^2 + (\frac{\Gamma}{2})^2} + \sum_{F'\neq F''} \frac{2C^{F'}_{i\to f}(q_s,q_L)C^{F''}_{i\to f}(q_s,q_L)\left(\Delta^{F'}_{F_i}\Delta^{F''}_{F_i} + (\frac{\Gamma}{2})^2\right)}{\left((\Delta^{F'}_{F_i})^2 + (\frac{\Gamma}{2})^2\right)\left((\Delta^{F''}_{F_i})^2 + (\frac{\Gamma}{2})^2\right)}\right].$$

Each individual equation describes the total scattering rate when starting in state $|i\rangle$ and ending in state $|f\rangle$. The sum over F' represents the interfering amplitudes from the multiple intermediate exited states. Rates for different combinations of initial and final state are calculated separately in an identical manner. Note that it is assumed the energy levels are non-degenerate and separated far enough that temporal effects like quantum beats are fast relative to measurement timescales.

Rates are assembled into a set of differential equations and solved as a function of measurement pulse duration to give the final state populations. In simple cases, analytical solutions can be found. The final populations are scaled by the experimentally determined bright level of each ground state during a D_2 state detection pulse, and summed to give an expected photon count at each frequency point. This full lineshape is used to fit the data involving quantum interference and extract the center frequency. An example is shown in Figure 3.8.

The additional systematic uncertainty associated with the quantum interference correction in this measurement was $\approx \pm 50$ kHz. This is limited by how precisely the spectroscopy pulse duration and intensity variables in the model can be matched to experimental conditions. While it is still ideal to probe transitions which have only a single intermediate excited state or are sufficiently resolved from other states that the interference distortions are negligible, it is not always possible or convenient. In this experiment the separate π transition measurement from $|^2S_{1/2}, 2, 0\rangle$ to $|^2P_{1/2}, 1, 0\rangle$ did not contain quantum interference, which was a useful benchmark for comparison.

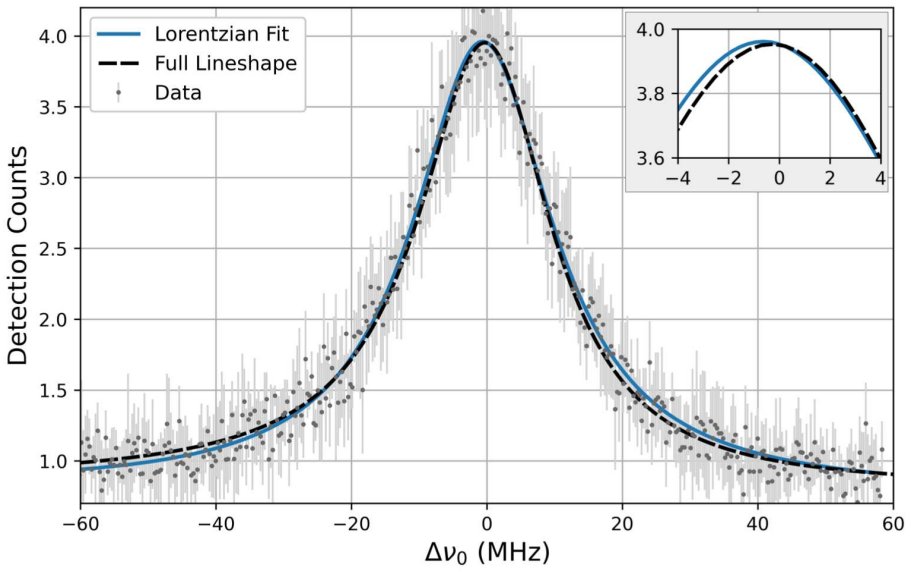

Figure 3.8: Two component Lorentzian and quantum interference corrected lineshape fits are shown for a single $|^2S_{1/2}, 1, 0\rangle$ to $|^2P_{1/2}, 1, -1\rangle$ data set. A magnified section is shown in the upper-right cutout. Extracted center frequencies using Lorentzian fits are consistently low by ≈ 630 kHz in this particular measurement. Quantum interference calculations capture the full lineshape and can directly extract the correct absolute transition frequency.

3.9 Wigner-Eckart Theorem Reduction of Dipole Matrix Elements

The numerator of each individual quantum interference term in the previous section contains the product of two terms, $(A^{F'm'}_{F_i m_i})_{q_L}$ and $(A^{F'm'}_{F_f m_f})_{q_s}$, which are the relative amplitudes associated with the excitation from state $|F_i, m_i\rangle$ to excited state $|F', m'\rangle$ with polarization q_L and decay to state $|F_f, m_f\rangle$ with polarization q_s. These terms originate from full dipole matrix elements, for example $\langle J', F', m'||D||J, F, m\rangle$, where D is the dipole operator. The discussion here follows the appendix of [6], and is generally consistent with chapter 7 of [53] (up to factors of $\sqrt{2J+1}$ or $\sqrt{2J'+1}$ being included or not in $\langle J'||D||J\rangle$). Since the hyperfine and Zeeman structures are small perturbations to the fine structure and do not appreciably change the electronic wavefunctions, their effects can be factored out from the full dipole matrix element to leave a reduced matrix element $\langle J'||D||J\rangle$. The reduced matrix element is proportional to the natural linewidth, Γ, and is common to all transitions within a given fine-structure manifold.

The starting point is the full dipole matrix element connecting each ground and excited state via the dipole interaction of an electric field of polarization q,

$$\langle J', F', m'||D_q||J, F, m\rangle\,. \tag{3.14}$$

Application of the Wigner-Eckart theorem extracts the m, m' and polarization dependence, yielding a reduced matrix element multiplied by a Clebsch-Gordan coefficient and a scaling factor.

$$\langle J', F', m'|D_q|J, F, m\rangle = \langle J', F'||D||J, F\rangle\,\frac{\langle F, m, 1, q|F', m'\rangle}{\sqrt{2F'+1}}. \tag{3.15}$$

The F and F' dependence can then be factored out as a Wigner-6j term, along with additional scaling factors,

$$\langle J', F'||D||J, F\rangle = \langle J'||D||J\rangle\,(-1)^{F+I+1+J'}\sqrt{2F+1}\sqrt{2F'+1}\begin{Bmatrix} J' & J & 1 \\ F & F' & I\end{Bmatrix}. \tag{3.16}$$

The reduced matrix elements can be expressed in terms of the natural linewidth,

$$\Gamma = \frac{\omega_0^3}{3\pi\epsilon_0\hbar c^3}\frac{|\,\langle J'||D||J\rangle\,|^2}{2J'+1}. \tag{3.17}$$

The $(A_{Fm}^{F'm'})_q$ terms are defined to contain all the factored-out dependence on polarization and F and m angular momentum quantum numbers. The remaining $\langle J'||D||J\rangle$ reduced elements are expressed in terms of Γ, which is common to all transitions within a given fine structure manifold.

3.10 Polarization Purity of the Spectroscopy Laser

Prior to each set of measurements, the laser polarization is carefully adjusted to the required state. An α-BBO Glan-Laser polarizer is first used to ensure a clean linear polar-

ization state from the UV doubler (extinction ratio $< 5 \times 10^{-6}$), after which the quarter and half waveplates are adjusted to set the desired state. Half-waveplates are held in rotation mounts, and the quarter waveplates are held in tip/tilt mounts for fine tuning of the birefringence. The magnetic field coil currents can also be adjusted to null the off-axis fields or optimize the k vector alignment.

The D_2 σ^- polarization can be set precisely using feedback from optical pumping and is discussed later on. The D_1 σ^- polarization traverses the apparatus in the opposite direction and can be optimized by minimization of the counter-propagating beam through the D_2 side polarizer or by optimization on a D_1 σ^- transition. The π polarization is more difficult to ensure high purity, as there isn't as strong a feedback signal for optimization. The beam geometry, however, ensures polarization impurities are split symmetrically between σ^- and σ^+ components, which doesn't tend to cause significant line pulling. Note that the beam geometry also strongly suppresses the possibility for π polarization impurity on σ measurements.

Several tests were completed to check for consistency and to observe potential shifts related to polarization. For σ^- measurements, equivalent σ^+ measurements were performed at various times throughout the measurement campaign. The reason for this test is polarization impurity tends to pull in opposite directions for the two cases. No significant disagreement was found in any case. For the D_1 π measurement, the linear polarization was intentionally rotated to introduce σ^- and σ^+ polarization impurity. This also did not produce a shift in the measured line center, as expected based on the level structure and geometry.

Approximate shifts in the D_1 frequency due to a 1% impurity in laser polarizaztion are summarized in Table 3.2. Adjusted lineshapes were generated based on rate equations from the quantum interference section. The D_1 measurements are not particularly sensitive to polarization impurity, as the hyperfine splitting is about 12 linewidths (too large for a small impurity component to generate a large shift) and the Zeeman splitting is only 200 kHz (too small to generate large shifts).

Table 3.2: Estimated D_1 shifts in kHz from π and σ polarization impurities, per 1%. For clarity, on a σ^- measurement a σ impurity means σ^+. On the π measurement it means equal split of σ^+ and σ^-. Note that the beam geometry strongly suppresses π polarization impurity on σ measurements.

Measurement	π	σ
D_1 σ^- $\|1,-1\rangle$ to $\|2,-2\rangle$	0.2	0.6
D_1 σ^- $\|1,0\rangle$ to $\|1,-1\rangle$	<0.1	0.4
D_1 π $\|2,0\rangle$ to $\|1,0\rangle$	$\cdots$	0.2

The D_2 measurement is potentially more sensitive to polarization impurity for two reasons. The first is the hyperfine and Zeeman splitting of the $^2P_{3/2}$ levels is on the order of 1-5 MHz, in the general range that can produce line pulling for the ≈18 MHz natural linewidth transition. The second is since more photons are scattered in a D_2 measurement pulse (peak ≈ 160), some amount of optical pumping could occur as a function of laser detuning. Fortunately, optical pumping also provides strong feedback for precise optimization of the σ^- polarization. Furthermore, with high extinction ratio the probability of pumping into dark states from the limited number of scatter events during detection becomes negligible.

The peak count rate is first optimized with the laser tuned to resonance on the $|^2S_{1/2}, 2, -2\rangle \rightarrow |^2P_{3/2}, 3, -3\rangle$ cycling transition. Since the Doppler cooling and detection beams are derived from the same laser and are co-aligned through the same optical fiber and polarization optics, they share the same polarization. All available adjustments are tuned repeatedly in a sequential manner and typically a high degree of pumping is achieved into $|^2S_{1/2}, 2, -2\rangle$. Histograms are recorded, binned according to number of photon counts detected and summed over the 100 to 200 repetitions. A typical example is shown in Figure 3.9.

Excess probability contained in the histogram dark bins compared to the main Poisson distribution is proportional to population leakage, mainly to $|^2S_{1/2}, 1, -1\rangle$, which occurs due to slight σ^+ polarization impurity. Some leakage to $|^2S_{1/2}, 1, 0\rangle$ would also be expected, but the specific route is mostly suppressed by quantum interference. A typical population ratio achieved is 98.6% with the laser on resonance. The measured population ratio can be used with relative scattering probabilities to estimate the σ^+/σ^- polarization extinction ratio.

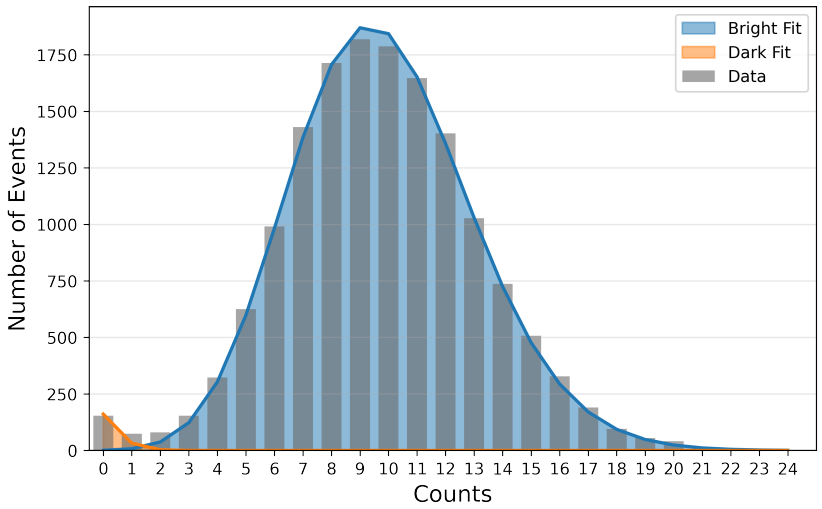

Figure 3.9: Histogram of a collection of data taken on D_2 resonance under typical polarization conditions. The $|^2S_{1/2}, 2, -2\rangle$ population is proportional to the number of events contained within the main Poisson distribution, while the population in dark states (mainly $|^2S_{1/2}, 1, -1\rangle$) is proportional to excess events in the dark bins. The distribution suggests population of 98.6% with the D_2 detection beam on resonance.

The estimated ratio based on a rate equation model is of the same order as the polarizer at 10^{-6}. At this level, pumping effects during a typical D_2 detection cycle and spectral line pulling are both negligible. Furthermore, any polarization impurity tends to appear in the histogram signal before reaching a level that leads to significant systematic shifts.

3.11 Results and Discussion

A summary of the individual D_1 and D_2 frequency measurements is shown in Figure 3.10. Final results for the absolute frequecies of the D-lines, $\Delta\nu_{fs}$, and $A_{P_{1/2}}$ are summarized in Figure 3.11 and Table 3.3. These results are compared to previous measurements and theory.

The measured D_1 and D_2 frequencies are in good agreement with a recent collinear spectroscopy measurement with uncertainties that have been reduced by a factor of 10 and 30, respectively [15]. This work helps to resolve a previous 7σ (combined) discrepancy in the D_2 frequency which was observed between recent trap-based and online measurements [14, 15]. The major source of systematic uncertainty in the online measurement is the cancellation of

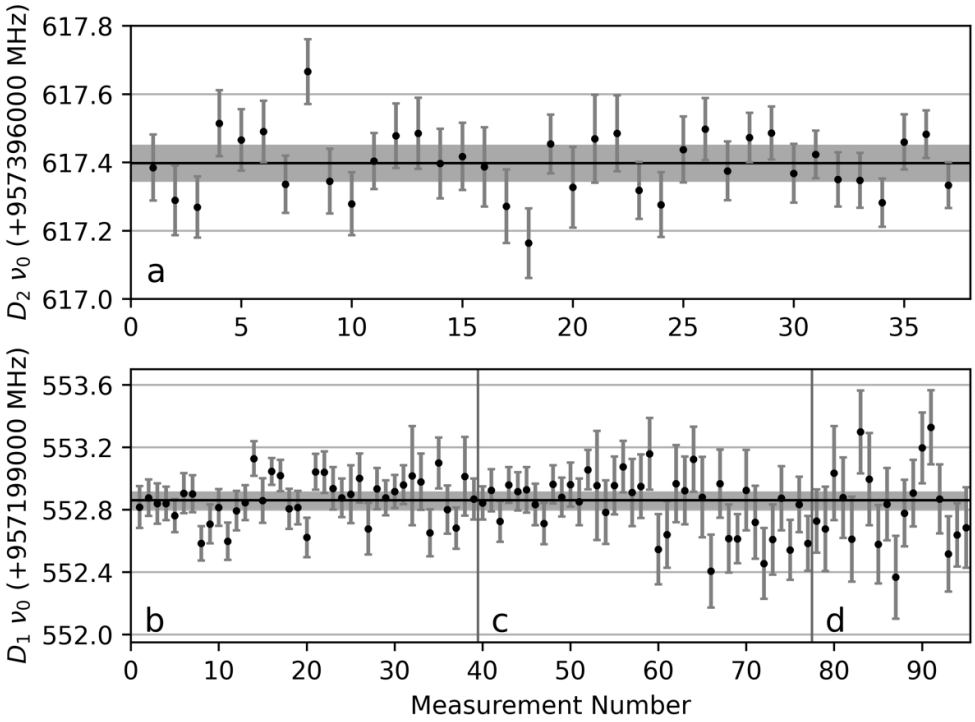

Figure 3.10: Individual measurements of the D_1 and D_2 frequencies. Labels a through d correspond to configurations in Figure 3.1. Error bars on each point represent statistical uncertainties in the individual fits. The weighted mean is shown as a solid black line, with total statistical and systematic uncertainties, summed in quadrature, shown as a grey band. The reduced χ^2 for D_1 and D_2 measurements are 1.06 and 1.10, respectively.

Table 3.3: Absolute transition frequencies of the $^9Be^+$ D-lines, ^2P fine structure interval, $\Delta\nu_{fs}$, and $^2P_{1/2}$ hyperfine constant, $A_{P_{1/2}}$ in units of MHz. Previous experimental results and theoretical values are compared with this work.

D_1	D_2	$\Delta\nu_{fs}$	$A_{P_{1/2}}$	Ref.
957 199 652(120)	957 396 802(135)	···	-118.6(36)	Exp[a]
···	957 396 515(14)	···	···	Exp[b]
957 199 553.28(52)[d]	957 396 616.6(15)[d]	197 063.2(16)[d]	-118.00(4)[c]	Exp[c,d]
···	···	197 068.0(25)[d]	-117.932(3)[e]	Theory[d,e]
957 199 552.86(5)	957 396 617.40(5)	197 064.54(7)	-117.92(4)	This Work

[a]Bollinger, et. al, (1985) [13] [b]Nakamura et. al., (2006) [14] [c]Nörtershäuser et. al., (2009) [7]
[d]Nörtershäuser et. al., (2015) [15] [e]M. Puchalski, K. Pachucki, (2009) [3]

the first order Doppler shift associated with the collinear spectroscopy method [54]. In the work presented here, both first- and second-order Doppler shifts are negligible at the current level of precision. A specific advantage of the trap-based D_2 measurement configuration in this work is that it probes only the $|^2P_{3/2}, F = 3\rangle$ state. One possible complication with the

online measurements may be the simultaneous fitting of multiple unresolved hyperfine components, where the hyperfine constants and relative intensities of the multiple components were left as free fitting parameters [55].

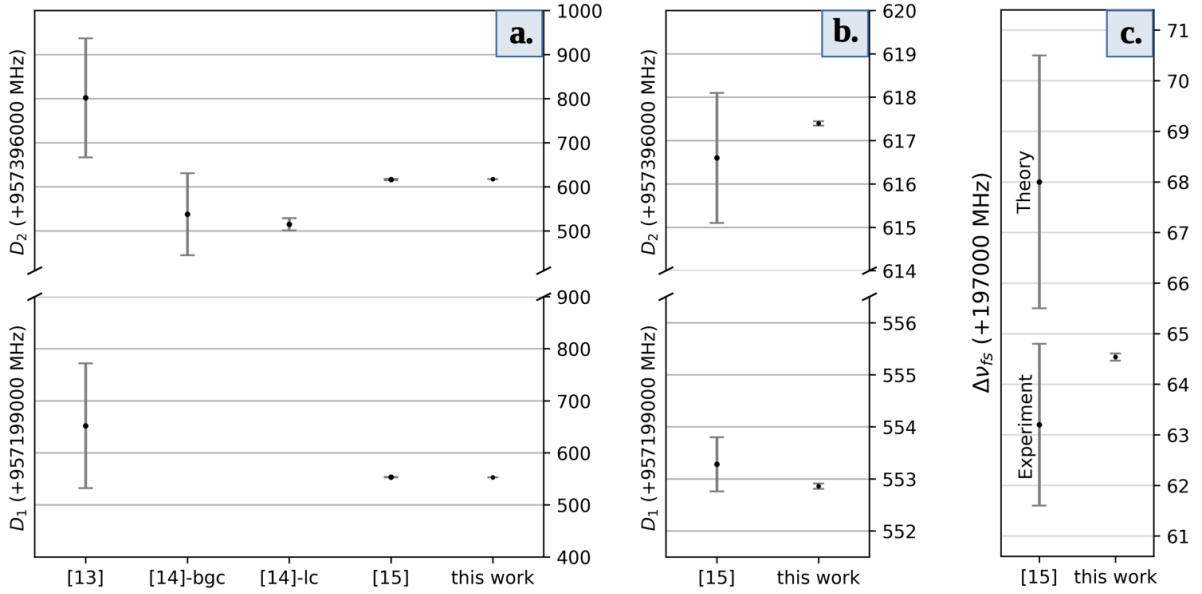

Figure 3.11: (a.) A comparison with previous D_1 and D_2 measurement results. Starting from the left are the NIST Penning trap measurements [13], the RIKEN buffer-gas-cooled and laser-cooled rf quadrupole trap measurements [14] and the ISOLDE collinear laser spectroscopy measurements [15]. (b.) A zoomed in comparison with the ISOLDE results [15]. (c.) The extracted fine structure splitting in comparison to both the experimental and theoretical values from [15].

A slight tension of 1.4σ (combined) is seen between the ^2P fine structure splitting reported here, $\Delta\nu_{fs}$, and the most recent theoretical calculations [3]. The uncertainty in the measurement is approximately 23 times smaller than the estimated theoretical uncertainty, suggesting that more theoretical work is needed to reduce that uncertainty and allow for a stringent test of the many-body QED theory in $^9Be^+$ [3,15]. In addition, the measured $^2P_{1/2}$ hyperfine constant, $A_{P_{1/2}}$, is consistent with recent theory [3]. In this case, the uncertainty in the comparison between theory and experiment is dominated by the experiment. Improvements in frequency metrology infrastructure and control of systematics could lead to reduced uncertainties. For example, it would be possible to repeat this set of measurements using

an auxiliary ion for sympathetic cooling [56, 57] and quantum-enabled state readout such as Mg^+ or Ca^+, as is done in high-accuracy optical clocks and photon recoil spectroscopy experiments [27,58,59]. The addition of a sympathetic cooling ion would eliminate the effect of motional heating due to photon scattering during the spectroscopy pulse and would allow for individual measurements which have a higher signal-to-noise ratio than could be achieved in this work.

Chapter 4

$^9Be^+$ 2p $^2P_{3/2}$ Unresolved Hyperfine Splittings

4.1 Motivation

In order to achieve the highest accuracy possible in our measurements of the absolute frequencies of the $^9Be^+$ D lines, we relied on theoretical values for the $^2P_{1/2}$ hyperfine A (magnetic dipole) coefficient and the $^2P_{3/2}$ hyperfine A and B (electric quadrupole) coefficients to determine the final center-of-gravity of the D_1 and D_2 transitions [3,22]. Since each D line measurement is made between a specific initial $|F, m_F\rangle$ and final $|F', m'_F\rangle$ state, it was necessary to correct our measured frequencies for the hyperfine structure in the $^2S_{1/2}$, $^2P_{1/2}$, and $^2P_{3/2}$ states. As a consistency check on our D_2 measurements, we performed repump measurements on the $|^2S_{1/2}, F = 1, m_F = -1\rangle \rightarrow |^2P_{3/2}, F = 2, mF = -2\rangle$ transition. Initial measurements were not consistent with what we predicted based on the published $^2P_{3/2}$ hyperfine constants. After detailed consideration and discussion with theoretical colleagues K. Pachucki, M. Puchalski, and V. Yerokhin it was concluded the magnitude of the hyperfine coefficients were correct, but there was an incidental sign error on the published value for the electric quadrupole term. This sign error had gone unnoticed for several years likely due to the fact that the hyperfine splittings the $^2P_{3/2}$ state are much smaller than the natural linwidth of the D line transitions. In addition, Doppler cooling and detection of $^9Be^+$ for quantum-logic applications typically relies on addressing only the $|^2P_{3/2}, F = 3\rangle$ state.

After the initial measurement of the $|^2S_{1/2}, F = 1, m_F = -1\rangle \rightarrow |^2P_{3/2}, F = 2, m_F = -2\rangle$ transition, we began to consider if we could also measure to a third excited state F level and achieve the first direct measurements of at least two $^9Be^+$ $^2P_{3/2}$ hyperfine splittings and confirm the A and B coefficients from theory. The measurement to the $|^2P_{3/2}, F = 1\rangle$ state presented a surprising instance in which quantum interference simplified the measurement

procedure, rather than simply producing complicated lineshape distortion. These measurement results were published in early 2024 in Phys. Rev. A [60].

4.2 Introduction

While the nuclear magnetic dipole moment can be determined from the ground state hyperfine splitting in alkali-like systems, determination of higher order contributions requires probing higher angular momentum states [8]. For example, $^2P_{3/2}$ hyperfine structure measurements have been used previously to extract nuclear magnetic octupole moments in both ^{133}Cs [9, 10] and ^{87}Rb [11]. Interest in understanding such nuclear structure of light atoms has persisted over many decades, including recent theoretical work and a proposal to extend measurements to muonic Li^{2+}, Be^{3+} and B^{4+} [61].

$^9Be^+$ has been the focus of study in prior theoretical works [3, 22] and has been widely used in ion trap and ion beam experiments dating back several decades. It is a particularly convenient ion to Doppler cool, requiring only a single 313 nm laser tuned to the D_2 closed cycling transition. It also has a long-lived ground state hyperfine qubit due to its nuclear spin of $\frac{3}{2}$. Thus, $^9Be^+$ has served as an ion for sympathetic cooling and state readout in quantum logic-clocks [18, 19], as a qubit for quantum information processing [16, 17], and as a platform for precision measurement of a simple three electron atomic system [45]. While the $^2S_{1/2}$ and $^2P_{1/2}$ hyperfine splittings in $^9Be^+$ have previously been measured [7, 13, 24, 45], the $^2P_{3/2}$ hyperfine splitting of a few MHz remained difficult to observe directly, unresolved beneath the ≈18 MHz natural linewidth [20, 21].

A wide variety of methods have been developed for measurement of both resolved and unresolved hyperfine structure of alkali atoms [62], but for the $^2P_{3/2}$ structure of alkali-like $^9Be^+$, only rough bounds have been set experimentally using zero field quantum beat spectroscopy [23]. The method applied here utilizes quantum interference and state-selective repump spectroscopy techniques to enable direct optical measurements with high specificity to individual $|^2P_{3/2}, F, m_F\rangle$ states at low magnetic field. The spectroscopy is performed on

a single trapped ion, applying a framework developed for spectroscopy of strong transitions that accounts for photon recoil in an intermediate confinement regime [45]. Using a single ion also simplifies high fidelity initialization into a single $|^2S_{1/2}, F, m_F\rangle$ ground state and the exchange and preferential detection of final state populations throughout the $^2S_{1/2}$ manifold. With this approach, we have measured the frequency difference between three separate D_2 transitions to determine the hyperfine splittings between the $|^2P_{3/2}, F = 3\rangle$ and $|^2P_{3/2}, F = 2\rangle$ states ($\Delta\nu_{32}$), and the $|^2P_{3/2}, F = 3\rangle$ and $|^2P_{3/2}, F = 1\rangle$ states ($\Delta\nu_{31}$). The measurement configurations are summarized in Figure 4.1.

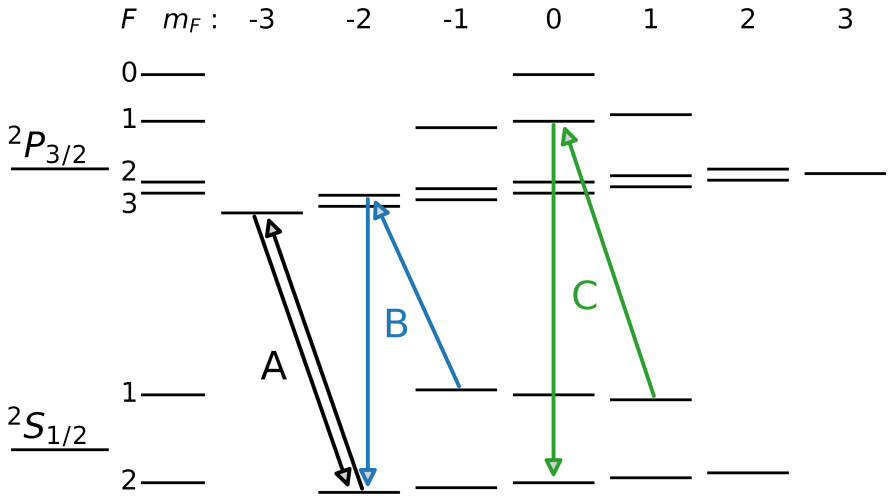

Figure 4.1: Energy level diagram for the $^2S_{1/2}$ and $^2P_{3/2}$ states in $^9Be^+$. The measurement configurations used to observe the hyperfine splittings are labeled as A, B and C. 'A' is the σ^- cycling transition, also used for Doppler cooling and state detection. 'B' is a standard repump configuration which scatters only through $|^2P_{3/2}, 2, -2\rangle$. 'C' is a configuration which preferentially detects scatter through $|^2P_{3/2}, 1, 0\rangle$ to $|^2S_{1/2}, 2, 0\rangle$. Splittings are recorded as difference frequencies, $\Delta\nu_{32} = \nu_B - \nu_A$ and $\Delta\nu_{31} = \nu_C - \nu_A$, after correction for the magnetic field contributions and $^2S_{1/2}$ hyperfine structure. Note that the 1-5 MHz $^2P_{3/2}$ hyperfine splittings are shown exaggerated in scale relative to the 1.25 GHz $^2S_{1/2}$ splitting.

4.3 Experiment

The ion trap and laser systems used in this work have been described in detail previously [45]. The linear rf Paul trap is a revised version of the wheel trap used in the aluminum ion quantum logic clock [27, 33], with gold electrodes on a diamond wafer and separate titanium endcaps spaced 4 mm from the center of the trap. A frequency stabilized UV laser at $\lambda = 313$ nm is used for Doppler cooling, optical pumping and state readout. The ion trap operates with an rf drive frequency of $\Omega_{rf}/2\pi = 78.93$ MHz and a differential drive amplitude of approximately $\pm$ 168 V. The secular mode frequencies of a single $^9Be^+$ ion are $\omega_z/2\pi \approx 3.65$ MHz for the axial mode, and $\omega_x/2\pi \approx 9.8$ MHz and $\omega_y/2\pi \approx 10.6$ MHz for the radial modes. A quantization axis magnetic field of $B = 13.43$ μT is used to produce ≈ 100 kHz separation between Zeeman sublevels. This low field value allows sufficient frequency separation between the states, while avoiding level crossings in the $^2P_{3/2}$ manifold that occur at higher field. The bias field is determined from measurements of the $|^2S_{1/2}, 2, -2\rangle \leftrightarrow |^2S_{1/2}, 1, -1\rangle$ transition ($\nu_{-2,-1} \approx 1250.3$ MHz). Stray magnetic fields on orthogonal axes are canceled using additional sets of magnetic field coils. A 50 mm diameter rf loop antenna is positioned just above the fluorescence collection window, outside the vacuum chamber above the trap. This is used to drive all microwave transitions between $|^2S_{1/2}, F, m_F\rangle$ states. The frequencies and pulses are generated by an externally referenced direct digital synthesizer. The fundamental rf frequencies are quadrupled to reach the required range of $\nu \approx 1250$ MHz. The microwave signal is amplified and then filtered to suppress other harmonic components.

All optical frequencies for this experiment are generated from a single laser. The laser frequency is stabilized to a wavemeter at a frequency that is detuned by ≈ -650 MHz from the $|^2S_{1/2}, 2, -2\rangle \rightarrow |^2P_{3/2}, 3, -3\rangle$ closed cycling transition. The laser frequencies are then adjusted using acousto-optic modulators (AOMs). The resonant detection beam is shifted up in frequency by ≈ 650 MHz and the repump beams are shifted down by ≈ 600 MHz to span the full 1.25 GHz ground state splitting. A cat-eye configuration is used for the double

pass AOM beams to suppress beam pointing variation [33]. The spatial profile is cleaned with a pinhole spatial filter and then power stabilized via feedback on the AOM drive power.

The excited state hyperfine splitting is determined as the sum of the AOM shifts for the cycling and repump transitions, minus the ground state contribution for each configuration. As absolute frequency measurements are not necessary, we determine only the relative splittings, $\Delta\nu_{32} = B - A$ and $\Delta\nu_{31} = C - A$ (see Figure 4.1), after correction for the magnetic field and $^2S_{1/2}$ hyperfine contributions. The frequency of the line center in (A) is determined by measurement before and after each repump measurement (B or C) with a linear interpolation using the time stamps of the scans. This is done to eliminate the effect of slow linear drift in the absolute frequency of the wavemeter lock point. The wavemeter tends to drift approximately 3 MHz over a single day, while a single set of measurements takes roughly 30 minutes. Drifts beyond the linear model are small, and negligible at the current measurement uncertainty.

At the start of each measurement, the ion is cooled using 1 ms of far-detuned ($\Delta/2\pi = -415$ MHz) laser cooling and 500 μs of near-detuned Doppler cooling ($\Delta/2\pi = -10$ MHz) on the $|^2S_{1/2}, 2, -2\rangle \rightarrow |^2P_{3/2}, 3, -3\rangle$ cycling transition ($\Gamma/2\pi \approx 18$ MHz [20, 21]). The measured temperature after cooling is consistent with the Doppler cooling limit of ≈ 0.5 mK. The cooling sequence also optically pumps the population into $|^2S_{1/2}, 2, -2\rangle$ with a measured purity $\geq 98.6\%$. For repump measurements, the population is then coherently transferred to either of the other initial $|^2S_{1/2}, F, m_F\rangle$ states using a sequence of microwave pulses.

After the population is initiated into the desired state, an optical spectroscopy pulse is applied to the ion. In all cases the intensity on the ion corresponds to a saturation parameter of $S_0 \leq 0.02$. Each point is the average of 200 individual measurements. A single lineshape is generated from a further 4 to 6 averages of 200 points over a scan range of about $\pm$ 60 MHz, with the order of measurement points randomized for each cycle. For measurements on the σ^- closed cycling transition (Figure 4.1, A), a 250 μs pulse is applied and photons are

counted as the frequency is adjusted in steps across the transition. For repump measurements (Figure 4.1, B and C), the pulse duration is set between $\approx 5 - 50$ μs and adjusted to limit repump saturation broadening.

While measurements (A) and (B) scatter only through a single excited state, it is necessary to account for several non-zero scattering amplitudes in measurement (C). This is done using the quantum interference formalism presented in [6], that was simplified for repump style measurements starting from a single ground state in [45]. As a brief summary, the scattering rate from initial ground state $|i\rangle$ to final ground state $|f\rangle$, with scatter through intermediate excited states $|F', m'\rangle$ is calculated according to,

$$R_{i\to f} = \frac{I}{I_0}\left(\frac{\Gamma}{2}\right)^3 \left| \sum_{F'} \frac{(A^{F'm'}_{F_f m_f})_{q_s}(A^{F'm'}_{F_i m_i})_{q_L}}{\Delta^{F'}_{F_i} + i\Gamma/2} \right|^2, \tag{4.1}$$

with a sum of amplitudes within the square capturing the interference between the components. I_0 is a defined reference intensity, Γ is the natural linewidth of the transition and $\Delta^{F'}_{F_i}$ is the laser detuning. The expression here is already simplified for the case of a single initial state, laser polarization q_L and scattering polarization q_s. The numerator contains the relative scattering amplitude of a given component, proportional to the product of excitation and decay matrix elements. Interference between states is most prominent for unresolved structure, where the relative detuning between the components is small compared to the natural linewidth. More details are given in the quantum interference section and references [6, 45].

The relative scattering amplitudes for measurement (C) are given in Figure 4.2. Scatter from $|^2P_{3/2}, 1, 0\rangle$ is measured by preferential detection of the generated $|^2S_{1/2}, 2, 0\rangle$ population. Quantum interference is helpful in suppressing scatter to both $|^2S_{1/2}, 2, -1\rangle$ and $|^2S_{1/2}, 1, -1\rangle$, which improves measurement specificity and contrast.

The final step of each repump measurement sequence is resonant state detection. The unequal brightness of $|^2S_{1/2}, F, m_F\rangle$ states is used to preferentially detect individual components. Any population in the $|^2\mathrm{S}_{1/2}, 2, -2\rangle$ state produces the most PMT counts, followed by population in $|^2\mathrm{S}_{1/2}, 2, -1\rangle$ and $|^2\mathrm{S}_{1/2}, 2, 0\rangle$. If a state population other than $|2, -2\rangle$ needs to

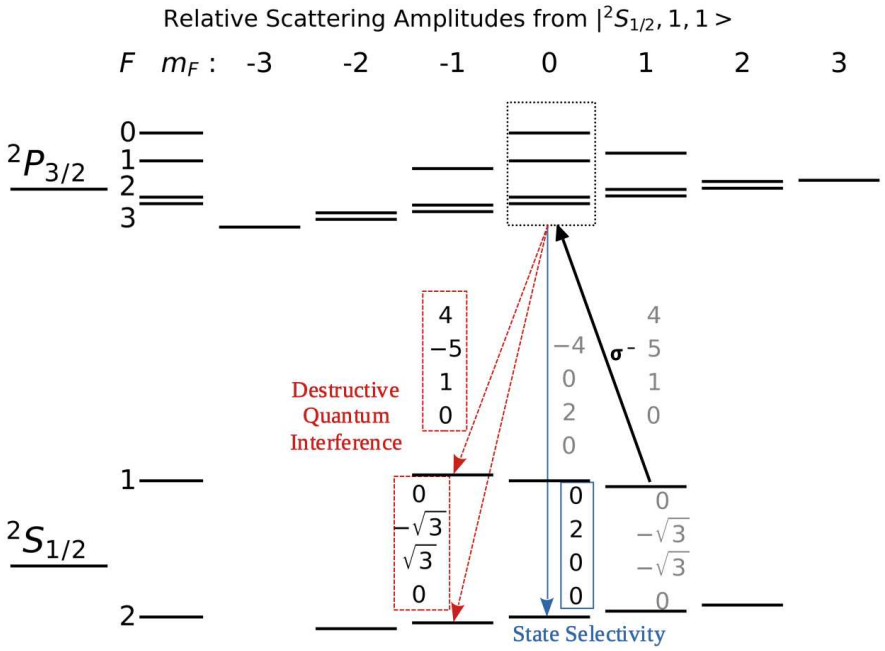

Figure 4.2: Relative scattering amplitudes for measurement C, with σ^- polarization and population starting in $|^2S_{1/2}, 1, 1\rangle$. The four numbers listed (top to bottom) for each final state represent amplitudes associated with scatter through $^2P_{3/2}$ excited states $F = 0, 1, 2, 3$, $m_F = 0$, respectively. The values are products of the excitation matrix element from initial state $|^2S_{1/2}, 1, 1\rangle$ and the decay matrix element to each given final state. Population starting in $|^2S_{1/2}, 1, 1\rangle$ can scatter to $|^2S_{1/2}, 2, 0\rangle$ only through $|^2P_{3/2}, 1, 0\rangle$ (all other amplitudes are zero). Population scattering to $|^2S_{1/2}, 1, -1\rangle$ and $|^2S_{1/2}, 2, -1\rangle$ is largely suppressed by quantum interference (the sum of the amplitudes is zero), outside of the effects of the small relative detuning differences between hyperfine components. This helps to improve the contrast of the signal. After the spectroscopy pulse, final state populations are exchanged using microwave pulses to preferentially detect the generated $|^2S_{1/2}, 2, 0\rangle$ component.

be measured, a series of microwave pulses is used to move that population to $|2, -2\rangle$ and put other major population components into darker states. In the particular case of measurement (C), microwave pulses are applied which rearrange the final $|F, m_F\rangle$ state populations $|2, -2\rangle \rightarrow |2, -1\rangle$, $|2, -1\rangle \rightarrow |2, 0\rangle$, and $|2, 0\rangle \rightarrow |2, -2\rangle$, to enhance the $|2, 0\rangle$ component.

The number of counts detected from each final state during a readout pulse is calibrated experimentally. In this case the typical relative brightness of the $F = 2$ ground states from $m_F = -2$ to $m_F = +2$ are approximately 1, 0.38, 0.18, 0.06, and 0.05, respectively. This trend can also be predicted from the relative probabilities of decays to $F = 1$ dark states using the quantum interference model. All of the $|^2S_{1/2}, F = 1\rangle$ states are relatively

dark due to the ≈ 1.25 GHz detuning, but do still generate some small residual counts of approximately 0.05, 0.04 and 0.03, respectively for $m_F = -1$ to $m_F = +1$.

The full lineshape model is generated by first calculating the relative scattering amplitudes and rates of population transfer using the quantum interference formalism [6, 45], solving the differential equations as an initial value problem to determine the expected final $^2S_{1/2}$ population distribution, and then scaling the populations by the calibrated brightness of each state during resonant D_2 detection. A simulated lineshape for measurement (C) applying this methodology is shown in Figure 4.3.

4.4 Characterization of Shifts and Uncertainties

A summary of measurement uncertainties is shown in Table 4.1. The dominant common systematic uncertainty is due to a slight residual slope in the power stabilization of the laser across the frequency range spanned by each double pass AOM. The stabilization is within 3% across the full scan range, which contributes up to 25 kHz uncertainty in determination of the line center. Because the beams for the cycling transition and repump are shifted through independent AOMs, with feedback parameters determined independently, we apply this uncertainty contribution from each beam in quadrature.

Photon recoil affects both the cycling transition and the repump measurements, with a correction applied individually to each. These effects have been characterized previously [45], and both the effective photon recoil shift and heating are accounted for here. The recoil and heating corrections mostly cancel when measuring a frequency difference between cycling and repump measurements, with a residual relative correction of 25 kHz. This correction is attributable to the mild difference in heating during a closed cycling transition measurement versus a repump measurement which scatters fewer photons. The uncertainty in the correction is $\pm$ 25 kHz, related to calibration of the heating and number of scattering events.

The observed lineshape in the $\Delta\nu_{31}$ measurement depends mildly on the repump pulse duration and intensity. A correction is applied individually to each measurement depending

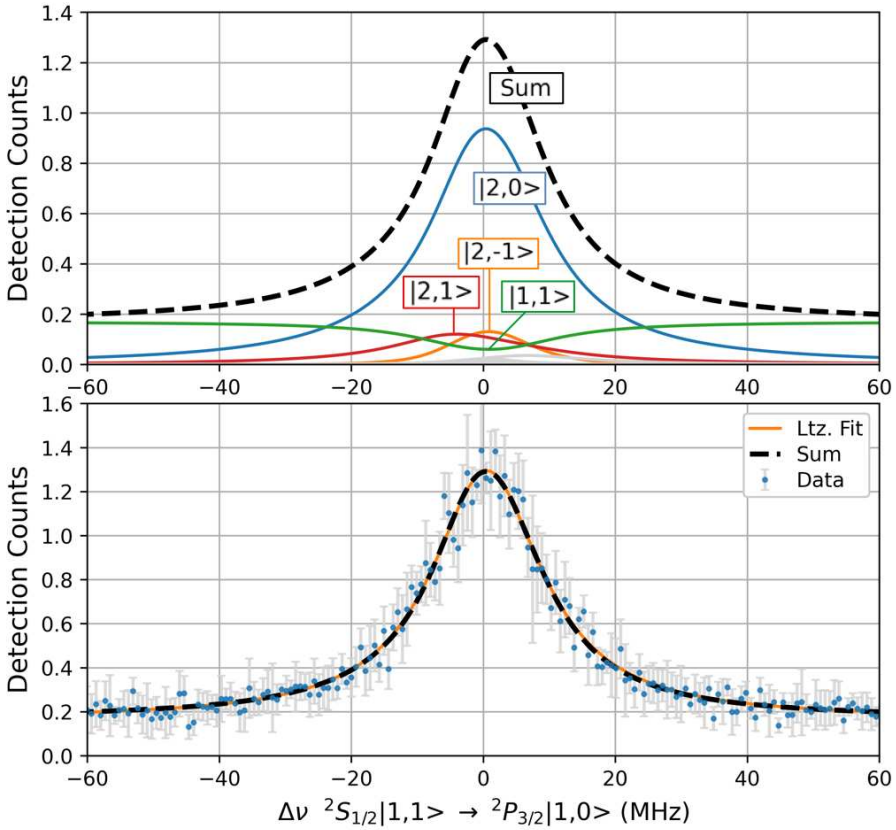

Figure 4.3: (Top) Calculated spectral contributions for measurement (C) in the case of a moderate duration spectroscopy pulse. The major contributions from individual final state populations are labeled. Population ending in $|^2S_{1/2}, 2, 0\rangle$ comes primarily from scatter from $|^2S_{1/2}, 1, 1\rangle$ through $|^2P_{3/2}, 1, 0\rangle$ and is detected preferentially by moving the $|2, 0\rangle$ population to the brightest state, $|2, -2\rangle$. Other major populations generated are exchanged to darker states to reduce their contributions to the lineshape. The total lineshape, when fit with a single component Lorentzian, appears shifted higher in frequency by approximately 200 kHz, with some pulse duration dependence. This originates from imperfect isolation of the final $|^2S_{1/2}, 2, 0\rangle$ population, and from secondary scatter during the spectroscopy pulse as some population also starts to accumulate in $|^2S_{1/2}, 1, 0\rangle$. (Bottom) A single dataset is shown for measurement (C), with statistical error bars on individual points. The data is fit with a Lorentzian lineshape (orange). The total calculated lineshape from the top section (black dashed) is superimposed over the data.

on the experimental conditions and ranges from -100 kHz to -300 kHz. Calibration of the experimental conditions used in the model contributes an uncertainty of 50 kHz in the extracted transition frequency, which is applied as a common systematic in the $\Delta\nu_{31}$ results.

Polarization impurity contributes only a negligible systematic uncertainty in these measurements. The σ^- polarization, which all spectroscopy beams share, can be tuned with such precision (by iteratively adjusting a combination of polarizer, waveplates with both

Table 4.1: Statistical and systematic uncertainties in kHz for the $^2P_{3/2}$ hyperfine splittings, $\Delta\nu_{32}$ and $\Delta\nu_{31}$.

Effect	$\Delta\nu_{32}$	$\Delta\nu_{31}$
Statistical variation	35	49
Optical power stabilization	36	36
Photon recoil effects	25	25
Scattering lineshape model	0	50
Magnetic field drift	< 2	< 2
AC Stark shift (optical)	< 1	< 1
Imperfect laser polarization	< 1	< 1
Total	56	83

axial rotation and tip/tilt, beam pointing and magnetic field, while observing histograms of the cycling transition counts) that σ^+ and π impurity components are negligible [45].

To extract the final frequency splittings, we apply corrections for the ground state hyperfine splittings and the ground and excited state Zeeman shifts due to applied bias magnetic field. Ground state contributions are calculated with the generalized Breit-Rabi formula, using the experimentally determined value $A_{S_{1/2}} = -625\ 008\ 837.044(12)$ Hz [24]. The Zeeman corrections for the excited states are first approximated assuming a linear shift. We then take the best-fit hyperfine coefficients and iteratively determine the full magnetic field shift, including the hyperfine-associated curvature, using the eigenvalues of the combined $^2P_{3/2}$ hyperfine and Zeeman Hamiltonian.

The theoretical excited state hyperfine constants used for comparison in this work are $A_{P_{3/2}} = -1.023(3)$ MHz, and $B_{P_{3/2}} = 2.290(6)$ MHz [3, 22, 63]. The value for the $B_{P_{3/2}}$ coefficient is corrected to account for a previous sign error in the literature and is scaled using the latest extracted value for the ^{9}Be nuclear electric quadrupole moment [63, 64]. It should be noted that the hyperfine coefficients given are effective values, already adjusted to account for second order hyperfine induced fine structure mixing of the ^2P manifold and various other corrections [3]. The ^{9}Be nuclear magnetic octupole moment has not yet been measured, but was approximated at $\Omega = -0.073\ (b \times \mu_N)$ [65]. A corresponding first order $C_{P_{3/2}}$ coefficient has not been reported. We have calculated the second order

hyperfine induced fine structure mixing contribution. By combining any two of the three reported fine structure mixing corrections from [3], $\delta A_{P_{1/2}} = -6.83$ kHz, $\delta A_{P_{3/2}} = -2.76$ kHz and $\delta B_{P_{3/2}} = -18.03$ kHz, with the equations for the $I = \frac{3}{2}$ case in [66], it is possible to determine the second order coefficients $\eta = -516.4$ kHz, $\zeta = -36.5$ kHz. The coefficients lead to a correction term $\delta C_{P_{3/2}} = -0.041$ kHz. This contribution is negligible at the present measurement uncertainty.

4.5 Results and Discussion

Individual measurement results are shown in Figure 4.4, with final uncertainty weighted results in Table 4.2. The measurements of $\Delta\nu_{32}$ and $\Delta\nu_{31}$ agree with the calculated values [3], within the experimental uncertainty. Further experimental precision could enable a more stringent test or help determine the effective $C_{P_{3/2}}$ coefficient and extract the magnetic octupole moment. It should be possible to improve the power stability of the spectroscopy laser by using a faster feedback method. To reduce the uncertainty due to photon recoil heating, it would be possible to add a sympathetic cooling ion, use lower exposure spectroscopy pulses or apply stronger trap confinement. To reach the few kHz level of uncertainty with this method would require splitting the 20 MHz linewidth by about one part in 4000. An additional technique that might help reduce the uncertainty in the recoil heating correction is decoherence-assisted spectroscopy, as presented in the context of strong transition measurements in $^{25}Mg^{+}$ [67]. We would like to thank Didi Leibfried for suggesting this technique upon discussion of these results.

This work represents the first direct optical measurements of two unresolved hyperfine splittings of the $^2P_{3/2}$ manifold in $^9Be^{+}$. The measurements to $|^2P_{3/2}, F = 1\rangle$ demonstrate a particular adaptation of repump spectroscopy utilizing quantum interference and selection rules to distinguish otherwise unresolved structure. The final results for the splittings are in good agreement with calculation using hyperfine constants from theory, within the experimental uncertainty.

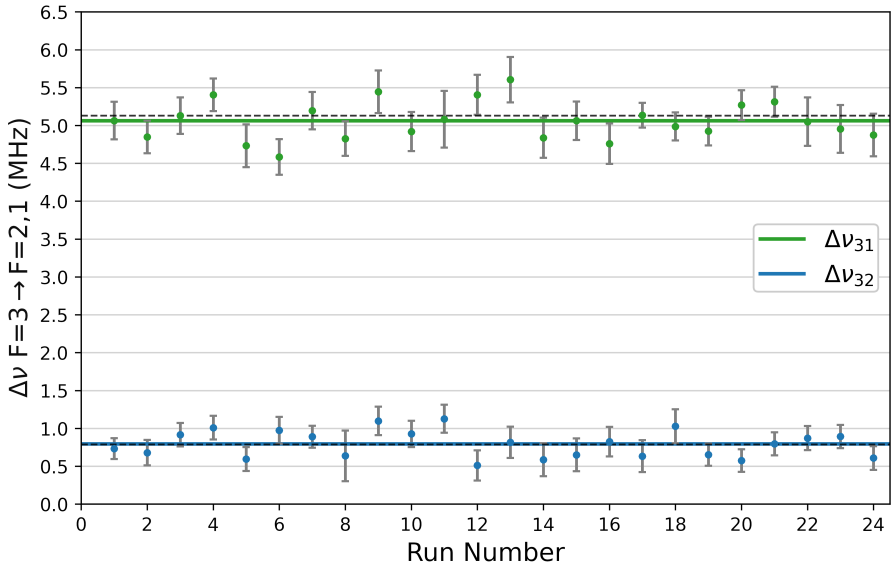

Figure 4.4: Consecutive measurements are shown for $\Delta\nu_{31}$ (top) and $\Delta\nu_{32}$ (bottom). The minor Zeeman contributions to the ground and excited states have been removed to give the zero field values. Splittings calculated from the effective hyperfine constants from theory are shown as dashed lines, with uncertainty weighted fits to the experimental data shown as solid lines. Error bars represent the statistical uncertainty for each individual measurement set. The reduced χ^2 for $\Delta\nu_{31}$ and $\Delta\nu_{32}$ measurements are 1.00 and 0.97, respectively. Note that the upper and lower data is not correlated since $\Delta\nu_{31}$ and $\Delta\nu_{32}$ measurements were taken on different days.

Table 4.2: Measured $^2P_{3/2}$ hyperfine splittings, $\Delta\nu_{32}$ and $\Delta\nu_{31}$, in comparison to calculated values. The effective hyperfine constants, $A_{P_{3/2}}$ and $B_{P_{3/2}}$, from theory are listed. The extracted hyperfine constants are a best fit to the two measured splittings. All values are in units of MHz.

$\Delta\nu_{32}$	$\Delta\nu_{31}$	$A_{P_{3/2}}$	$B_{P_{3/2}}$	Ref.
0.788	5.130	-1.023(3)	2.290(6)	Theory[a]
0.801(56)	5.050(83)	-1.01(2)	2.23(8)	This Work

[a]M. Puchalski, K. Pachucki, (2009) [3]

4.6 Theory of the Combined $^2P_{3/2}$ Hyperfine-Zeeman Hamiltonian

When the magnetic field and hyperfine shifts are of similar order of magnitude, such as in the $^2P_{3/2}$ manifold of $^9Be^+$, the two effects must be combined into a single Hamiltonian to accurately solve for the eigenstates as a function of magnetic field strength. For the $J = \frac{1}{2}$ case, this leads to the Breit-Rabi formula, which was used in this work for calculations of the $^2S_{1/2}$ and $^2P_{1/2}$ manifolds. For the $^2P_{3/2}$ manifold ($J = I = \frac{3}{2}$), there is no simple algebraic solution but the two effects can be written as 16x16 matrices and summed. The hyperfine

Hamiltonian is diagonal in the $|I, J, F, m_F\rangle$ basis, while the Zeeman interaction is diagonal in the $|I, m_I, J, m_J\rangle$ basis. Thus, we also need the appropriate matrix to transform between the two basis sets, which is comprised of a block diagonal set of Clebsch-Gordan coefficients.

The hyperfine interaction can be written as [53],

$$H_{HFS} = \frac{1}{2}A_{hfs}K + B_{hfs}\frac{\frac{3}{2}K(K+1) - 2I(I+1)J(J+1)}{4I(2I-1)J(2J-1)} + C_{hfs}\frac{5K^2(K/4+1) + K[I(I+1) + J(J+1) + 3 - 3I(I+1)J(J+1)] - 5I(I+1)J(J+1)}{I(I-1)(2I-1)J(J-1)(2J-1)}, \tag{4.2}$$

where $K = F(F+1) - I(I+1) - J(J+1)$.

The Zeeman interaction can be written as,

$$H_Z = (m_I g_I + m_J g_J)\mu_B B. \tag{4.3}$$

Since these two effects are naturally written in two different basis sets, we need a transformation matrix to be able to sum the effects in the same basis. The completeness relation in quantum mechanics allows decomposition of any vector $|\Psi\rangle$ into a sum of basis vectors $|\phi_i\rangle$ as, $|\Psi\rangle = \sum_i |\phi_i\rangle \langle\phi_i|\Psi\rangle$.

If we take $|\Psi\rangle$ to be a vector in the combined angular momentum $|F, m_F\rangle$ basis and $|\phi_i\rangle$ to be the $|I, m_I, J, m_J\rangle$ basis,

$$|F, m_F\rangle = \sum_{m_I}\sum_{m_J} |I, m_I, J, m_J\rangle \langle I, m_I, J, m_J|F, m_F\rangle . \tag{4.4}$$

The matrix elements on the right side are Clebsch-Gordan coefficients, which can be looked up in a table or calculated using the sympy package in Python. From there all that is necessary is to build the matrices. If the matrix of Clebsch-Gordan coefficients is M, the Zeeman effect matrix H_Z can be transformed to the combined basis as $H_{Z_{(F,m_F)}} = MH_ZM^{-1}$, and summed with the H_{HFS} Hamiltonian in the same basis set. The eigenvalues can then

be found numerically for any value of the magnetic field. The calculated results for the $^2P_{3/2}$ manifold in $^9Be^+$ are shown in Figure 4.5.

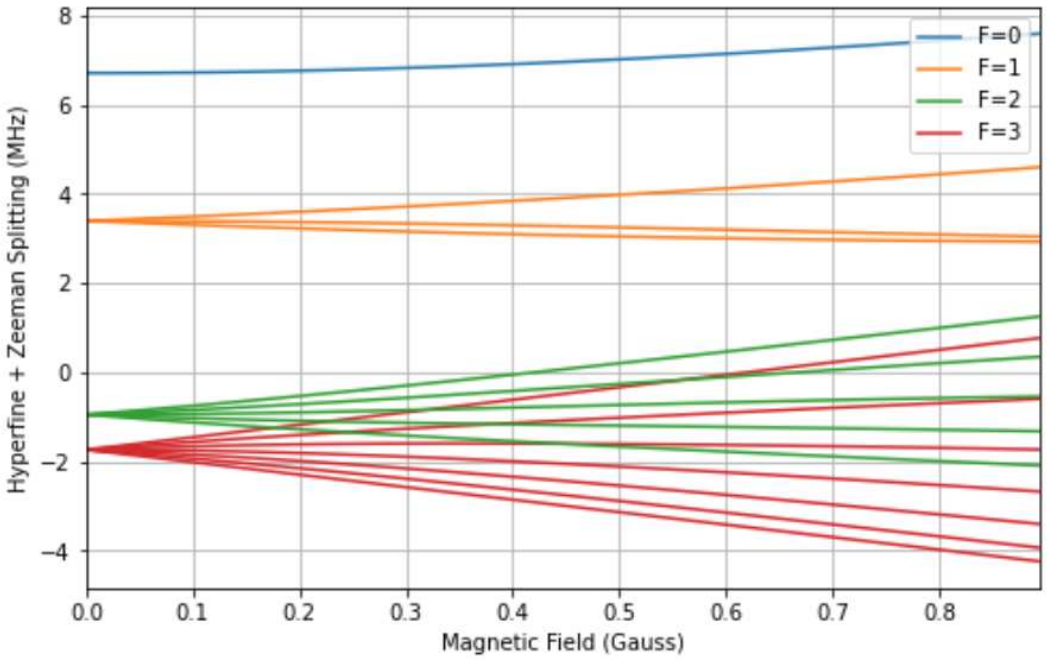

Figure 4.5: A plot showing the combined effects of the Zeeman and Hyperfine interactions versus magnetic field in the $^2P_{3/2}$ manifold of $^9Be^+$. The D-line and ground state hyperfine constant measurements were taken at 0.895 Gauss, whereas the $^2P_{3/2}$ hyperfine measurements were taken at 0.1343 Gauss, prior to any level crossings.

Chapter 5

Lifetime of the $^2P_{1/2,3/2}$ Excited States.

5.1 Introduction

The typical lifetime value referenced for the $^2P_{1/2,3/2}$ excited states is $\tau = 8.1(4)$ ns, measured in 1969 by Andersen *et al.* [20]. This corresponds to a natural linewidth of $\Gamma/2\pi \approx 19.6$ MHz. More recently, however, a calculation from M. S. Safranova set a more precise theoretical value for the lifetimes and linewidth at $\tau = 8.850(2)$ ns and $\Gamma/2\pi = 17.98$ MHz [21]. Two approaches were taken here to obtain an improved experimental value of the lifetimes. The first approach was analysis of the lineshapes of already existing data from the original D_2 measurements and from the later $^2P_{3/2}$ hyperfine splitting measurements. The second approach was to measure the off-resonant pumping rate, using far detuned light, of population out of the $|^2S_{1/2}, 1, -1\rangle$ sublevel, and compare that to a measured AC stark shift from the same beam.

5.2 Analysis Of Existing D_2 Lineshapes

As there already existed over 70 usable D_2 data sets with full lineshapes, this first approach was just a matter of correcting for small contributions from photon recoil and saturation broadening to extract a lifetime. The code already built to simulate photon recoil lineshapes was used to generate the first correction, and the saturation broadening correction was applied based on optical power measurements and calibrated collection efficiency. This allowed separate adjustment for conditions during each individual measurement. The results are shown in Figure 5.1. The extracted value in this approach was $\tau = 8.79(9)$ ns, in closer agreement with the $\tau = 8.850(2)$ ns theory value [21] than the previous experimental value of $\tau = 8.1(4)$ ns [20].

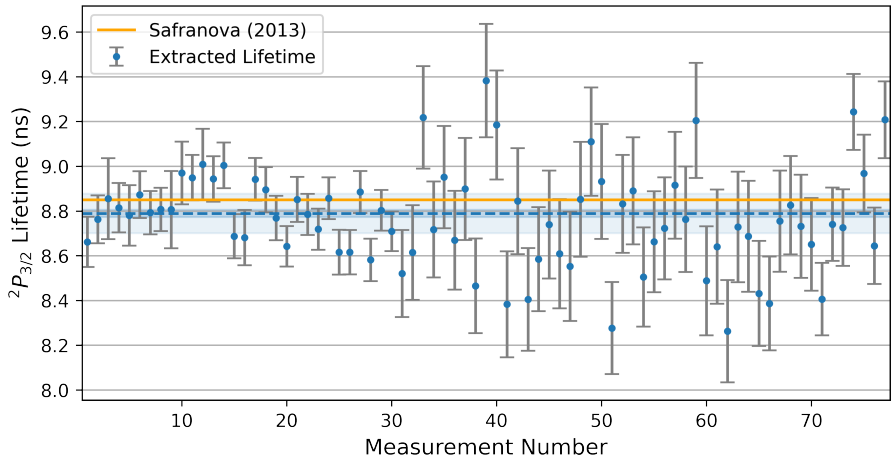

Figure 5.1: The extracted lifetime from corrected D_2 lineshapes are shown in the figure. Corrections were applied for photon recoil and saturation broadening. The theory value of 8.850(2) ns from [21] is shown as a solid orange line. The total uncertainty-weighted experimental fit is shown as a dashed line with uncertainty band in light blue. The experimental fit of 8.79(9) ns is in good agreement with the value from theory. The previous experimental value was 8.1(4) ns [20].

5.3 Off-Resonant Pumping Rate and AC Stark Shift

The general approach and experimental demonstration of extracting an excited state lifetime from the ratio of measurements of a pumping rate and an AC stark shift from far off resonant light has been detailed in a number of publications [68–71]. We believed this could potentially be adapted for an off-resonant σ^- D_1 pumping experiment out of the $|^2S_{1/2}, 1, -1\rangle$ ground state. We obtained data under several detuning conditions over about one week. In this experiment, light detuned by Δ from the $|^2S_{1/2}, 1, -1\rangle \rightarrow |^2P_{1/2}, 2, -2\rangle$ transition is applied for some duration, which causes population to move into states $|^2S_{1/2}, 2, -2\rangle$ and $|^2S_{1/2}, 2, -1\rangle$. The AC stark shift of $|^2S_{1/2}, 1, -1\rangle$ can be written as,

$$\delta_{AC} = \frac{\Omega^2}{4\Delta}, \tag{5.1}$$

and the pumping rate of population out of $|^2S_{1/2}, 1, -1\rangle$ is

$$\mathcal{R} = A(1-p)\frac{\Omega^2}{4\Delta^2}, \tag{5.2}$$

where p is the effective branching fraction which returns back to $|^2S_{1/2}, 1, -1\rangle$ and A is the total spontaneous decay rate from $|^2P_{1/2}, 2, -2\rangle$. The branching ratios from $|^2P_{1/2}, 2, -2\rangle$ to $|^2S_{1/2}, 1, -1\rangle$, $|^2S_{1/2}, 2, -2\rangle$ and $|^2S_{1/2}, 2, -1\rangle$ are $\frac{1}{2}$, $\frac{1}{3}$ and $\frac{1}{6}$, respectively. There are two general scenarios for the value of p. If the detuning from the $F = 2$ ground state is relatively large, the effective value for p is $\frac{1}{2}$ as population leaves $|^2S_{1/2}, 1, -1\rangle$ to $|^2S_{1/2}, 2, -2\rangle$ and $|^2S_{1/2}, 2, -1\rangle$ and remains there. If the detuning from the $F = 2$ ground state is small, the effective value for p is $\frac{3}{5}$, since population moved to $|^2S_{1/2}, 2, -1\rangle$ can scatter again quickly with some of the population going back to $|^2S_{1/2}, 1, -1\rangle$. Taking the ratio of Equation 5.1 and Equation 5.2 and solving for the lifetime $\tau = 1/A$ yields

$$\tau = \frac{(1-p)}{\Delta}\frac{\delta_{AC}}{\mathcal{R}}, \tag{5.3}$$

which is equivalent to Eq. (4) in [71]. For the experiment, it is convenient to write instead in terms of the measured pumping time constant, $\tau_{meas} = 1/\mathcal{R}$,

$$\tau = \left[\frac{(1-p)\delta_{AC}}{\Delta}\right] \times \tau_{meas}. \tag{5.4}$$

For an off-resonant D_1 measurement, if the σ^- polarization is reasonably pure, the ground state $|^2S_{1/2}, 2, -2\rangle$ level should have no AC stark shift, as there is no upper state level to which it couples. Therefore, the AC stark shift on $|^2S_{1/2}, 1, -1\rangle$ can be obtained directly by measuring the microwave transition frequency $\nu_{-2,-1} = |^2S_{1/2}, 2, -2\rangle \rightarrow |^2S_{1/2}, 1, -1\rangle$ with and without the off-resonant beam turned on.

Experimental implementation of the method was attempted both on the D_2 and D_1 transitions using σ^- polarization. A typical data set is comprised of a D_2 measurement to determine the exact detuning, a pump out time constant measurement, and measurements of the microwave transition with and without the repump beam turned on. An example is shown in Figure 5.2.

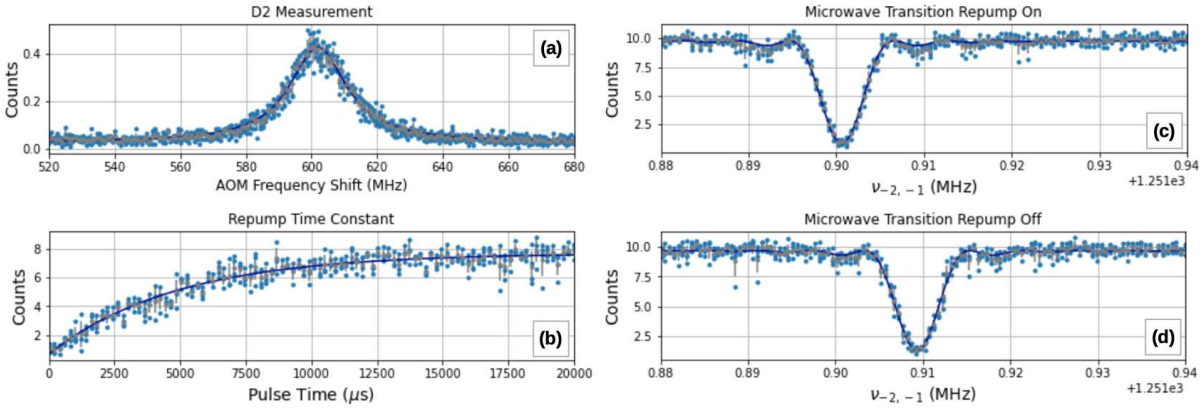

Figure 5.2: A typical dataset is shown. There are four measurements taken for each set, a D_2 measurement to determine the detuning (a), a time constant measurement for off resonant repump (b), and measurements of the microwave transition with and without the repump beam on to determine the AC Stark shift (c,d).

Unfortunately, there was unexpected variability in the results, with extracted values for the lifetime ranging from about 7 ns to 11 ns. We think that the variability is related to the complicating factors of secondary scattering and, possibly, polarization purity dependence. While this still seems a promising approach, the closeness of the ground state hyperfine sublevels (compared to the large fine structure splittings used in other works) complicates the experiment, and has been left for further consideration in the future.

Chapter 6

$^9Be^+$ $^2S_{1/2}$ Hyperfine Constant

6.1 Introduction

The ^{9}Be nuclear Zemach radius (defined as the convolution of the nuclear magnetic moment with the nuclear charge radius) can be extracted by comparison of the point nucleus-based theoretical prediction for the ground state hyperfine constant, $A_{S_{1/2}}$, with measurements [72]. Deviations from the theoretical prediction can be attributed to the finite nuclear charge and magnetic moment distributions.

Exceptionally precise measurements of the ground state hyperfine splitting were performed at high magnetic field (0.5-4.5 T) in a Penning trap at NIST as recently as 2011 [12, 24, 25]. There had not, however, been a similar measurement at low field and the favorable conditions within the linear rf trap suggested a similarly precise measurement could be performed here. Our objective was to perform time delay Ramsey spectroscopy of the magnetic field insensitive $|^2S_{1/2}, F = 2, m_F = 0\rangle \rightarrow |^2S_{1/2}, F = 1, m_F = 0\rangle$ microwave transition and investigate the accuracy that could be achieved in our system. Many of the experimental techniques and the uncertainty characterization closely follow similar experiments performed on magnesium ions [73]. Performing these measurements allowed us to characterize the residual trap-induced AC magnetic field at the location of the ion, for comparison to previous versions of the trap wafer.

6.2 Apparatus

The trap and laser systems used in these measurements are described in previous sections. The basic apparatus consists of an rf Paul trap and a frequency stabilized UV laser at 313 nm for Doppler cooling, optical pumping and state readout. Most of the experimental parameters are the same as those used in the D line measurements, however, here we perform

time delay Ramsey spectroscopy with microwave pulses to determine the first-order magnetic field insensitive $|^2S_{1/2}, F = 2, m_F = 0\rangle \rightarrow |^2S_{1/2}, F = 1, m_F = 0\rangle$ transition frequency, $\nu_{0,0}$, and extract $A_{S_{1/2}}$.

The ion trap operates with an rf drive frequency of $\Omega_{rf}/2\pi = 78.93$ MHz and a differential drive amplitude of approximately $\pm$ 168 V. The secular mode frequencies of a single $^9Be^+$ ion are $\omega_z/2\pi \approx 3.65$ MHz for the axial mode, and $\omega_x/2\pi \approx 9.8$ MHz and $\omega_y/2\pi \approx 10.6$ MHz for the radial modes (in the plane of the trap wafer). The quantization axis magnetic field is characterized and maintained at the typical operating point of 0.0895 mT by measurement of the field sensitive $|^2S_{1/2}, 2, -2\rangle \rightarrow |^2S_{1/2}, 1, -1\rangle$ transition frequency, $\nu_{-2,-1}$ ($\approx$ 1251.9 MHz).

A single ion is loaded via laser ablation of a beryllium wire located on the far trap endcap. The ion is monitored on a UV sensitive camera to ensure there remains only one ion in the trap at any time. Occasionally, a sympathetically cooled dark ion will be found, which can be easily identified as it shifts the center location of the bright ion on the camera. The two also occasionally swap location from random residual background gas collision. If a second ion is found, the trap is dumped and reloaded.

A 50 mm diameter rf loop antenna is positioned approximately 1 mm above the fluorescence collection window, outside the vacuum chamber above the trap. This is used to drive all microwave transitions between the various sublevels in the ground $^2S_{1/2}$ manifold. The frequencies and pulses are generated by an externally referenced ARTIQ control system using an AD9912 DDS channel, with a resolution of 4 μHz. The base rf frequencies are doubled twice to reach the required range of $\approx$ 1.25 GHz. This is then amplified and filtered for suppression of harmonic components. The π times for ground state transitions with the available rf power are approximately $100 - 200$ μs.

6.3 State Preparation

Prior to each measurement, the ion is cooled using 1 ms of far-detuned ($\Delta/2\pi = -415$ MHz) laser cooling and 500 μs of near-detuned Doppler cooling ($\Delta/2\pi = -10$ MHz) on the

$|^2S_{1/2}, 2, -2\rangle \rightarrow |^2P_{3/2}, 3, -3\rangle$ cycling transition ($\Gamma/2\pi \approx 18$ MHz [20, 21]). The measured temperature after cooling agrees with the Doppler cooling limit of ≈ 0.5 mK. The laser has precisely tuned σ^- polarization, which pumps the population into the $|^2S_{1/2}, 2, -2\rangle$ ground state. Histograms are recorded, from which the state purity can be inferred from the ratio of counts in the dark bins compared to the main Poisson distribution, as previously shown in Figure 3.9. A typical state preparation results in ≥ 98.6 % population being initialized into the $|^2S_{1/2}, 2, -2\rangle$ state.

6.4 Readout

Experimental data is recorded as counts on a photomultiplier tube (PMT). State readout is achieved via resonant detection on the $|^2\mathrm{S}_{1/2}, 2, -2\rangle \rightarrow |^2\mathrm{P}_{3/2}, 3, -3\rangle$ D_2 transition, which can distinguish between population in the $F = 2$ bright states versus the $F = 1$ dark states. All points are averages of ≈ 40 repetitions, which was chosen as a balance between measurement rate and quantum projection noise. The details of quantum projection noise in this type of two level system are summarized in [74].

In the $\nu_{0,0}$ Ramsey measurement, the population is first coherently moved to $|1, 0\rangle$ via frequency resolved microwave pulses. After the probe, a pulse sequence is applied to map the $|2, 0\rangle$ and $|1, 0\rangle$ populations to states with greater contrast for better signal to noise ratio. The $|2, 0\rangle$ population is shelved in the $|1, 1\rangle$ dark level, while the $|1, 0\rangle$ population is transferred to $|2, -2\rangle$, the brightest state. An energy level diagram with transitions used in the measurement sequence is shown in Figure 6.1.

6.5 Clock Probe

The experiment is run as a clock with a two point probe by performing interleaved measurements with a detuning that corresponds to the mid-points of the transition probability for the $\nu_{0,0}$ zero order Ramsey spectrum peak. The relative transition probability from the

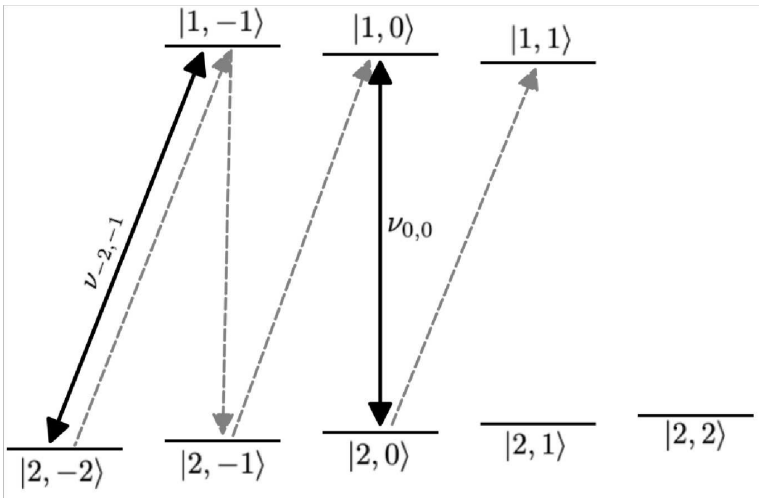

Figure 6.1: An energy level diagram is shown for the $^2S_{1/2}$ ground state in $^9Be^+$. The $\nu_{-2,-1}$ transition is used to characterize and stabilize the quantization axis magnetic field. Rabi measurements on this transition are interleaved with Ramsey measurements on the field insensitive transition $\nu_{0,0}$. Prior to the Ramsey probe, the population is coherently moved to $|1,0\rangle$ (first three dashed lines). After the Ramsey probe and prior to state readout, any $|2,0\rangle$ population is shelved in $|1,1\rangle$ (final dashed line) and $|1,0\rangle$ population is walked back to $|2,-2\rangle$ along the same path. This gives higher contrast for determining the relative $|2,0\rangle$ and $|1,0\rangle$ populations, though still limited by quantum projection noise.

two points provides feedback to track the center of the peak. The transition probability at the center frequency is also measured to maintain a record of the contrast of the line. The $\nu_{0,0}$ measurements are interleaved with a two point Rabi spectroscopy probe on the $\nu_{-2,-1}$ transition. This precisely tracks deviations in the magnetic field and is used to provide negative feedback on the quantization axis magnetic field coil to stabilize the magnetic field at the desired setpoint. It is also used to calculate the slight adjustments to the intermediate microwave transition frequencies required to ensure high fidelity population transfer between ground states. The recorded signals from a single measurement run are shown in Figure 6.2. Note that the particular data set was chosen to display the peak tracking with several magnetic field fluctuations, rather than data with the lowest noise. Since magnetic field noise is considerably lower after normal university operating hours, most of the data used in the final results was taken overnight.

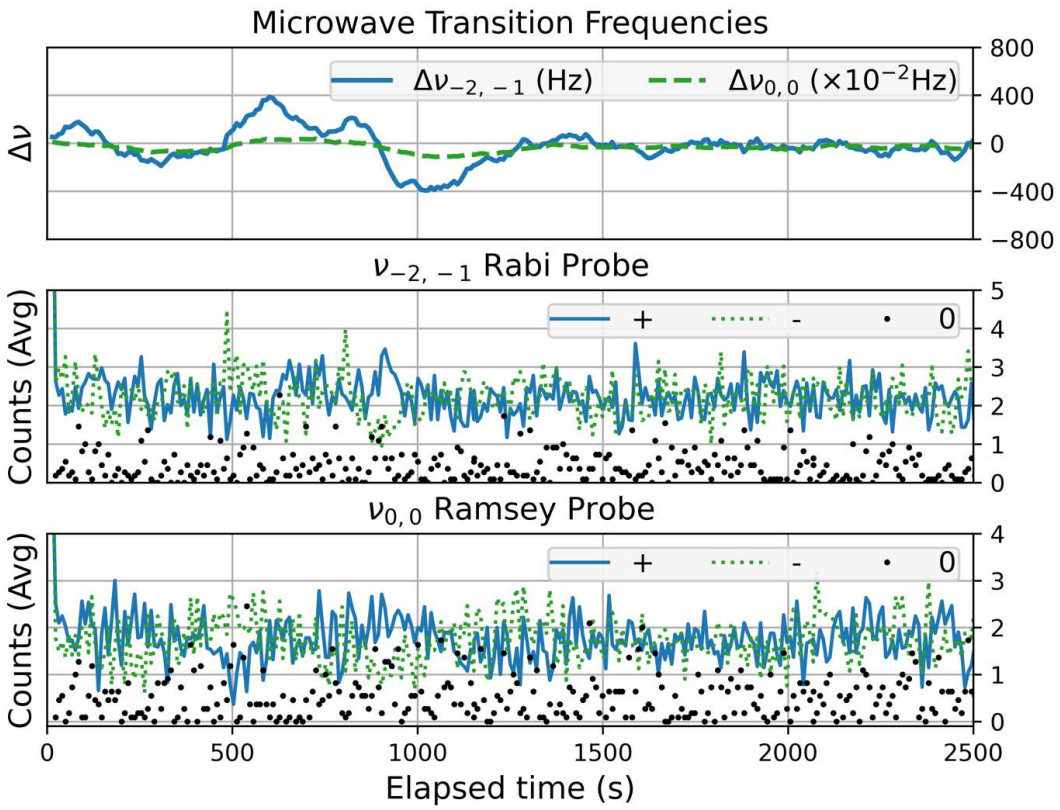

Figure 6.2: The measurement signals associated with peak tracking on a single measurement run are shown. The first ≈40 points are typically discarded to ensure sufficient time for initial tracking onto both peaks. The top plot shows the deviation in frequency of both the field sensitive and field insensitive transitions. Besides following any magnetic field fluctuations, there is also random walk associated with quantum projection and other white noise. The middle plot shows the two point probe data which tracks the $\nu_{-2,-1}$ transition for characterization and stabilization of the magnetic field. The bottom plot shows the two point Ramsey probe data. Measurements at the center point (a minimum in the current configuration) are also obtained to monitor the signal contrast.

6.6 Probe Shift

Ramsey spectroscopy measurements are subject to a small probe-induced frequency shift from the $\pi/2$ pulses, which decreases toward zero in the limit of long free-evolution time. In the case of a small shift relative to the Rabi frequency, this can be expressed as

$$\delta_\nu = \frac{(\Delta/2\pi)}{1 + (\frac{\pi}{4})(\frac{T_R}{\tau_p})}, \tag{6.1}$$

where T_R and τ_p are the free-evolution time and the $\pi/2$ duration, respectively [73, 75]. To characterize the shift, data sets were recorded with free-evolution times ranging from

$5 - 320$ ms with $\tau_p = 120$ μs. A plot of data associated with the probe-induced shift characterization with the global fit result are shown on the left panel in Figure 6.3. The extracted probe shift at $T_R = 160$ ms is 9.7 mHz.

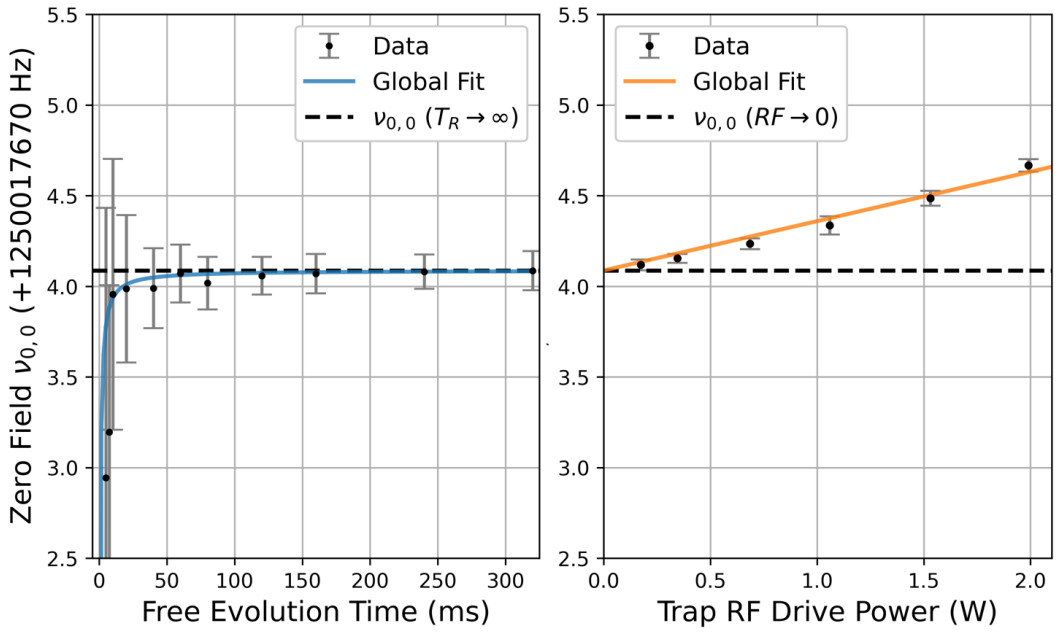

Figure 6.3: The probe dependent(left) and rf dependent (right) shift characterizations are shown. A global uncertainty-weighted fit to the experimental data was used in the analysis. The data shown are already corrected for DC magnetic field using the generalized Breit-Rabi formula for both $\nu_{-2,-1}$ and $\nu_{0,0}$. The probe shift data in the plot is corrected for a fixed AC Zeeman shift at 0.346 W. The AC Zeeman shift data is corrected for a fixed probe shift at T_R=160 ms.

6.7 AC Quadratic Zeeman Shift

There is also a small trap drive amplitude dependence attributed to an AC quadratic Zeeman shift due to imbalanced currents in the trap drive electrodes. Data using calibrated rf drive powers ranging from $0.1 - 2$ W were used for a linear extrapolation to the zero power transition frequency. Data used in the rf shift characterization with the global fit result are shown on the right panel in Figure 6.3. The extracted shift is 0.2723 Hz/W, which was used to estimate a residual AC magnetic field at the location of the ion of $\langle B_{ac}^2 \rangle = 0.9 \times 10^{-12}$ T^2/W. This field is approximately 4 times lower per Watt of applied rf power compared to the

measurements taken with $^{25}Mg^{+}$ at NIST using the previous wheel trap revision [73]. This result suggests that some of the trap wafer symmetry characteristics have been improved in this more recent design.

6.8 Results and Discussion

A comparison of the results at $B = 0.0895$ mT to the result obtained at $B = 4.64$ T [24] are shown in Figure 6.4b and Table 6.1. The two are in good agreement, and as such no corrections to theoretical calculations [72] of the Zemach radius of ^{9}Be are indicated by this additional measurement. The final result obtained here is $A_{S_{1/2}} = -625.008837044(10)$ Hz.

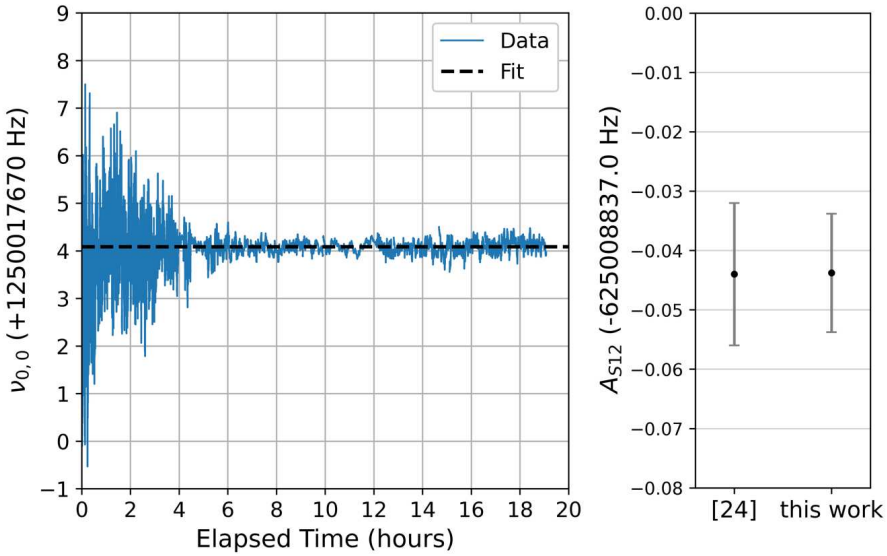

Figure 6.4: Fully corrected data over about 20 hours of collection time are shown in the figure(left). Sections with larger variations correspond to the data taken using shorter Ramsey free evolution time. The final extracted hyperfine constant in comparison to [24] is shown on the right.

Table 6.1: Table of experimental measurement results of the $^{9}Be^{+}$ ground state hyperfine constant.

$A_{S_{1/2}}$	Ref.
-625 008 837.044(12)	Exp.[a]
-625 008 837.044(10)	this work

[a] Shiga et. al. (2011) [24]

Chapter 7

Additional Ion Trap Characterization

7.1 Secular Mode Frequencies at Higher Radial Confinement

Since photon recoil heating was a limiting systematic uncertainty in all of the strong transition measurements, we chose to test if the trap could easily achieve secular mode frequencies beyond the 18 MHz D-line natural linewidth. This would allow us to observe a truly photon recoil-free spectrum in the strong-confinement regime.

The secular mode frequencies are most easily determined by applying a small rf 'tickle' either to the endcaps or to the compensation electrodes to address the axial or radial modes, respectively. In this method, when the applied rf frequency is equal to the secular mode frequency, the ion heats significantly leading to a reduction in the fluorescence level on resonance. When the rf "tickle" frequency is swept across the mode frequency, it is possible to observe a resonance line that can be used to extract the precise motional mode frequencies. Example rf tickle spectra are shown in Figure 7.1. The typical axial and radial mode frequencies for the experiments were $\omega_z/2\pi \approx 3.65$ MHz, $\omega_x/2\pi \approx 9.8$ MHz and $\omega_y/2\pi \approx 10.6$ MHz.

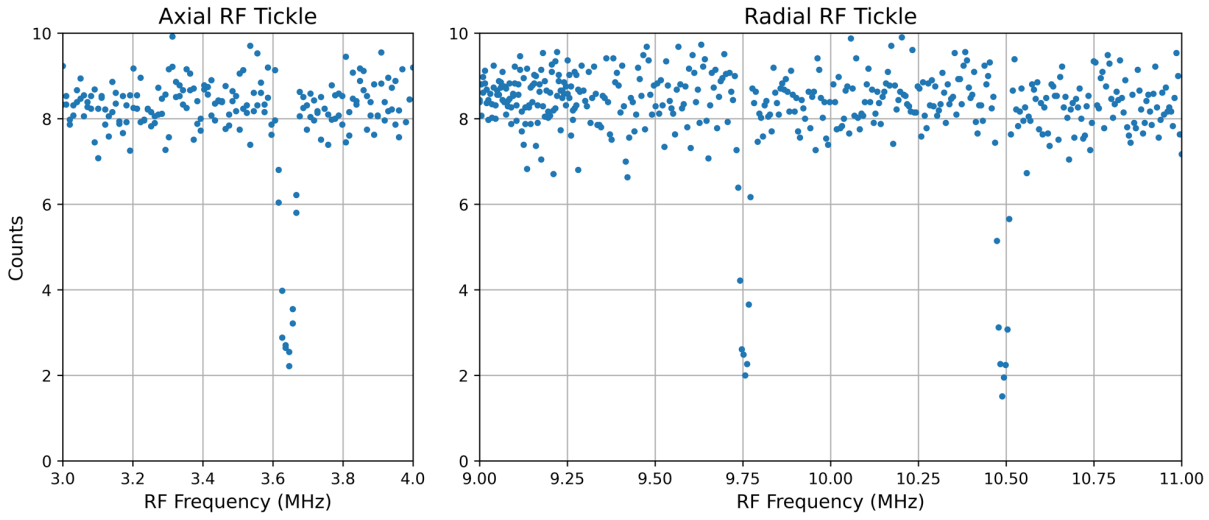

Figure 7.1: RF Tickle data for axial(left) and radial modes(right). For the axial mode the rf is applied to the endcap. For radial modes the rf is applied to the rf dc bias electrodes.

During the D line experiments, we typically operated the trap with an rf drive power of approximately 0.8 W, however, in the measurements of the ground state hyperfine constant we had increased the drive power as high as 2 W. Data of the mode frequencies up to this RF power was obtained and is shown in Figure 7.2. A table of the drive parameters and required vertical compensation voltage to minimize the micromotion along the σ^- detection axis is provided in Table 7.1. One detail about the compensation voltages is that the majority of the axial confinement was applied as a negative DC bias to the RF electrodes, rather than as a positive voltage to the endcaps. This approach can reduce axial heating rates as injected noise here tends to be common mode (as opposed to independent voltages on each endcap), but it does change the relative DC voltage between the RF electrodes and the vertical and horizontal compensation electrodes.

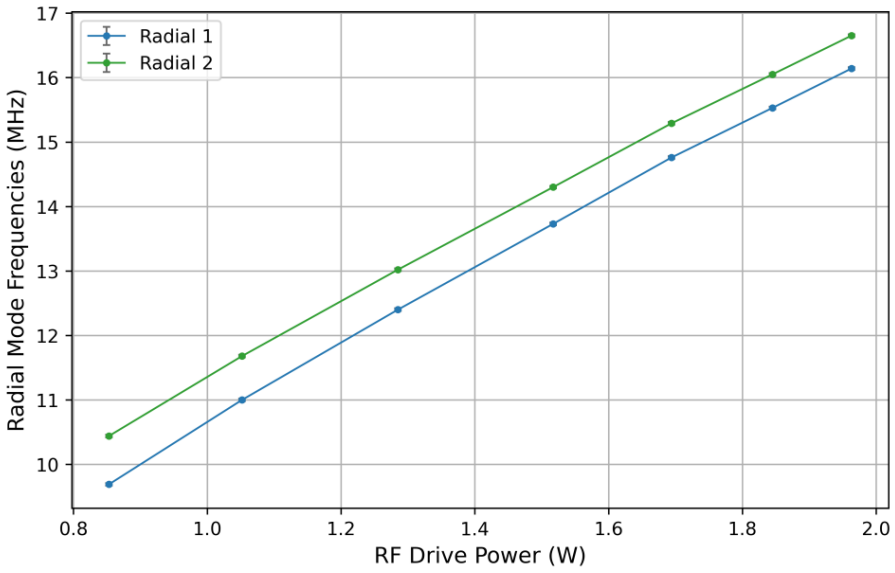

Figure 7.2: Radial secular mode frequencies for a single $^9Be^+$ ion versus RF drive power (on the antenna) up to 2 W. Non-degenerate frequencies are obtained by applying a different DC bias to the two radial electrode sets, in this case -75 and -77V. The axial confinement was fixed for these tests, with mode frequency of 3.64 MHz. To achieve a clean recoil-free spectrum it would be ideal to push the mode frequencies up to around 40 MHz, well resolved from the 20 MHz natural linewidth.

With the current 2W amplifier (Mini-Circuits ZHL-1-2W-S+) we can only reach about 16 MHz radial mode frequencies. This would help reduce the Lamb-Dicke parameters and

Table 7.1: Measured RF power available at the loop antenna as a function of power output at the Siglent function generator. The required vertical compensation voltage at different settings, for minimum micromotion parallel to the σ^- detection beam, is also listed. The final column lists the resulting measured radial secular mode frequencies of a single $^9Be^+$ ion.

Input (dBm)	Output (dBm)	Output (Watts)	V. Comp.	Mode Freqs. (MHz)
6.2	32.93	1.963	-9 x 20	16.14 , 16.65
5.2	32.66	1.845		15.53 , 16.05
4.2	32.29	1.694		14.76 , 15.29
3.2	31.81	1.517	-9 x 20	13.73 , 14.30
2.2	31.09	1.285		12.40 , 13.02
1.2	30.22	1.052	-8 x 20	11.00 , 11.68
0.2	29.31	0.853	-7 x 20	9.69 , 10.44
-0.8	28.34	0.682	-7 x 20	
-1.8	27.39	0.548		
-2.8	26.39	0.436		
-3.8	25.39	0.346	-6.5 x 20	
-4.8	24.39	0.275		
-5.8	23.41	0.219		
-6.8	22.41	0.174	-6.5 x 20	
-7.8	21.13	0.139		

slow the heating rates during spectroscopy pulses, however the recoil shift model suggested we would need to increase all of the mode frequencies to approximately 40 MHz to reduce the recoil shift correction to the few kHz level. It might be possible to or increase the mode frequencies to $\approx$ 20 MHz and fit a multi-component spectrum to achieve accuracy at the few kHz level, but this was not investigated. We estimate that with an axial secular mode frequency of 12 MHz, and radial mode frequencies of 16.14 MHz and 16.65 MHz there would still be approximately a 90 kHz photon recoil shift correction that would need to be characterized, compared to the 180 kHz shift reported above [45].

7.2 Axial and Radial Heating Rates

Heating of the ion from rf noise can occur from injected noise on the end caps or electrodes, or as "anomalous" heating, thought to be associated with electric field noise due to fluctuating patch potentials on electrode surfaces [76, 77]. Characterizing the electric

field noise motional heating rates was not critical for any of the strong transition measurements, but is important to understand for planned experiments that involve quantum-logic spectroscopy.

The temperature of the ion can be measured by comparing the relative amplitude of the red and blue sidebands at the secular mode frequencies, using resolved Raman sideband spectroscopy [31, 76]. In the limit that the motional state population is prepared in the the $n = 0$ ground state, the red sideband amplitude tends to zero. Note that for Raman sideband spectroscopy, the polarization and wavevector orientations of the two beams need to be set appropriately to address axial and radial motional modes. The heating can then be measured by applying a variable delay between the Doppler cooling sequence and measurement of the ion temperature. This was done separately for all three modes. After reducing several sources of injected technical noise, the heating rates were measured with results summarized in Table 7.2.

Table 7.2: Heating rates for each axis after Doppler cooling to the measured initial mode occupation number, $\bar{n}$.

Axis	Initial $\bar{n}$	Heating Rate (quanta/s)
Axial	2.44	35.1
Radial 1	1.09	3.4
Radial 2	0.95	3.75

7.3 Operation at Magnetic Fields up to 10 Gauss

The majority of measurements were performed at a bias field of 0.895 mG with the $^2P_{3/2}$ hyperfine splittings measured at a bias field of 0.1343 mG. We had also considered the possibility that moving to higher magnetic field might allow us to resolve particular excited state hyperfine components, so we added a second set of coils on the quantization axis. These were driven first with a BK Precision current/voltage controller and later with a more precise Agilent controller. Since the second set of coils was totally separate, we could still use the

feedback mechanism on the first set to stabilize the field and run all the experiments from previous chapters, including the clock probe on the ground state hyperfine splittings. A plot of the measured magnetic field as a function of applied current is shown in Figure 7.3.

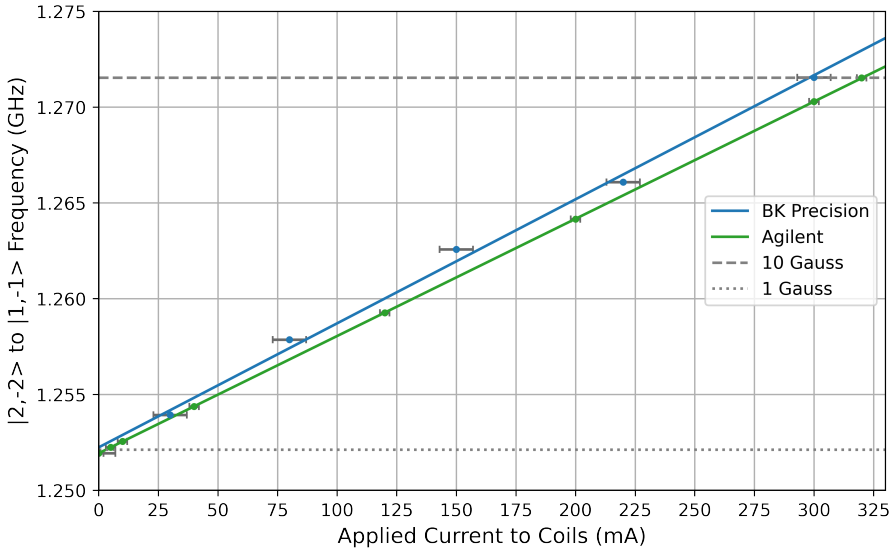

Figure 7.3: The measured transition frequency of the $|^2S_{1/2}, 2, -2\rangle$ to $|^2S_{1/2}, 1, -1\rangle$ transition versus applied current to the coils. The covered range is approximately 1 to 10 Gauss, with corresponding dotted and dashed lines shown in the plot.

7.4 Laser Ablation Loading Conditions for Be^+ and Ca^+

Beryllium ions are loaded into the wheel trap via pulsed laser ablation of a 0.25 mm diameter beryllium wire (Goodfellow BE005115, 99.7 %), mounted on the back of the far endcap. Loading from $BeCl_2$ salts has been demonstrated, and is described in a later section. Loading of Ca^+ with no photoionization from a 10 % concentration calcium aluminum alloy has been demonstrated as well, using the same trap under similar conditions. The primary difference is an IR repump laser operating at $\lambda = 866$ nm is required to prevent accumulation of population in the metastable $D_{3/2}$ state.

The ablation laser (CrystalLaser QL523-500) beam is first expanded by roughly a factor of 3 with a basic two lens Galilean beam expander. The maximum pulse energy delivered

from the laser is 200 μJ, at a wavelength of 523 nm with a pulse duration of 10 ns. The power is attenuated using a half waveplate and polarizing beamsplitter cube, typically to about half of maximum available output power of the laser. The ablation beam is steered though a hole in the front endcap and center of the trap and is focused onto the target with an 80 mm focal length plano-convex lens. The estimated beam radius is 12 μm when focused on the wire. The repetition rate of the laser can be reduced to 100 Hz using the internal trigger of the laser controller, or can be adjusted down further for single shot loading using an external TTL control signal. Adjusting the ablation pulse energy and trap radial confinement determines whether hot clouds or individual ions are loaded. In general, lower radial confinement leads to loading of larger clouds while single ions are more commonly loaded with higher radial confinement. The approximate conditions for each case are summarized in Table 7.3. An additional table is included for when we loaded the same trap with Calcium ions Table 7.4. When locating the first ion cloud it is easier to load and look for a large cloud while fine-tuning the far-detuned beam alignment. Once the alignment and other trap parameters are optimized, we then adjust to load single ions. It is unclear whether the near-detuned cooling beam plays a significant role in loading, or whether it is just helpful for greater fluorescence contrast when the cloud crystallizes.

Table 7.3: Approximate parameters used for loading both large beryllium ion clouds and few- or single-ion crystals. The numbers are not meant to imply what is required or optimal, but rather what was typical and successful within our usage. The near detuned cooling is mostly helpful to see greater fluorescence upon crystallization of the ion cloud. Once the cloud crystallizes, the far detuned beam power needs to be attenuated to observe the strongest fluorescence. For reference, the 15 V_{pp} RF voltage on the antenna corresponds to radial secular mode frequencies of about 10 MHz, or about $\pm$150 V_{pp} at the trap. The axial secular mode frequency for a single $^9Be^+$ ion at +80V relative potential on the endcaps is about 3.6 MHz.

Parameter	Load Cloud	Load Single	Observe Single	Unit
Applied RF Voltage (Antenna, 80 MHz)	$\leq$10	$\geq$15	$\geq$15	V_{pp}
Axial Confinement Voltage	20	80	80	V
Far Detuned Cooling (-415 MHz)	0.1-5	0.1-5	$<$0.1	mW
Near Detuned Cooling (-10 MHz)	N/A	N/A	1	μW
Ablation	$\approx$140	$\approx$140		μJ
Magnetic Field	0.1-10	0.1-10	0.1-10	G

Table 7.4: Approximate parameters used for loading $^{40}Ca^{+}$. Near detuned cooling is helpful to see greater fluorescence upon crystallization of the ion cloud. Once the cloud crystallizes, the far detuned and IR repump beam power need to be attenuated to observe the strongest fluorescence. The mode frequencies at the high end of the confinement range for a single $^{40}Ca^{+}$ ion were 2.8 MHz (axial) and 3.5 MHz (radial).

Parameter	Load Cloud	Load Single	Observe Single	Unit
Applied RF Voltage (Antenna, 71 MHz)	≈10	15-35	15-35	V_{pp}
Axial Confinement Voltage	20	80-250	80-250	V
Far Detuned Cooling (-210 MHz)	1-5	1-5	<0.1	mW
Near Detuned Cooling (-10 MHz)	N/A	N/A	1	μW
IR Repump (Resonant)	2.5	2.5	0.025	mW
Ablation	≈100	≈50		μJ
Magnetic Field	>0.5	>0.5	>0.5	G

A magnetic field to set the quantization axis is important for achieving the highest cycling rate on the $^{2}P_{3/2}$ closed-cycling transition. We typically use a field of about 1 Gauss and tune the σ^{-} polarization carefully (far- and near-detuned beams share the same polarization). For loading of Ca^{+} ions, a field of approximately 0.5 Gauss or higher was helpful and fluorescence decreased at lower values (which may be more related to destabilization of dark resonances). Images showing the initial cloud and later optimization to trap single ions is shown in Figure 7.4.

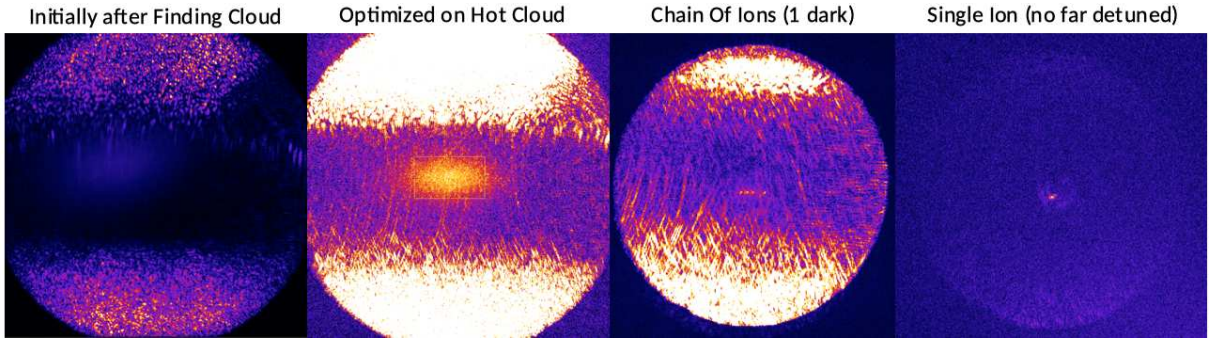

Figure 7.4: A sequence of images showing the first calcium cloud, followed by optimization of the lasers and loading parameters to trap a single $^{40}Ca^{+}$ ion.

Chapter 8

Ion Trap for Radioactive Isotopes $^{7,10}Be^{+}$

8.1 Introduction

One of the primary motivations for the work presented here is the study of few-electron ions for tests of QED. In particular, the techniques developed here for precision measurements in $^{9}Be^{+}$ can be applied to the study of $^{7,10}Be^{+}$ to investigate the many-body QED corrections to the predicted energy levels in Li-like ions. By comparing of the ^{2}P fine structure splitting for each rare isotope with that of $^{9}Be^{+}$, it is possible to extract the isotope shift of the fine structure splitting; the so-called "splitting isotope shift" (SIS) [2, 7, 55]. Since the relativistic corrections to the calculations of the ^{2}P fine structure are common to all isotopes of a given element, a measurement of the SIS makes it possible to isolate the many-body QED contribution to the theory. The theoretical uncertainty in the SIS is typically of the order of a few kHz and therefore provides an opportunity for comparison with high-precision measurements [15, 45]. In addition, it is possible to extract the relative nuclear charge radii of rare isotopes of beryllium using spectroscopic measurements. The mass shift contribution, due to the different nuclear mass of each isotope, can be calculated and subtracted off. The remaining shift is dominated by the field shift, or in other words the difference in the effective radius of the nuclear charge distribution.

Since isotopes 7 and 10 have reasonably long half-lives of 53 days and 1.4×10^{6} years, respectively, these could potentially be trapped and studied in our apparatus to yield improved experimental results. The following sections describe the details related to the study of these isotopes in a duplicate rf Paul trap with slight modifications, starting from procurement of samples dissolved in HCl.

8.2 Rare Isotope Sample Procurement

^{7}Be was ordered in aqueous form in 0.5-5.0 N HCl at a concentration of about 1mCi/mL. This is available directly from the National Isotope Development Center (NIDC), and is produced from time to time in an accelerator facility. To minimize ionizing radiation hazards, we chose to limit our total ^{7}Be sample to 1 μCi of activity. We note that it is possible that we will encounter difficulty when trying to load the trap using such a low initial total number of atoms, $N_0 = 2.5 \times 10^{11}$. For reference, this atom number is roughly 10^5 times lower than in previously published work on loading $^{133}Ba^{+}$ from 1 mCi samples of radioactive barium [78].

A fixed ratio aqueous solution of ^{9}Be and ^{10}Be was previously sold from NIST for use as a calibration sample for ^{10}Be dating. This was discontinued some years ago, but we were able to arrange to obtain one of the remaining sample vials. The sample vials are provided as 5 g of 73.35 Bq ^{10}Be/g, 57 μg Be/g, 1M HCl from the radioactivity group at the National Institute of Standards and Technology (NIST) in Gaithersburg, MD. It is a mixture containing mostly the stable isotope ^{9}Be with a partial fraction of ^{10}Be. The total activity for 5 g is

$$73.35 \text{ Bq/g} \times 5\text{g} = 366.75\text{Bq} = 10 \text{ nCi},$$

thus deposition of the full solution volume would result in at most 10 nCi of ^{10}Be. We plan to start with just 1 nCi. This is a small activity but a relatively large initial number of ^{10}Be atoms, $N_0 = 2.3 \times 10^{16}$.

8.3 Radioactivity Analysis

^{7}Be has a half-life of 53.22 days and decays only through electron capture.

$$^{7}_{4}\text{Be} + e^{-} \rightarrow ^{7}_{3}\text{ Li} + \nu_e.$$

The total decay energy is 861.8 keV, which is primarily transferred to the electron neutrino. In 10.44 % of decays, the lithium nucleus ends in an excited state which then decays with emission of a 477.6 keV gamma ray.

^{10}Be has a half-life of 1.51×10^6 years and decays through beta decay (β^-) to Boron, an electron, and an anti-neutrino.

$$^{10}_{4}\mathrm{Be} \rightarrow ^{10}_{5}\mathrm{B} + e^- + \nu^-.$$

The total decay energy is 556 keV, which is split on average about 50/50 between the electron and anti-neutrino. The relevant radiation concern is the 275 keV electron from each decay. We estimate that this electron will typically collide with a solid structure within the trap or with the walls of the chamber produce Bremsstrahlung radiation at a significantly reduced energy depending on the particular material.

8.4 Endcap and Ablation Target Design

The trap endcaps were redesigned with slots to allow for interchangeable target holders, which can be accessed by removing the top spectroscopy chamber window. A diagram indicating the target mounting location is shown in Figure 8.1. A 250 μm ^{9}Be wire is also mounted within the field of view of the ablation laser, fixed in a narrow slot on the endcap.

8.5 Deposition of Samples on the Target

Both ^{7}Be and ^{10}Be are available as aqueous solutions in HCl, which can be evaporated using a hot plate in a fume hood to deposit chloride salts on the target. The process follows previous descriptions of $BaCl_2$ target preparation [78, 79]. We have tested a modified version of the procedure using ^{9}Be dissolved in HCl. Since the volume of the hole on the target is only a few μL, it was necessary to first concentrate the samples and then transfer via micro-pipette after reaching a small enough total volume. To concentrate the samples, vials with

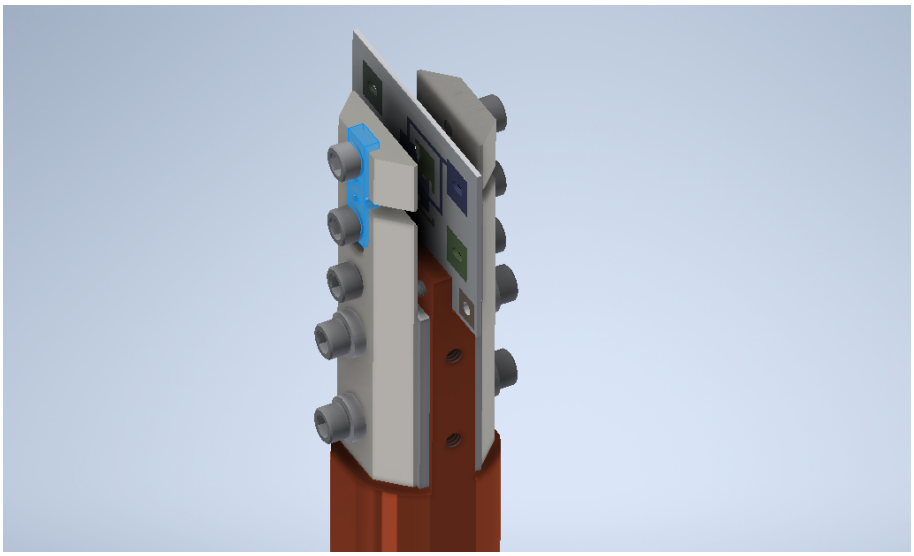

Figure 8.1: An interchangeable ablation target (blue) is shown mounted in a modified endcap designed for it. The ablation target has a 1 mm diameter, 1mm depth hole on the inner surface which contains the deposited $^{7,10}BeCl_2$ samples.

an internal conical shape were used for initial evaporation (Wheaton borosilicate graduated V-vial, 0.5 mL). Micropipetting was done using an adjustable pipette (Accumax 0.1-2.5 μL) with universal micropipette tips (LabGenius non-filtered, 10 μL). To reduce any proportion of ions which remain in the vials or pipette tips on surface sites, glassware and tips were first rinsed with prepared aqueous ^{9}Be HCl solution.

After some testing of parameters using a prepared ^{9}Be HCl solution, it was determined that the samples could be concentrated 100 μL at a time by heating in the borosilicate V-vial in an aluminum holder on a hot plate at about 90° C. Gentle air flow helps increases the evaporation rate. The samples were allowed to fully evaporate between steps, and finally re-dissolved with about 5 μL distilled water and moved with micropipette to the hole on the (cold) target. Depositing a non-acidic sample in the final step reduced etching of the titanium. The target, still on the custom built holder, was allowed to heat to 160° C and given ample time to fully evaporate the liquid to leave the salt residue. The total mass of beryllium deposited on the target in the initial test was about 90 μg. An image of the V-vial during the concentration process, target holder block and the final resulting chloride salt deposition for the ^{9}Be test are shown in Figure 8.2.

Figure 8.2: From left to right in the image. Borosilicate V-Vial used to concentrate the samples, heating and concentration at 90C in aluminum holder, micropipetting into cold target on custom holder, and residual $^{9}BeCl_2$ salts after final heating and evaporation at 160C. Images are from the testing phase prior to work with the rare isotopes.

8.6 Imaging of the Ablation Laser Focus

One of the challenges of ablating from the target was simply making sure the ablation beam was properly focused and aligned on either the Be wire or the $BeCl_2$ salts. In the previous version of the trap with only the Be wire, it was possible to measure the transmitted ablation laser power as it was swept across the wire to determine the focus spot size and beam location. Since the salts were deposited from liquid onto the target, no through beam hole could be easily added. Instead, an on-axis imaging system for the ablation beam based around a USB microsope (Plugable USB2-MICRO-250X) and a silver mirror (Thorlabs ME1-P01) mounted at 45° with a central hole drilled through using a diamond bit was built. Note that it was later found it is possible to buy silver mirrors on a molybdenum substrate, which is easier to machine the hole into. A diagram of the ablation laser imaging setup and images with the laser focused on the Be wire and beryllium chloride salts is shown in Figure 8.3. This was successful in imaging the reflected light from the ablation beam on the target, despite having to image through the center of the trap. Diffuse white light is also input from one of the other back side spectroscopy chamber apertures to illuminate the target and endcaps to identify the features in the image. On-axis white light from the microscope itself is available, though it was typically turned off to avoid reflection artifacts which tend

to obscure the image. The camera sensitivity is reasonably high, so the ablation laser was almost completely attenuated for alignment then turned up for actual ablation (with the camera blocked or removed to avoid damaging the sensor).

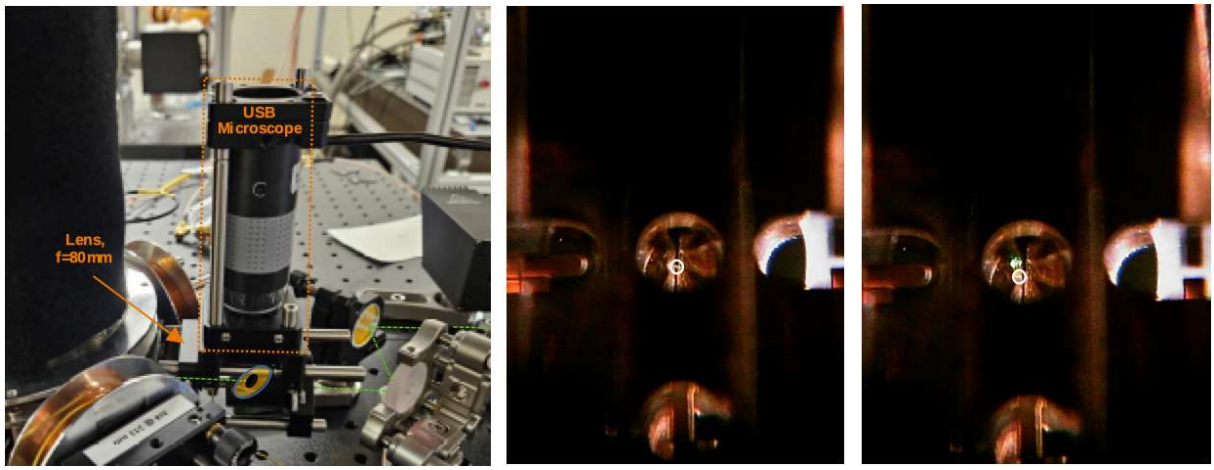

Figure 8.3: A diagram of the USB microscope and collection setup used to both align and focus the ablation laser while imaging is shown on the left. Sample images looking through the center of the trap with the ablation laser focused on the wire(center) and chloride salts(right) are also shown. A white circle highlights the location of the focus spot to help distinguish from other scatter artifacts which can also sometimes be observed.

8.7 Test of Ion Trap Loading from $^{9}BeCl_2$ Salts

The trap was first optimized after loading from the beryllium wire. The ablation beam was focused to a calculated waist radius of roughly 12 μm with initial power set at about 75 % of the maximum possible 200 μJ pulse energy from a 523 nm, 10 ns pulsed laser (CrystalLaser QL523-500). Ablation pulses at 100 Hz repetition rate are delivered for a fraction of a second. The pulse energy density corresponds to approximately 35 J/cm^2, far into the regime where both ions and neutrals should be generated. After the magnetic field, far-detuned and resonant laser beam alignment and polarization were well optimized, the ablation beam was steered to the chloride salts. The loading from salts was successful immediately, and required only about half the ablation pulse energy. The trap was loaded

repeatedly from the same spot location hundreds of times over the first few days with no significant decrease in performance, and has continued to be able to load as needed. Single shot loading via external TTL control was also successful with the same general configuration.

8.8 Magnetic Field Coils

Helmholz-like coils for all three axes were assembled to null the two off-quantization-axis fields and generate the $0.1 - 1$ Gauss quantization axis field. The spacing for the vertical axis is close to the Helmholz condition of the coil radius equal to the coil spacing. On the horizontal axes there is insufficient space to put larger radius coils so the field is not quite as uniform. A plot of the simulated and measured magnetic fields for the vertical (large coils) and horizontal (small coils) at a drive current of 100 mA is shown in Figure 8.4.

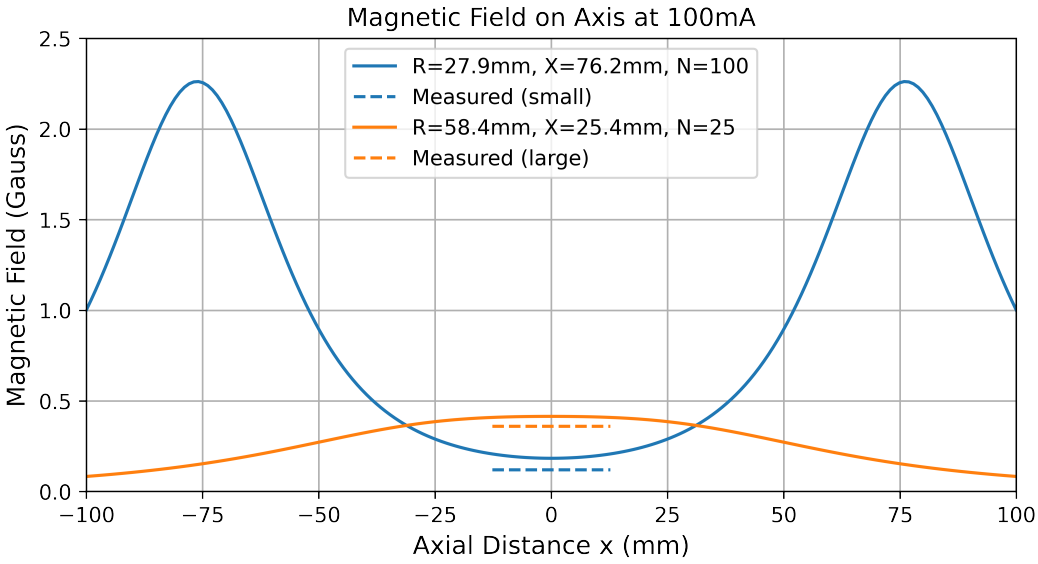

Figure 8.4: Calculated magnetic field on axis for the horizontal (blue) and vertical coils (orange) at a drive current of 100 mA. Measured values are shown as dashed lines for each, measured at 500mA then divided by 5. The Gaussmeter resolution was limited to about 0.1 Gauss with some random fluctuations, so it could not resolve the fine field variations across a 25mm translation stage range at 500mA drive current.

The quantization axis field is controlled with a precision laser diode controller (Thorlabs LDC500), which has a compliance voltage of < 4 V and maximum current of 500 mA. The wire gauge (26) and number of loops (100) was chosen to give approximately 8 Ω total resistance to maximize the available range and allow fine tuning for 0.1 mA steps in the manual control. The vertical axis uses coils with 25 loops each and 26 gauge wire.

The magnetic field was measured for both the small and large coil sets. The measured field was slightly lower than the model in both cases. The coil strengths on axis near the center are 1.2 and 3.6 G/A for the small and large coil sets (when not attached to the chamber), respectively.

Chapter 9

Conclusions and Outlook

9.1 Summary of Work and Impact

In summary, precision measurements on simple atoms and ions can be used for a wide variety of studies including tests of QED and measurements of nuclear structure. The work presented here led to the development high-precision techniques for measurements of strong transitions using single trapped ions, and explored the limiting systematic uncertainties in such cases. The precise state control available when using a single laser-cooled $^9Be^+$ ion led to improved measurement of all of the first excited state energy level structure, reducing the absolute uncertainties to 50-80 kHz.

The absolute frequency measurements of the D-lines in $^9Be^+$ are now the most accurate, to date, of any such ion-trap-based measurements of a broad dipole-allowed transition, with a relative uncertainty of $\Delta\nu/\nu = 5 \times 10^{-11}$ and line splitting of approximately one part in 400. This accuracy was enabled by the careful characterization of photon recoil and by conducting measurements in a regime which produces lineshapes closely approaching the fundamental Lorentzian limit. By carefully considering the role of quantum interference, we have been able to extend these measurement techniques to resolving the $^2P_{3/2}$ hyperfine structure and to provide the first direct experimental measurement of the splittings. The microwave Ramsey spectroscopy measurement of the ground state hyperfine splitting is in good agreement with the high-field Penning trap measurements from NIST, with comparable accuracy. This measurement demonstrated a technique which can be applied to future measurements of $^7Be^+$ at low applied magnetic field. Finally, extraction of the ^2P lifetimes using the D_2 lineshape data yielded an improved result compared to previous experimental values and is in good agreement with recent theory prediction [21]. A summary of all the completed measurements is shown in Figure 9.1.

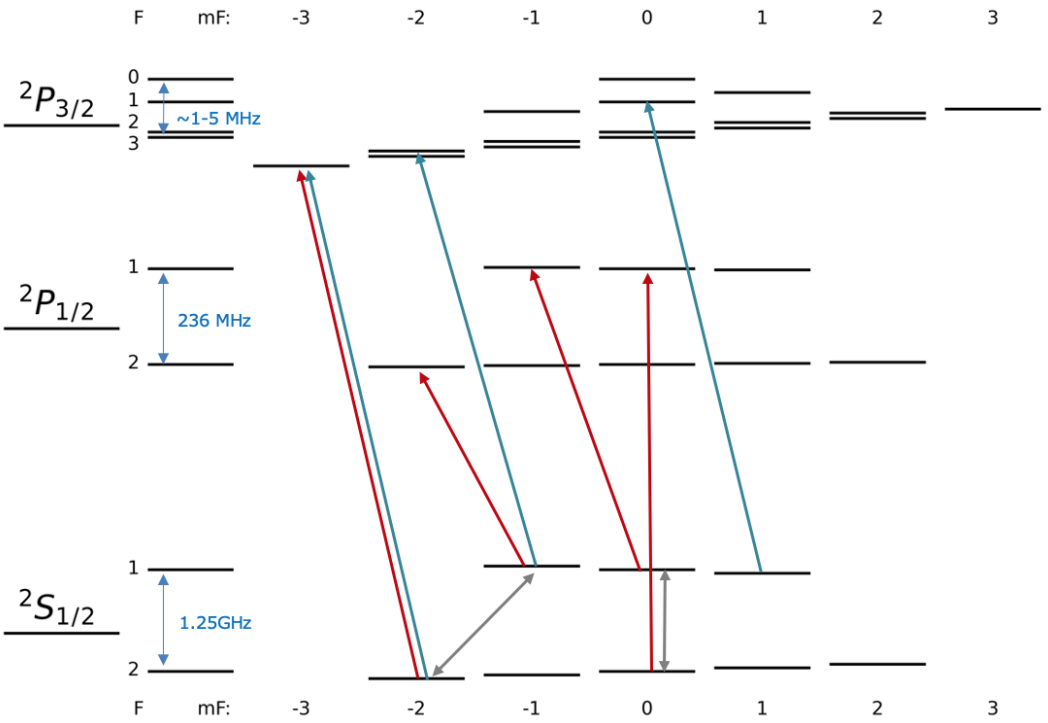

Figure 9.1: A summary of the completed measurements are shown in the figure. In red are shown the four absolute frequency measurements of the D-lines in $^9Be^+$, which reduced the uncertainty in these transitions from the single MHz level to about 50 kHz [45]. The fine structure splitting and $^2P_{1/2}$ hyperfine constant were also extracted. In blue are shown the relative measurements to $^2P_{3/2}$ F=3,2,1 used to extract the hyperfine coefficients for comparison to theory [60]. In grey are shown the microwave transitions which were used for a 1.6×10^{-11} relative uncertainty measurement of the ground state hyperfine splitting.

9.2 Outlook

The techniques utilized within this work and the characterizations of systematic effects are applicable not just to $^9Be^+$, but generally to other trapped ion systems. The details for other experiments will vary depending on the nuclear spin, excited-state structure and level of confinement in the trap, but the general framework can be adapted. Measurement of fine and hyperfine structure by such means is a promising avenue by which to extract subtle nuclear structure or test atomic structure calculations. Prior to this work, $^9Be^+$ had already been widely used and studied for over 40 years, but there still remained so much further fine detail that could be explored experimentally. This suggests that similar measurements of other species using single trapped ions might also prove fruitful. For example, although nuclear

magnetic octupole moments have already been extracted in heavy alkali atoms ^{133}Cs [9, 10] and ^{87}Rb [11], and in alkali-like ion $^{137}Ba^{+}$ [80,81], precise measurements using the techniques presented in this work might enable sufficient resolution for extraction of the more subtle effects in lighter species as well.

A particular technical development that may be applicable in other systems is the experimental control and lineshape modeling used to resolve the otherwise-unresolved $^{2}P_{3/2}$ hyperfine structure. This technique is referred to as quantum-interference-enhanced state-selective repump spectroscopy [60]. While a wide variety of other methods exist to measure hyperfine structure, most are inherently limited to a resolution that is comparable to the natural linewidth of the transition.

Experiments using the rare isotopes $^{7,10}Be^{+}$ are currently under development. A new ion trap and vacuum system have been constructed and $^{9}Be^{+}$ ions have been loaded from a $BeCl_2$ target. All of the necessary measurement infrastructure and techniques have been established for precision experiments with $^{7,10}Be^{+}$. A measurement of the fine-structure splitting in these rare isotopes will enable a stringent test on many-body QED in three electron systems and a more precise extraction of the relative nuclear charge radii. Measurement of the $^{7}Be^{+}$ ground state hyperfine splitting in the ion trap is expected to improve on the current best result by four orders of magnitude and allow an improved determination of the nuclear Zemach radius. Measurement of the excited state hyperfine splitting will allow improved understanding of the ^{7}Be nuclear magnetic dipole and electric quadrupole moments and comparison to theoretical calculations of the hyperfine coefficients, similar to what was achieved in this work for $^{9}Be^{+}$. Further developments in loading efficiency might prove necessary, for example by implementing photoionization or by dynamic adjustment of trap potentials during ablation. This could lead to helpful insight in other ion-trap experiments which seek to load single ions or small crystals of rare atomic species.

Precise measurement of strong transitions in ion traps presents unique challenges, but also the opportunity to gain insight about an ion's nuclear structure and to test QED theory

predictions. With the well-controlled conditions and state preparation present for a single Doppler-cooled ion, it is possible to extract spectra approaching the fundamental Lorentzian limit and to observe and utilize interesting effects such as quantum interference. Photon recoil heating is inevitably a challenge, but is able to be controlled and modeled sufficiently, even in the intermediate confinement regime. Different ion species may in fact prove easier to deal with than beryllium, as the photon recoil is relatively large for the low mass Be^+ ion and large momentum 313 nm photon. In the future, it could be possible to improve the accuracy of measurements in Li-like ions by, for instance, increasing the trapping confinement or employing quantum-enabled spectroscopy techniques such as quantum-logic spectroscopy or photon recoil spectroscopy.

Bibliography

[1] M. S. Safronova, D. Budker, D. DeMille, Derek F. Jackson Kimball, A. Derevianko, and Charles W. Clark. Search for new physics with atoms and molecules. *Rev. Mod. Phys.*, 90:025008, Jun 2018.

[2] Zong-Chao Yan and G. W. F. Drake. Lithium isotope shifts as a measure of nuclear size. *Phys. Rev. A*, 61:022504, Jan 2000.

[3] Mariusz Puchalski and Krzysztof Pachucki. Fine and hyperfine splitting of the $2p$ state in li and be$^+$. *Phys. Rev. A*, 79:032510, Mar 2009.

[4] Mariusz Puchalski and Krzysztof Pachucki. Quantum electrodynamics $m\alpha^6$ and $m\alpha^7 ln\alpha$ corrections to the fine splitting in li and be$^+$. *Phys. Rev. A*, 92:012513, Jul 2015.

[5] Aldo Antognini, Franziska Hagelstein, and Vladimir Pascalutsa. The proton structure in and out of muonic hydrogen. *Annual Review of Nuclear and Particle Science*, 72(1):389–418, 2022.

[6] Roger C. Brown, Saijun Wu, J. V. Porto, Craig J. Sansonetti, C. E. Simien, Samuel M. Brewer, Joseph N. Tan, and J. D. Gillaspy. Quantum interference and light polarization effects in unresolvable atomic lines: Application to a precise measurement of the ^{6,7}li D_2 lines. *Phys. Rev. A*, 87:032504, Mar 2013.

[7] W. Nörtershäuser, D. Tiedemann, M. Žáková, Z. Andjelkovic, K. Blaum, M. L. Bissell, R. Cazan, G. W. F. Drake, Ch. Geppert, M. Kowalska, J. Krämer, A. Krieger, R. Neugart, R. Sánchez, F. Schmidt-Kaler, Z.-C. Yan, D. T. Yordanov, and C. Zimmermann. Nuclear charge radii of ^{7,9,10}Be and the one-neutron halo nucleus ^{11}Be. *Phys. Rev. Lett.*, 102:062503, Feb 2009.

[8] E. Arimondo, M. Inguscio, and P. Violino. Experimental determinations of the hyperfine structure in the alkali atoms. *Rev. Mod. Phys.*, 49:31–75, Jan 1977.

[9] Vladislav Gerginov, Andrei Derevianko, and Carol E. Tanner. Observation of the nuclear magnetic octupole moment of ^{133}Cs. *Phys. Rev. Lett.*, 91:072501, Aug 2003.

[10] Dipankar Das and Vasant Natarajan. High-precision measurement of hyperfine structure in the d lines of alkali atoms. *Journal of Physics B: Atomic, Molecular and Optical Physics*, 41(3):035001, jan 2008.

[11] Vladislav Gerginov, Carol E Tanner, and W.R Johnson. Observation of the nuclear magnetic octupole moment of [sup.87]rb from spectroscopic measurements of hyperfine intervals. *Canadian journal of physics*, 87(1):101–, 2009.

[12] D. J. Wineland, J. J. Bollinger, and Wayne M. Itano. Laser-fluorescence mass spectroscopy. *Phys. Rev. Lett.*, 50:628–631, Feb 1983.

[13] J. J. Bollinger, J. S. Wells, D. J. Wineland, and Wayne M. Itano. Hyperfine structure of the $2p^2p_{\frac{1}{2}}$ state in ^{9}Be$^+$. *Phys. Rev. A*, 31:2711–2714, Apr 1985.

[14] T. Nakamura, M. Wada, K. Okada, A. Takamine, Y. Ishida, Y. Yamazaki, T. Kambara, Y. Kanai, T. M. Kojima, Y. Nakai, N. Oshima, A. Yoshida, T. Kubo, S. Ohtani, K. Noda, I. Katayama, V. Lioubimov, H. Wollnik, V. Varentsov, and H. A. Schuessler. Laser spectroscopy of ^{7,10}Be$^+$ in an online ion trap. *Phys. Rev. A*, 74:052503, Nov 2006.

[15] Wilfried Nörtershäuser, Christopher Geppert, Andreas Krieger, Krzysztof Pachucki, Mariusz Puchalski, Klaus Blaum, Mark L. Bissell, Nadja Frömmgen, Michael Hammen, Magdalena Kowalska, Jörg Krämer, Kim Kreim, Rainer Neugart, Gerda Neyens, Rodolfo Sánchez, and Deyan T. Yordanov. Precision test of many-body qed in the be$^+$ $2p$ fine structure doublet using short-lived isotopes. *Phys. Rev. Lett.*, 115:033002, Jul 2015.

[16] D. J. Wineland, C. Monroe, W. M. Itano, D. Leibfried, B. E. King, and D. M. Meekhof. Experiment issues in coherent quantum-state manipulation of trapped atomic ions. *J. Res. Natl. Inst. Stand. Technol.*, 103:259, 1998.

[17] J. P. Gaebler, T. R. Tan, Y. Lin, Y. Wan, R. Bowler, A. C. Keith, S. Glancy, K. Coakley, E. Knill, D. Leibfried, and D. J. Wineland. High-fidelity universal gate set for $^{9}Be^{+}$ ion qubits. *Phys. Rev. Lett*, 117:060505, 2016.

[18] T. Rosenband et al. Frequency ratio of al^{+} and hg^{+} single-ion optical clocks; metrology at the 17th decimal place. *Science*, 319:1808, 2008.

[19] S. A. King, L. J. Spieß, P. Micke, A. Wilzewski, T. Leopold, E. Benkler, R. Lange, N. Huntemann, A. Surzhykov, V. A. Yerokhin, J. R. Crespo López-Urrutia, and P. O. Schmidt. An optical atomic clock based on a highly charged ion. *Nature*, 611:43, 2022.

[20] T. Andersen, K. A. Jessen, and G. Sørensen. Mean-life measurements of excited electronic states in neutral and ionic species of beryllium and boron. *Phys. Rev.*, 188:76–81, Dec 1969.

[21] U. I. Safronova and M. S. Safronova. Relativistic many-body calculation of energies, lifetimes, polarizabilities, and hyperpolarizabilities in li-like be^{+}. *Phys. Rev. A*, 87:032502, Mar 2013.

[22] V. A. Yerokhin. Hyperfine structure of li and be. *Phys. Rev. A*, 78:012513, Jul 2008.

[23] O Poulsen, T Andersen, and N J Skouboe. Fast-beam, zero-field level-crossing measurements of radiative lifetimes, fine and hyperfine structures in excited states of ionic and neutral beryllium. *Journal of Physics B: Atomic and Molecular Physics*, 8(9):1393, jun 1975.

[24] N. Shiga, W. M. Itano, and J. J. Bollinger. Diamagnetic correction to the $^{9}Be^{+}$ ground-state hyperfine constant. *Phys. Rev. A*, 84:012510, 2011.

[25] J. J. Bollinger, D. J. Heinzen, Wayne M. Itano, S. L. Gilbert, and D. J. Wineland. Test of the linearity of quantum mechanics by rf spectroscopy of the $^{9}Be^{+}$ ground state. *Phys. Rev. Lett.*, 63:1031–1034, Sep 1989.

[26] K. Okada, M. Wada, T. Nakamura, A. Takamine, V. Lioubimov, P. Schury, Y. Ishida, T. Sonoda, M. Ogawa, Y. Yamazaki, Y. Kanai, T. M. Kojima, A. Yoshida, T. Kubo, I. Katayama, S. Ohtani, H. Wollnik, and H. A. Schuessler. Precision measurement of the hyperfine structure of laser-cooled radioactive $^{7}Be^{+}$ ions produced by projectile fragmentation. *Phys. Rev. Lett.*, 101:212502, Nov 2008.

[27] S. M. Brewer, J.-S. Chen, A. M. Hankin, E. R. Clements, C. W. Chou, D. J. Wineland, D. B. Hume, and D. R. Leibrandt. $^{27}al^{+}$ quantum-logic clock with a systematic uncertainty below 10^{-18}. *Phys. Rev. Lett.*, 123:033201, Jul 2019.

[28] C. Monroe, D. M. Meekhof, B. E. King, S. R. Jefferts, W. M. Itano, D. J. Wineland, and P Gould. Resolved-sideband raman cooling of a bound atom to the 3d zero-point energy. *Phys. Rev. Lett.*, 75:4011, 1995.

[29] W. M Itano and D. J. Wineland. Laser cooling of ions stored in harmonic and penning traps. *Phys. Rev. A*, 25:35, 1982.

[30] J.-S. Chen, S. M. Brewer, C. W. Chou, D. J. Wineland, D. R. Leibrandt, and D. B. Hume. Sympathetic ground state cooling and time-dilation shifts in an $^{27}Al^{+}$ optical clock. *Phys. Rev. Lett.*, 118:053002, Jan 2017.

[31] D. Leibfried, R. Blatt, C. Monroe, and D. Wineland. Quantum dynamics of single trapped ions. *Rev. Mod. Phys*, 75:281–324, 2003.

[32] D. J. Berkeland, J. D. Miller, J. C. Bergquist, W. M. Itano, and D. J. Wineland. Minimization of ion micromotion in a paul trap. *J. Appl. Phys.*, 83:5025, 1998.

[33] Jwo-Sy Chen. *Ticking near the Zero-Point Energy: towards 1×10^{-18} Accuracy in Al^{+} Optical Clocks*. PhD thesis, University of Colorado, Boulder, 2017.

[34] G. D. Boyd and D. A. Kleinman. Parametric interaction of focused gaussian light beams. *J. Appl. Phys.*, 39:3597, 1968.

[35] Tim Freegarde, Julian Coutts, Jochen Walz, Dietrich Leibfried, and T. W. Hänsch. General analysis of type i second-harmonic generation with elliptical gaussian beams. *J. Opt. Soc. Am. B*, 14(8):2010–2016, Aug 1997.

[36] Joseph T. Verdeyen. *Laser Electronics*. Prentice Hall, 1995.

[37] Zakary N. Burkley. *High power deep-UV laser for improved and novel experiments on hydrogen*. PhD thesis, Colorado State University, 2019.

[38] A. Wilson et al. A 750-mw continuous-wave, solid-state laser source at 313 nm for cooling and manipulating trapped $^{9}be^{+}$ ions. *Appl. Phys. B*, 105:741, 2011.

[39] Travis C. Briles, Dylan C. Yost, Arman Cingöz, Jun Ye, and Thomas R. Schibli. Simple piezoelectric-actuated mirror with 180 khz servo bandwidth. *Opt. Express*, 18(10):9739–9746, May 2010.

[40] T. W. Hansch and B. Couillaud. Laser frequency stabilization by polarization spectroscopy of a reflecting reference cavity. *Optics Communications*, 35(3):441–444, December 1980.

[41] Y. Colombe, D. H. Slichter, A. C. Wilson, D. Leibfried, and D. J. Wineland. Single-mode optical fiber for high-power, low-loss uv transmission. *Opt. Express*, 22:19783–19793, 2014.

[42] Christian D. Marciniak, Harrison B. Ball, Alex T.-H. Hung, and Michael J. Biercuk. Towards fully commercial, uv-compatible fiber patch cords. *Opt. Express*, 25(14):15643–15661, Jul 2017.

[43] A. D. Brandt. *A new measurement of the $2S_{1/2} - 8D_{5/2}$ transition in atomic hydrogen*. PhD thesis, Colorado State University, 2021.

[44] A. D. Brandt, S. F. Cooper, C. Rasor, Z. Burkley, A. Matveev, and D. C. Yost. Measurement of the $2s_{1/2} - 8d_{5/2}$ transition in hydrogen. *Phys. Rev. Lett.*, 128:023001, 2022.

[45] D. M. Fairbank, A. L. Banducci, R. W. Gunkelman, J. B. VanArsdale, M. L. Vildibill, and S. M. Brewer. Absolute frequency measurements of the d lines in $^{9}be^{+}$ using a single trapped ion. *Phys. Rev. Lett.*, 131:093001, Sep 2023.

[46] Jürgen Eschner, Giovanna Morigi, Ferdinand Schmidt-Kaler, and Rainer Blatt. Laser cooling of trapped ions. *J. Opt. Soc. Am. B*, 20:1003–1015, 2003.

[47] Doppler broadening and lamb-dicke regime, 2018. www.thuliumlab.ru/blog/cold-atoms/dicke/.

[48] D. M. Meekhof, C. Monroe, B. E. King, W. M. Itano, and D. J. Wineland. Generation of nonclassical motional states of a trapped atom. *Phys. Rev. Lett.*, 76:1796–1799, Mar 1996.

[49] JC Bergquist, Wayne M Itano, and DJ Wineland. Recoilless optical absorption and doppler sidebands of a single trapped ion. *Physical Review A*, 36(1):428, 1987.

[50] Tetsuya Ido and Hidetoshi Katori. Recoil-free spectroscopy of neutral sr atoms in the lamb-dicke regime. *Phys. Rev. Lett.*, 91:053001, Jul 2003.

[51] Thomas Udem, Lothar Maisenbacher, Arthur Matveev, Vitaly Andreev, Alexey Grinin, Axel Beyer, Nikolai Kolachevsky, Randolf Pohl, Dylan C. Yost, and Theodor W. Hänsch. Quantum interference line shifts of broad dipole-allowed transitions. *Annalen der Physik*, 531(5):1900044, 2019.

[52] B H Bransden and C J Joachain. *Physics of Atoms and Molecules; 2nd ed.* Prentice-Hall, Harlow, 2003.

[53] Daniel Steck. *Quantum and Atom Optics*. 2022.

[54] R. Neugart, J. Billowes, M. L. Bissell, K. Blaum, B. Cheal, K. T. Flanagan, G. Neyens, W. Nörtershäuser, and D. T. Yordanov. Collinear laser spectroscopy at isolde: new methods and highlights. *Journal of Physics G: Nuclear and Particle Physics*, 44:064002, 2017.

[55] A. Krieger, W Nörtershäuser, Ch. Geppert, K. Blaum, M. L. Bissell, N. Frömmgen, M. Hammen, K. Kreim, M. Kowalska, J. Krämer, R. Neugart, G. Neyens, R. Sánchez, D. Tiedemann, D. T. Yordanov, and M. Zakova. Frequency-comb referenced collinear laser spectroscopy of be$^+$ for nuclear structure investigations and many-body qed tests. *Appl. Phys. B*, 123:15, 2017.

[56] M. Herrmann, V. Batteiger, S. Knünz, G. Saathoff, Th. Udem, and T. W. Hänsch. Frequency metrology on single trapped ions in the weak binding limit: The $3s_{1/2} - 3p_{3/2}$ transition in $^{24}Mg^+$. *Phys. Rev. Lett.*, 102:013006, Jan 2009.

[57] M. D. Barrett, B. DeMarco, T. Schaetz, V. Meyer, D. Leibfried, J. Britton, J. Chiaverini, W. M. Itano, B. Jelenković, J. D. Jost, C. Langer, T. Rosenband, and D. J. Wineland. Sympathetic cooling of $^9Be^+$ and $^{24}Mg^+$ for quantum logic. *Phys. Rev. A*, 68:042302, 2003.

[58] P. O. Schmidt et al. Spectroscopy using quantum logic. *Science*, 309:749–752, 2005.

[59] Y. Wan et al. Precision spectroscopy by photon-recoil signal amplification. *Nature Communications*, 5:3096, 2014.

[60] D. M. Fairbank, A. L. Banducci, R. W. Gunkelman, J. B. VanArsdale, and S. M. Brewer. Measurement of the unresolved $^9Be^+$ $^2p_{3/2}$ hyperfine splittings using quantum-interference-enhanced state-selective repump spectroscopy. *Phys. Rev. A*, 109:012809, Jan 2024.

[61] A. E. Dorokhov, A. A. Krutov, A. P. Martynenko, F. A. Martynenko, and O. S. Sukhorukova. Hyperfine structure of s states in muonic ions of lithium, beryllium, and boron. *Phys. Rev. A*, 98:042501, Oct 2018.

[62] Maria Allegrini, Ennio Arimondo, and Luis A. Orozco. Survey of hyperfine structure measurements in alkali atoms. *Journal of Physical and Chemical Reference Data*, 51(4):043102, 2022.

[63] K Pachucki, M. Puchalski, and V. A. Yerokhin. Regarding the $^9Be^+$ $^2P_{3/2}$ hyperfine B coefficient. private communication, 2023.

[64] Mariusz Puchalski, Jacek Komasa, and Krzysztof Pachucki. Hyperfine structure of the 2^3p state in ^{9}Be and the nuclear quadrupole moment. *Phys. Rev. Res.*, 3:013293, Mar 2021.

[65] K. Beloy, A. Derevianko, and W. R. Johnson. Hyperfine structure of the metastable $^3P_2$ state of alkaline-earth-metal atoms as an accurate probe of nuclear magnetic octupole moments. *Phys. Rev. A*, 77:012512, Jan 2008.

[66] K. Beloy and A. Derevianko. Second-order effects on the hyperfine structure of p states of alkali-metal atoms. *Phys. Rev. A*, 78:032519, Sep 2008.

[67] G. Clos, M. Enderlein, U. Warring, T. Schaetz, and D. Leibfried. Decoherence-assisted spectroscopy of a single mg^+ ion. *Phys. Rev. Lett.*, 112:113003, Mar 2014.

[68] R. Gerritsma, G. Kirchmair, F. Zähringer, J. Benhelm, R. Blatt, and C. F. Roos. Precision measurement of the branching fractions of the 4p 2p3/2 decay of ca ii. *The European Physical Journal D*, 50(1):13–19, 2008.

[69] M. Hettrich, T. Ruster, H. Kaufmann, C. F. Roos, C. T. Schmiegelow, F. Schmidt-Kaler, and U. G. Poschinger. Measurement of dipole matrix elements with a single trapped ion. *Phys. Rev. Lett.*, 115:143003, Oct 2015.

[70] Ziv Meir, Mudit Sinhal, Marianna S. Safronova, and Stefan Willitsch. Combining experiments and relativistic theory for establishing accurate radiative quantities in atoms: The lifetime of the $^2p_{3/2}$ state in $^{40}Ca^+$. *Phys. Rev. A*, 101:012509, Jan 2020.

[71] M. Fan, C. A. Holliman, A. Contractor, C. Zhang, S. F. Gebretsadken, and A. M. Jayich. Measurement of the ra$^+$ $7p\,^2P_{3/2}$ state lifetime. *Phys. Rev. A*, 105:042801, Apr 2022.

[72] Mariusz Puchalski and Krzysztof Pachucki. Ground-state hyperfine splitting in the be$^+$ ion. *Phys. Rev. A*, 89:032510, Mar 2014.

[73] S. M. Brewer, J.-S. Chen, K. Beloy, A. M. Hankin, E. R. Clements, C. W. Chou, W. F. McGrew, X. Zhang, R. J. Fasano, D. Nicolodi, H. Leopardi, T. M. Fortier, S. A. Diddams, A. D. Ludlow, D. J. Wineland, D. R. Leibrandt, and D. B. Hume. Measurements of $^{27}Al^+$ and $^{25}Mg^+$ magnetic constants for improved ion-clock accuracy. *Phys. Rev. A*, 100:013409, Jul 2019.

[74] W. M. Itano, J. C. Bergquist, J. J. Bollinger, J. M. Gilligan, D. J. Heinzen, F. L. Moore, M. G. Raizen, and D. J. Wineland. Quantum projection noise: Pupulation flucturation in two-level systems. *Phys. Rev. A*, 47:3554, 1993.

[75] A. V. Taichenachev, V. I. Yudin, C. W. Oates, Z. W. Barber, N. D. Lemke, A. D. Ludlow, U. Sterr, Ch. Lisdat, and F. Riehle. Compensation of field-induced frequency shifts in ramsey spectroscopy of optical clock transitions. *JETP Letters*, 90:713–717, 2010.

[76] M Brownnutt, M Kumph, P Rabl, and R Blatt. Ion-trap measurements of electric-field noise near surfaces. *Reviews of Modern Physics*, 87(4):1419, 2015.

[77] D. A. Hite, Y. Colombe, A. C. Wilson, K. R. Brown, U. Warring, R. Jördens, J. D. Jost, K. S. McKay, D. P. Pappas, D. Leibfried, and D. Wineland. 100-fold reduction of

electric-field noise in an ion trap cleaned with *In Situ* argon-ion-beam bombardment. *Phys. Rev. Lett.*, 109:103001, 2012.

[78] J. Christensen. *High-fidelity operation of a radioactive trapped-ion qubit,* $^{133}Ba^{+}$. PhD thesis, UCLA, 2020.

[79] Brendan M. White, Pei Jiang Low, Yvette de Sereville, Matthew L. Day, Noah Greenberg, Richard Rademacher, and Crystal Senko. Isotope-selective laser ablation ion-trap loading of $^{137}Ba^{+}$ using a $bacl_2$ target. *Phys. Rev. A*, 105:033102, Mar 2022.

[80] Nicholas C. Lewty, Boon Leng Chuah, Radu Cazan, Murray D. Barrett, and B. K. Sahoo. Experimental determination of the nuclear magnetic octupole moment of $^{137}ba^{+}$ ion. *Phys. Rev. A*, 88:012518, Jul 2013.

[81] M. Hoffman. *Observation of the Nuclear Magnetic Octupole Moment of 137Ba+*. PhD thesis, University of Washington, 2014.